UNIVERSITY OF POTSDAM

MASTER THESIS

# Magnetization precession in 3D metals: the role of heat and strain

*Supervisor:*
Maximillian MATTERN
Dr. Alexander von REPPERT

*Examiner:*
Prof. Dr. Matias BARGHEER
Dr. Daniel SCHICK

*Author:*
Fried-Conrad WEBER

Ultrafast Dynamics in Condensed Matter group
Institute of Physics and Astronomy

November 24, 2024

UNIVERSITY OF POTSDAM

# *Abstract*

Faculty of Science
Institute of Physics and Astronomy

Master Thesis

**Magnetization precession in 3D metals: the role of heat and strain**

by Fried-Conrad WEBER

This work studies the precessional magnetization response of cobalt and nickel upon laser excitation. The magnetization dynamics is measured using a time-resolved magneto-optical Kerr effect (trMOKE) at different angles of the external field and various field strengths and fluences. To systematically analyze the magnetization response, preliminary simulations of laser-induced heat and strain, using the UDKM1Dsim toolbox, are used as input to a non-norm-conserving Landau-Lifshitz-Gilbert (LLG) equation. These LLG simulations agree well with the measured magnetization response and elucidate the roles of heat and strain in driving the precession. The key findings of this research include the identification of magneto-elastic coupling as the primary driver of precession in the low fluence regime for nickel and cobalt, whereas demagnetization dominates at high fluences. Additionally, two distinct cases of magnetoelastically driven precession are found: quasi-static strain leading to a displacement of the effective field, thereby triggering precession, and the matching of the round trip time of strain pulses with the precession frequency, resulting in a resonant enhancement of the precession. The study also reveals that the substrate of the cobalt sample affects its crystallinity, which in turn influences the anisotropy and thus the precessional behavior. This comprehensive understanding of the mechanisms that trigger precession is utilized to develop a novel coherent control scheme. Instead of merely strengthening or attenuating the precession by adjusting the time delay between two pump pulses, it is demonstrated that changing the fluence, and thus transitioning from strain-driven to demagnetization-driven precession, can also be effectively employed.

# Table of contents

# List of Figures

# Chapter 1

# Introduction

The field of laser-induced magnetization dynamics has experienced a rapid advancement in recent years. Controlling magnetization dynamics is particularly interesting due to its potential for developing novel data storage media and processing devices. Beyond technological applications, however, magnetization dynamics is also fundamentally fascinating, as it encompasses a variety of phenomena, including ultrafast demagnetization [1, 2], magnetization precession in metals [3] in semiconductors [4] and insulators [5, 6], but also all-optical switching [7, 8], and magnetization nutation [9, 10].
This work focuses on studying the mechanisms that trigger magnetization precession, including the role of the effective field and how it is affected by temperature and strain. Studying the dynamics of the precessional motion as well as the driving factors is highly relevant, as precessional switching may be the fastest way to manipulate a magnetization state, as it represents the coherent motion of the magnetization vector [11, 12]. The role of strain in the observed magnetization dynamics was long neglected, but has recently been highlighted by the work of Shin et al. [13, 14] and Temnov [15, 16]. In this work it is shown that for nickel and cobalt, at small excitation fluences, where $T_\mathrm{p} \ll T_\mathrm{C}$, the strain is the primary factor driving the precession. The shape of the laser-induced strain pulses has been oversimplified in previous models. Using the well-tested UDKM1DSIM toolbox [17], magnetization precession under realistic strain pulses in laser-excited multi-interface heterostructures can be studied [18].
**Chapter 2** introduces the theoretical foundation for describing magnetization dynamics using the thermodynamic principle of the free energy, integrating contributions such as Zeeman energy, magnetocrystalline anisotropy, and magnetoelastic anisotropy. In addition to directional dynamics, also demagnetization plays an important role in the observed dynamics. To describe the occurrence of both effects simultaneously, a new model for the total magnetization dynamics is employed, which is motivated by the separation of the magnetization vector into direction $\hat{m}$ and length $|m|$ components. This approach of modifying the LLG equation to account for non-constant magnetization magnitude was independently developed by Hudl et al. [19] to model THz-induced magnetization dynamics in CoFeB thin films
**Chapter 3** provides the quasi-static magnetic and structural characterization measurements on nickel and cobalt samples. Out-of-plane hysteresis curves yield an initial estimation of the saturation field. Further ferromagnetic resonance measurements (FMR) for nickel samples allow for more precise quantification of the contributions to the free energy. X-ray diffraction reveals that nickel samples exhibit polycrystalline growth with a preferred direction $\langle 111 \rangle$, while cobalt samples show polycrystalline growth with a preferred [0001] orientation. The cobalt sample growth influences their magnetic properties, with the sample on the JGS2 substrate exhibiting better crystallinity compared to the one on the PGO substrate.
**Chapter 4** delves into precession measurements for different samples. The initial section of the chapter is devoted to the modelling of the laser-induced magentization response. FMR measurements and an accurate understanding of the effective field make nickel particularly

suitable for numerical modelling. In order to achieve accurate modelling, it is necessary to examine the thermal response and strain of the sample system, which control magnetization dynamics. The UDKM1DSIM toolbox is employed to reconstruct the samples virtually and describe heat propagation and laser-induced strain response via a one-dimensional model. As a first approximation the change in phonon temperature is employed to describe the demagnetization process through a modified Landau-Lifshitz-Gilbert (LLG) equation, motivated in Chapter 2. For nickel and cobalt, the magnetoelastic coupling constant $b_1$ is positive, ensuring that demagnetization and strain act in opposite directions after laser excitation. Modelling based on the previously introduced LLG equation captures the behavior of the observed magnetization response for various excitation conditions. By toggling mechanisms triggering precession dynamics on and off, the driving forces behind magnetization precession can be isolated. Quasi-static strain from thermal expansion drives precession dynamics in the 20 nm nickel sample and the dynamics observed in the 200 nm nickel sample in frontside excitation. For the 200 nm sample in backside excitation, strain pulses matched to the precession frequency lead to the observed precession dynamics. No FMR measurements were available for cobalt samples, so they were investigated qualitatively across different configurations. The measurements showed an increase in precession frequency and amplitude as field strength increased, reflecting changes in the initial $m_z$ component. By increasing the excitation fluence the driving mechanism for the laser-induced precession changes from pre-dominantly strain driven to predominantly demagnetization induced precession. In the final section of Chapter 4, a double-pulse coherent control scheme is presented that extends beyond conventional scenarios. Instead of triggering magnetization dynamics through a single mechanism, two mechanisms are employed, namely quasi-static strain and demagnetization.

# Chapter 2

# From static to ultrafast magentism

This work focuses the magnetization dynamics on the picosecond to nanosecond timescale after laser excitation. The primary goal is to model the precession dynamics of two different nickel films. In this chapter, only the basic magnetic mechanisms, namely the ultrafast demagnetization and precession, that are necessary to describe the dynamics will be presented. A detailed discussion of mechanisms that affect the magnetization but are not of magnetic origin, such as the generation and propagation of picosecond strain pulses, is not given here. Detailed descriptions of these processes can be found in the literature [20–22].
The magnetization $\mathbf{M}$ can be written as

$$\mathbf{M} = M_\mathrm{s}\,\boldsymbol{m} = M_\mathrm{s}\,\hat{m}\,|m| \tag{2.1}$$

The magnetization $\mathbf{M}$ is written as a term describing the orientation $\hat{m}$ and the amplitude $|m|$. Both quantities are represented by the variable $\boldsymbol{m}$. $M_\mathrm{s}$ is the saturation magnetization. This description is useful because it allows the time evolution of both variables to be treated separately. By doing this, it is possible to combine precession and demagnetization as described at the end of this chapter. To describe the magnetization dynamics, it is first necessary to determine the initial position of the magnetization. This is discussed in the first section of this chapter for both the orientation $\mathbf{m}$ and the amplitude $m$. The second section deals with the laser-induced ultrafast response of these two variables. Finally, a model is presented in which the dynamics of the direction is combined to describe the dynamics of $\boldsymbol{m}$.
In the present work, different coordinate systems are often used because, depending on the situation, a description in Cartesian coordinates is more convenient than in spherical coordinates and vice versa. To describe the orientation of the external field and the magnetization, I use the convention shown in figure 2.1.

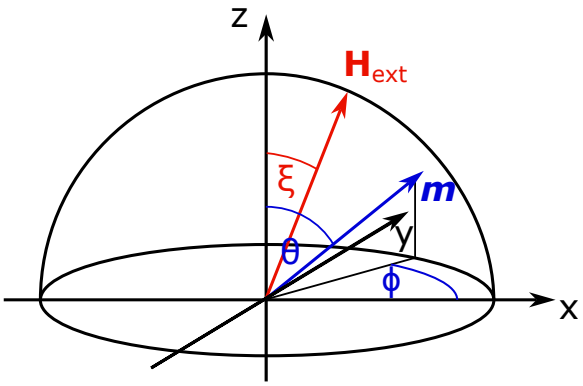


FIGURE 2.1: **Coordinate system for describing the unitless magnetization and external field:** The sample is in the x-y plane. The external field (red) is characterized by the angle $\xi$ with respect to the surface normal. The magnetization, expressed in spherical coordinates, is characterized by the angles $\theta$ and $\phi$.

## 2.1 Free energy and the direction of magnetization

In general, the magnetization of a ferromagnet does not point in the same direction as the applied external magnetic field. To describe this phenomenologically, a free energy is assigned to the magnetization [21], which depends on the external field as well as the orientation and amplitude of the magnetization itself. The equilibrium orientation of the magnetization is then determined by minimizing the free energy. The free energy consists of several different contributions describing the different types of magnetic interactions

$$F = F_{\text{Zee}} + F_{\text{eff}} + F_{\text{mc}} + F_{\text{me}}. \tag{2.2}$$

The first part $F_{\text{Zee}}$ is called the Zeeman energy, the second $F_{\text{eff}}$ is the effective anisotropy that combines shape and any possible uniaxial anisotropy, the third term $F_{\text{mc}}$ is called magneto crystalline anisotropy and the last $F_{\text{me}}$ is the magneto elastic term. The free energy reduces the complexity of the system as it captures the different interactions between the magnetic moments and the magnetic field and the interactions of the magnetic moments on a lattice. In the following the individual contributions to the free energy are motivated.

### 2.1.1 Zeeman energy

In an external magnetic field, magnetic moments tend to align parallel to the external field. The free energy that describes this behaviour is called the Zeeman free energy

$$F_{\text{Zee}} = -\mu_0 M_{\text{s}} \, \mathbf{m} \cdot \mathbf{H}_{\text{ext}}. \tag{2.3}$$

The free energy is minimized as $\boldsymbol{m}$ is parallel to the external field $\boldsymbol{H}_{\text{ext}}$.

### 2.1.2 Effective anisotropy energy

The origin of the shape anisotropy is the dipole-dipole interaction between the magnetic moments. The total energy of this interaction is obtained by summation over all the atomic

magnetic dipole moments $m_i$ and $m_j$, [23],

$$E_{\text{dip-dip}} = -\frac{1}{2\,\pi\mu_0} \sum_{i \neq j} \frac{1}{r_{ij}^3} \left[ \mathbf{m}_i \cdot \mathbf{m}_j - 3 \frac{\left(\mathbf{r}_{ij} \cdot \mathbf{m}_i\right)\left(\mathbf{r}_{ij} \cdot \mathbf{m}_j\right)}{r_{ij}^2} \right], \tag{2.4}$$

where $\mathbf{r}_{ij}$ is the vector connecting two dipoles. The contribution to the total energy is relatively small. For example, if one sets $m = \mu_B$ and chooses a typical distance between the magnetic moments of 2 Å, one finds an energy of less than 0.1 meV [24]. Nevertheless, the influence of this interaction cannot be neglected. As illustrated in figure 2.2, the free energy

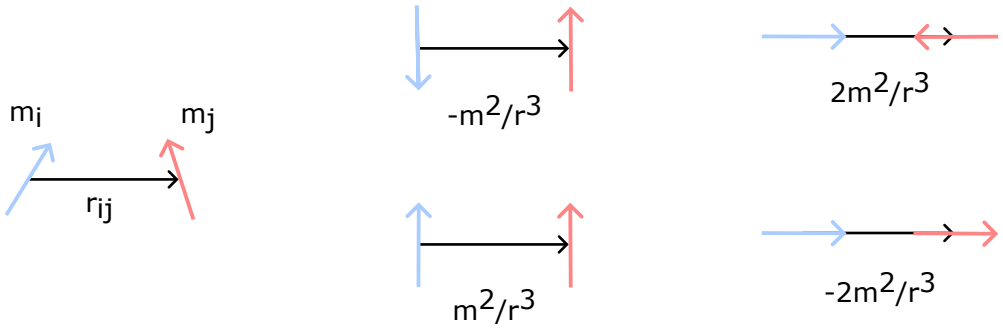


FIGURE 2.2: **Physical origin of the shape anisotropy.** The variables of equation 2.4 are represented on the left. In the center, a configuration is shown where the magnetic moments are parallel and antiparallel to each other, perpendicular to the internuclear axis. On the right, the parallel and antiparallel configuration is shown for the case where the magnetic moments are parallel to the internuclear axis. The free energy, as defined by equation 2.4, is written below each sketch. The parallel orientation of the magnetic moments along the internuclear axis is the most favorable. [23]

is minimized as the magnetic dipoles lay parallel to one another and the internuclear axis. As for a thin film, the number of internuclear axes $\mathbf{r}_{ij}$ lying in the plane is much higher, than the internuclear axis pointing out-of plane. Thus, the energy is minimized when the magnetization lies in the plane.
For a sample with an arbitrary shape the free energy is usually expressed as [25]

$$F = \frac{\mu_0}{2} M_s^2 \left( N_x m_x^2 + N_y m_y^2 + N_z m_z^2 \right), \tag{2.5}$$

here $N_x$, $N_y$ and $N_z$ are the shape factors whose sum is equal to one. In general, however, it is possible that other uniaxial anisotropies appear in addition to the shape anisotropy. These have the same proportionalities with respect to magnetization as the shape anisotropies, and can therefore be incorporated by introducing effective anisotropy factors, $N_x \rightarrow N_x^{\text{eff}}$. As shown in the following calculation this expression can be simplified even further by

rewriting it in spherical coordinates and substituting $N_y^{\text{eff}} + \Delta = N_x^{\text{eff}}$

$$\begin{aligned} F &= \frac{\mu_0}{2} M_s^2 \left( (N_y^{\text{eff}} + \Delta) \sin^2\vartheta \cos^2\varphi + N_y^{\text{eff}} \sin^2\vartheta \sin^2\varphi + N_z^{\text{eff}} \cos^2\vartheta \right) \\ &= \frac{\mu_0}{2} M_s^2 \left( N_y^{\text{eff}} \sin^2\vartheta \left(\cos^2\varphi + \sin^2\varphi\right) + \Delta \sin^2\vartheta \cos^2\varphi + N_z^{\text{eff}} \cos^2\vartheta \right) \\ &= \frac{\mu_0}{2} M_s^2 \left( N_y^{\text{eff}} \left(1 - \cos^2\vartheta\right) + \Delta \sin^2\vartheta \cos^2\varphi + N_z^{\text{eff}} \cos^2\vartheta \right) \\ &= \frac{\mu_0}{2} M_s^2 \left( N_y^{\text{eff}} + \Delta m_x^2 + \left( N_z^{\text{eff}} - N_y^{\text{eff}} \right) m_z^2 \right) \end{aligned} \tag{2.6}$$

The first term in the parentheses is a constant offset of the free energy, which is independent of the direction of magnetization. Since this offset has no influence on the direction of the minimal free energy and makes no contribution to the effective field, this term can be discarded. By substitution, the equation (2.6) can be simplified to give the following equation for the effective anisotropy energy.

$$F_{\text{eff}} = \frac{\mu_0}{2} M_s^2 \left( N_x^{\text{eff}} m_x^2 + N_z^{\text{eff}} m_z^2 \right) \tag{2.7}$$

### 2.1.3 Magnetocristalline anisotropy (MCA)

The field-dependent magnetization of crystalline samples shows a different behavior depending on along which crystalline direction the external field is applied. The origin of the magnetocrystalline anisotropy lies in the spin-orbit coupling. Since different kinds of many-body interactions play a role as well, and the complexity of the electronic band structure is quite overwhelming, there is no simple model. However, the main mechanisms responsible for the MCA are quite simple. The angular moments of the atomic orbitals are aligned in a crystal structure due to the Coulomb interactions between the orbitals. Consequently, due to the spin-orbit coupling, the spins align along a preferred direction in the crystal. [23, 24] For nickel, which has a cubic crystal structure, the magnetization is easier to align along the $\langle 111 \rangle$ [1] cube diagonals than along the $\langle 100 \rangle$ edges. For iron it is exactly the opposite. Cobalt, on the other hand, has a hexagonal crystal structure at room temperature, in this case there is a hard axis along the [001] direction [26]. Figure 2.3 illustrates the lattice structure Cobalt, Iron and Nickel and the corresponding magnetocrystalline free energy surfaces. Assuming that for the hexagonal structure the [001] direction coincides with the z-axis, the free energy for a cubic and a hexagonal system is given by [26] :

$$F_{\text{mc}}^{\text{cub}} = K_1 \left( m_x^2 m_y^2 + m_y^2 m_z^2 + m_z^2 m_x^2 \right) + K_2 \left( m_x^2 m_y^2 m_z^2 \right) \tag{2.8}$$

$$F_{\text{mc}}^{\text{hex}} = K_1 \cos^2(\vartheta) + K_2 \cos^4(\vartheta) = K_1 m_z^2 + K_2 m_z^4 \tag{2.9}$$

Here $K_1$ and $K_2$ are the magnetocrystalline anisotropy constants. The hexagonal anisotropy is often expressed in powers of $\sin(\theta)$. For this conversion, $\cos(\theta)^2 = (1 - \sin\theta)^2$ is used, which also changes the anisotropy factors. The anisotropy factors for the 3d ferromagnets Iron, Cobalt and Nickel are given in table 2.1. For nickel, the MCA is so small that it can be neglected. For cobalt, however, it is much stronger. If the higher order contributions ($K_2$) to the hexagonal MCA of cobalt are neglected, then the MCA can be considered as a contribution to the effective anisotropy.

[1] The indices of particular directions are written in square brackets, such as the six cube-edge directions: [100], [010], [001], [-100], [0-10], and [00-1]. These are directions of a form, the whole set of these directions are written in angular brackets $\langle 100 \rangle$.

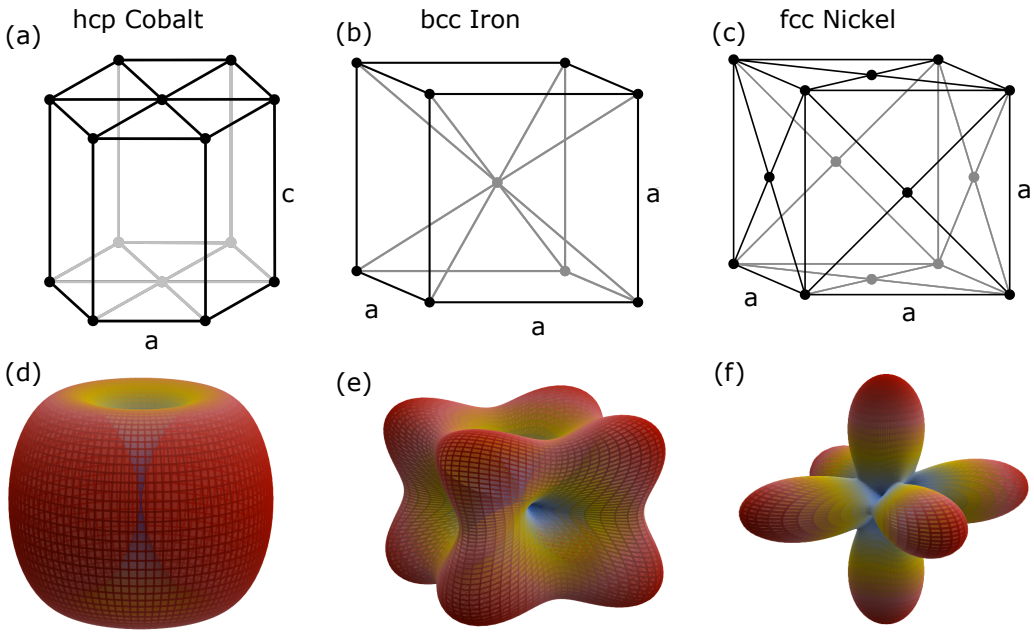


FIGURE 2.3: **Crystalline structures and magnetocrystalline free energy surfaces for the 3d metals Co, Fe, Ni:** (a-c) depicts the unit cells of Cobalt, Iron and Nickel. In (d-f) the magnetocrystalline free energy surfaces are shown. The minima of the free energy defines the easy easy-axis.

| element | $K_1$ ($10^4$ J/m$^3$) | $K_2$ ($10^4$ J/m$^3$) |
|---|---|---|
| Fe | 4.8 | $\pm$ 0.5 |
| Co | -75 | 15 |
| Ni | -0.5 | -0.2 |

TABLE 2.1: Crystal anisotropy constants for 3d ferromagnets [26].

### 2.1.4 Magneto-elastic anisotropy

Magnetoelastic anisotropy is responsible for the coupling of strain with magnetization. The origin of this interaction is complex and cannot be attributed to a uniform mechanism, since it is material dependent. One plausible mechanism is spin-orbit coupling. Due to a distortion of the lattice, other orientations of the atomic orbitals are energetically more favorable, which eventually affects the orientation of the magnetic moments [27]. Another plausible mechanism is the dipole-dipole interaction between the magnetic moments, which changes when the lattice is distorted. However, calculations show that the magnetoelastic coupling factors obtained are too small by a factor of 5 for iron and even have the wrong sign for nickel [28]. A recent paper identified the main mechanism for iron as a Dzyaloshinskii-Moriya-like interaction based on a symmetry-breaking distortion of the lattice [29].
Empirically, the total free energy for the magnetoelastic coupling is given by [21]

$$F_{me} = -b_1(\eta_{xx}m_x^2 + \eta_{yy}m_y^2 + \eta_{zz}m_z^2) - b_2(\eta_{xy}m_x m_y + \eta_{yz}m_y m_z + \eta_{zx}m_z m_x) \tag{2.10}$$

Here $b_1$ and $b_2$ are the magneto-elastic coupling parameters and $\eta_{ij}$ is the strain in a certain direction. In this work it is assumed that there is only one contribution to $\eta_{zz}$. This is a good approximation for a continuous thin film where the probed region is homogeneously pumped. In addition, the out-of-plane expansion of the continuous film is is enhanced as the in-plane expansion is compensated. [20]

### 2.1.5 Temperature dependence and effective field

The anisotropy constants show a strong dependence on temperature [30, 31]. The anisotropy almost always decreases with increasing temperature and disappears before the Curie temperature is reached. A typical model to describe the temperature dependence is based on the assumption that the deviation of the individual magnetic moments from the mean orientation increases with increasing temperature. In this model the temperature dependent anistropy is given by the following proportionality [26]

$$\frac{K^n}{K_0^n} \propto m^{\frac{n(n+1)}{2}} \tag{2.11}$$

Where $n$ is the power of the anisotropy function. For the uniaxial anisotropy $K_u$ ($n = 2$) and the cubic anisotropy $K_1$ (n=4) then the following relationship exists

$$\frac{K_u}{K_{u,0}} \propto m^3, \tag{2.12}$$

$$\frac{K_1}{K_{1,0}} \propto m^{10}. \tag{2.13}$$

In contrast to the method described above, this work employs an alternative approach to incorporate temperature-dependent anisotropy. Instead of neglecting temperature dependence or using the model that fails for materials other than iron, we replace the magnetization in the free energy formulas with a temperature-dependent reduced magnetization, denoted as $\mathbf{m} \rightarrow \boldsymbol{m}$.
To model the magnetization, not the external field, but the effective field, which is derived from the total free energy of the macroscopic magnetization $\mu_0 \mathbf{H}_{eff} = -\nabla_{\boldsymbol{M}} F$ is important. For nickel the MCA is small and can be neglected so the effective field is written as:

$$\mathbf{H}_{\text{eff}} = \mathbf{H}_{\text{ext}} - N_{\text{z}}^{\text{eff}} M_{sat} m_{\text{z}} \mathbf{e}_{\text{z}} + N_{\text{x}}^{\text{eff}} M_{\text{sat}} m_{\text{x}} \mathbf{e}_{\text{x}} + \frac{b_1 \eta}{\mu_0 M_{\text{sat}}} m_{\text{z}} \mathbf{e}_{\text{z}} \tag{2.14}$$

Neglecting higher order contributions to the MCA of cobalt, the effective field in this case can be expressed by

$$\mathbf{H}_{\text{eff}} = \mathbf{H}_{\text{ext}} - N_{\text{z}}^{\text{eff}} M_{\text{sat}} m_{\text{z}} \mathbf{e}_{\text{z}} + \frac{2\, K_{\text{u}}}{\mu_0 M_{\text{s}}} m_{\text{z}} \mathbf{e}_{\text{z}} + N_{\text{x}}^{\text{eff}} M_{\text{sat}} m_{\text{x}} \mathbf{e}_{\text{x}} + \frac{2\, b_1 \eta}{\mu_0 M_{\text{sat}}} m_{\text{z}} \mathbf{e}_{\text{z}} \tag{2.15}$$

For both cases the effective field can be written as:

$$\mathbf{H}_{\text{eff}} = \mathbf{H}_{\text{ext}} - H_{\text{sat}} m_{\text{z}} \mathbf{e}_z + H_{\text{uni}} m_{\text{x}} \mathbf{e}_x + H_{\text{me}} m_{\text{z}} \mathbf{e}_z \tag{2.16}$$

Here $H_{\text{sat}}$ is the saturation field , $H_{\text{uni}}$ is the uniaxial field and $H_{\text{me}}$ is the magnetoelastic field.

## 2.2 Mean-field model and the length of the magnetization

The magnetization of a sample depends strongly non-linearly on the temperature. While for small temperatures the magnetization is due to the excitation of spinwaves [24] proportional to $\left(1 - (T/T_{\text{C}})^{3/2}\right)$ at high temperatures the magnetization decreases drastically

until it vanishes at the Curie Temperature $T_C$. This section aims to describe this temperature dependence in the context of the mean-field model. The basic idea is that a spontaneous magnetization exists, i.e. ordered magnetization in specific regions or domains that an external field can macroscopically align. To explain the spontaneous magnetization, the magnetic moments of the atoms must be aligned and prevail the thermal motion. A simple explanation for this alignment would be the magnetic dipole interaction between the magnetic moments, but a closer look reveals that this interaction is too small and only allows for magnetic ordering at temperatures below 1 K. In order to understand the magnetic order at higher temperatures, a much stronger interaction must therefore be important. In the early days of this theory, Pierre Weiss postulated an enormously strong molecular field with a field strength of about 1000 T. Nowadays we understand this enormous field in the context of quantum mechanics as an exchange interaction between magnetic moments [23].

### 2.2.1 Exchange energy and mean field model

The exchange energy between magnetic moments is a consequence of the Coulomb interaction, in conjunction with quantum mechanical effects such as the Heisenberg uncertainty principle and the Pauli exclusion principle. In the Heisenberg model of magnetism, the exchange interaction between the localized electrons in the crystal lattice is expressed by the following Hamiltonian: [24]

$$H = -\frac{J}{\hbar^2} \sum_{j=1}^{z} \mathbf{S}_\mathrm{i} \cdot \mathbf{S}_\mathrm{j} \,. \tag{2.17}$$

The interaction energy depends on the exchange constant $J$ and the scalar product of the angular momentum vectors of neighbouring magnetic moments $\mathbf{S}_\mathrm{j}$. The average exchange energy is given by replacing the magnetic moment $\mathbf{S}_\mathrm{j}$ with the mean value over time $\langle \mathbf{S}_\mathrm{j} \rangle$.

$$E = -z \frac{J}{\hbar^2} \langle \mathbf{S}_\mathrm{i} \rangle \cdot \mathbf{S}_j \,. \tag{2.18}$$

The effect of this approximation is depicted in Figure 2.4; instead of looking at the interaction of all spins with each other, a single spin interacts with the mean value of the other spins. The magnetization can be expressed in terms of the mean value of the spins,

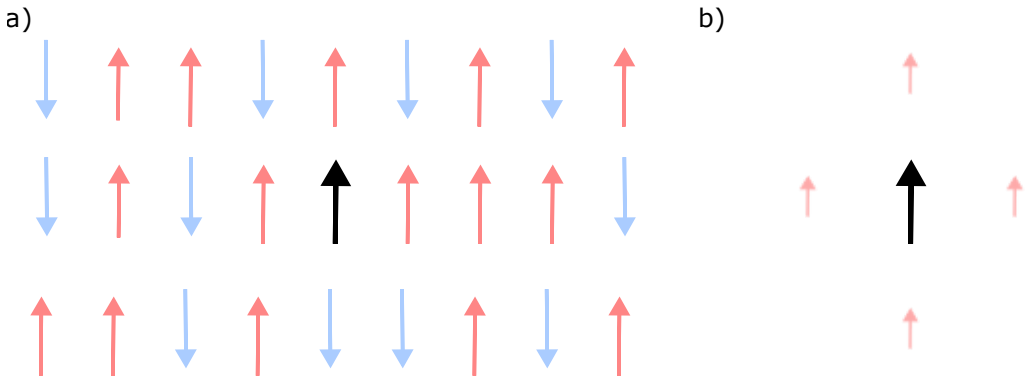


FIGURE 2.4: **Approximating the exchange interaction** a) Spins on a lattice that interact via exchange coupling b) The interaction of the spins can be approximated by only looking at one spin and describe all other spins by their mean value.

$$\mathbf{M} = -ng\mu_{\mathrm{B}}\frac{\langle S_j \rangle}{\hbar}\,, \tag{2.19}$$

where $n$ is the density of atoms, $g$ is the Landé-factor and $\mu_{\mathrm{B}}$ is the Bohr magneton. If we now substitute the magnetization into the upper equation and compare this with the energy of a magnetic moment $\mu$ in a magnetic field

$$\mathbf{E} = -\left(-g\mu_{\mathrm{B}}\mathbf{S}_{\mathrm{i}}\right)\cdot\frac{zJ\hbar}{ng^2\mu_{\mathrm{B}}^2}\mathbf{M} = -\mu\cdot\mathbf{B}_A\,, \tag{2.20}$$

one finds the exchange field or molecular field $\mathbf{B}_A$,

$$\mathbf{B}_A = \frac{z\,J}{ng^2\mu_{\mathrm{B}}^2}\mathbf{M} = \mu_0\gamma_{\mathrm{mf}}\,\mathbf{M}. \tag{2.21}$$

Here $\gamma_{\mathrm{mf}}$ is the so-called molecular field or mean field constant [23, 24] .

### 2.2.2 Temperature dependence

In summary, the approximation is thus to describe the magnetization with the help of a single magnetic moment that experiences the external field and a molecular field produced by the other magnetic moments.

$$\mathbf{B} = \mathbf{B}_{ext} + \mathbf{B}_A = \mathbf{B}_{ext} + \mu_0\gamma_{\mathrm{mf}}\,\mathbf{M} \tag{2.22}$$

As depicted in Figure 2.5, this system can be described as a two level system where the

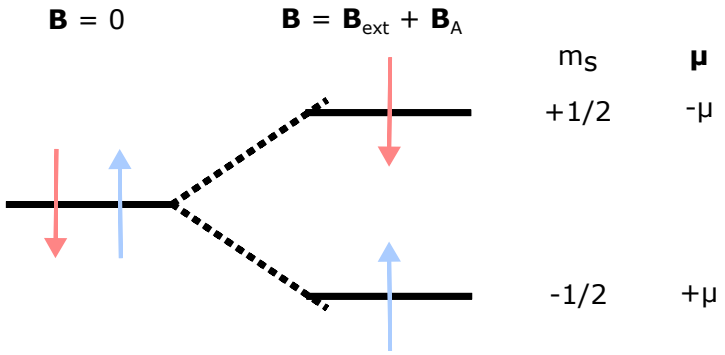


FIGURE 2.5: **Splitting of energy levels in magnetic field** The energy levels split due to the magnetic field that is mostly generated by the exchange interaction (mean-field). The lower energy level is preferred for temperature where $k_{\mathrm{B}}T \ll \mu B$, which leads to a total magnetization parallel to the field.

magnetic moment can occupy two different states [2]. Either it is parallel $M_{\mathrm{s}} = -1/2$, $\mu = \frac{1}{2}g\mu_{\mathrm{B}} \approx \mu_{\mathrm{B}}$ or antiparallel $M_{\mathrm{s}} = 1/2$, $\mu = -\frac{1}{2}g\mu_{\mathrm{B}} \approx -\mu_{\mathrm{B}}$ to the effective field. As mentioned earlier, the postulated molecular/mean field has an enormous field strength $B_{\mathrm{A}} \gg B_{\mathrm{ext}}$. Then the occupation numbers of the parallel $N_{\mathrm{p}}$ and the antiparallel state $N_{\mathrm{a}}$ are given by

[2] For materials such as Fe, Co and Ni, this description is sufficient. One must introduce further levels for materials with a large magnetic moment, such as gadolinium ($m_J = -7/2 \ldots 7/2$). If one generalizes the derivation for arbitrary values of $J$, one obtains the Brillouin function.

[32]

$$\frac{N_{\mathrm{p}}}{N} = \frac{\exp\left(\mu_{\mathrm{B}} B_{\mathrm{A}}/k_{\mathrm{B}}T\right)}{\exp\left(\mu_{\mathrm{B}} B_{\mathrm{A}}/k_{\mathrm{B}}T\right) + \exp\left(-\mu_{\mathrm{B}} B_{\mathrm{A}}/k_{\mathrm{B}}T\right)} \tag{2.23}$$

$$\frac{N_{\mathrm{a}}}{N} = \frac{\exp\left(-\mu_{\mathrm{B}} B_{\mathrm{A}}/k_{\mathrm{B}}T\right)}{\exp\left(\mu_{\mathrm{B}} B_{\mathrm{A}}/k_{\mathrm{B}}T\right) + \exp\left(-\mu_{\mathrm{B}} B_{\mathrm{A}}/k_{\mathrm{B}}T\right)} \tag{2.24}$$

Expressing the magnetization as the balance of parallel and antiparallel states, and by writing $x = \mu_{\mathrm{B}} B_{\mathrm{A}}/k_{\mathrm{B}}T$, one finds the following relation for the magnetization:

$$M(T) = N\,\mu_{\mathrm{B}}\left(\frac{N_p}{N} - \frac{N_a}{N}\right) = N\,\mu_{\mathrm{B}}\left(\frac{e^x - e^{-x}}{e^x + e^{-x}}\right) = M_{sat}\ \tanh(x) \tag{2.25}$$

writing out this expression, one finds,

$$M(T) = M_{sat}\tanh\left(\frac{\mu_{\mathrm{B}} B_{\mathrm{A}}}{k_{\mathrm{B}}\,T}\right), \tag{2.26}$$

in terms of normalized magnetization $m = \frac{M}{M_{\mathrm{S}}}$, one can rewrite this as

$$m(T) = \tanh\left(\frac{\mu_{\mathrm{B}} B_{\mathrm{A}}}{k_{\mathrm{B}}\,T}\right) = \tanh\left(\frac{\mu_{\mathrm{B}}\mu_0\gamma_{\mathrm{mf}} M_{sat}(0)m(T)}{k_{\mathrm{B}}\,T}\right) = \tanh\left(\frac{T_{\mathrm{C}}\,m(T)}{T}\right), \tag{2.27}$$

here $T_{\mathrm{C}}$ is the Curie temperature $T_{\mathrm{C}} = \mu_{\mathrm{B}}\,B_{\mathrm{A}}/k_{\mathrm{B}} = \mu_{\mathrm{B}}\mu_0\gamma_{\mathrm{mf}} M_{sat}(0)/k_{\mathrm{B}}$ and $M_{sat}(0)$ is the saturation magnetization at absolute zero temperature. The relations in 2.27 cannot be

| element | $B_{\mathrm{A}}$ (T) | $T_{\mathrm{C}}$ (K) |
|---|---|---|
| Fe | 1553 | 1043 |
| Co | 2067 | 1388 |
| Ni | 949 | 637 |

TABLE 2.2: Curie temperatures and calculated molecular fields for 3d transition metals. [23]

.

solved analytically for $m$(T) as it is a transcendental equation. However, one can solve this numerically by re-expressing this as

$$m(T) - \tanh\left(\frac{T_{\mathrm{C}}\,m}{T}\right) = 0, \tag{2.28}$$

since there are many very efficient algorithms for finding zeros.

### 2.2.3 Free energy formulation

Section 2.1 describes how the orientation of the magnetization can be determined by minimizing the free energy. This section aims to briefly describe how the amplitude of the magnetization can be calculated in the free energy framework. For the Ising model the free energy is given by [33]

$$F_L^{\mathrm{Is}}(m) = -\frac{k_{\mathrm{B}}\,T_{\mathrm{C}}}{2}\,m^2 - \mu_{\mathrm{B}}\,B\,m + \frac{k_{\mathrm{B}}\,T}{2}\log\left[\frac{1-m^2}{4}\right] + m\,k_{\mathrm{B}}\,T\,\mathrm{arctanh}(m), \tag{2.29}$$

and for the mean-field model it is [34]

$$F_L^{\mathrm{mf}}(m,B) = -\frac{k_\mathrm{B}\,T_\mathrm{C}}{2}\,m^2 - \mu_\mathrm{B}\,B\,m + \frac{k_\mathrm{B}\,T}{2}\left[(1+m)\ln(1+m) + (1-m)\ln(1-m)\right] - k_\mathrm{B}\,T\ln(2) \tag{2.30}$$

For both models one can find the temperature dependent magnetization by minimizing the free energy. For the Ising model the equlibrium condition becomes

$$\begin{aligned}\frac{F_L^{\mathrm{Is}}(m)}{dm} &= -\mu_\mathrm{B}\,B - k_\mathrm{B}\,T_\mathrm{C}\,m + k_\mathrm{B}\,T\,\mathrm{arctanh}(m) = 0 \\ \leftrightarrow\; m &= \tanh\left(\frac{T_\mathrm{C}\,m}{T} + \frac{\mu_\mathrm{B}\,B}{k_\mathrm{B}\,T}\right)\end{aligned} \tag{2.31}$$

The same result is obtained by minimizing the free energy of the mean field model

$$\frac{F_L^{\mathrm{mf}}(m)}{dm} = -\mu_\mathrm{B}\,B - k_\mathrm{B}\,T_\mathrm{C}\,m + \frac{k_\mathrm{B}\,T}{2}\ln\left(\frac{1+m}{1-m}\right) = -\mu_\mathrm{B}\,B - k_\mathrm{B}\,T_\mathrm{C}\,m + k_\mathrm{B}\,T\,\mathrm{arctanh}(m) = 0 \tag{2.32}$$

For $B = 0$ this yields the same temperature dependence as for the mean field model (equation 2.27). In figure 2.6 this temperature-dependent magnetization for various external magnetic fields is compared with data from nickel, cobalt and iron [35]. It can be seen that this model describes the temperature dependence for these materials in good approximation. External fields lead to deviations near the Curie temperature as $B_\mathrm{A} \approx B_\mathrm{ext}$.

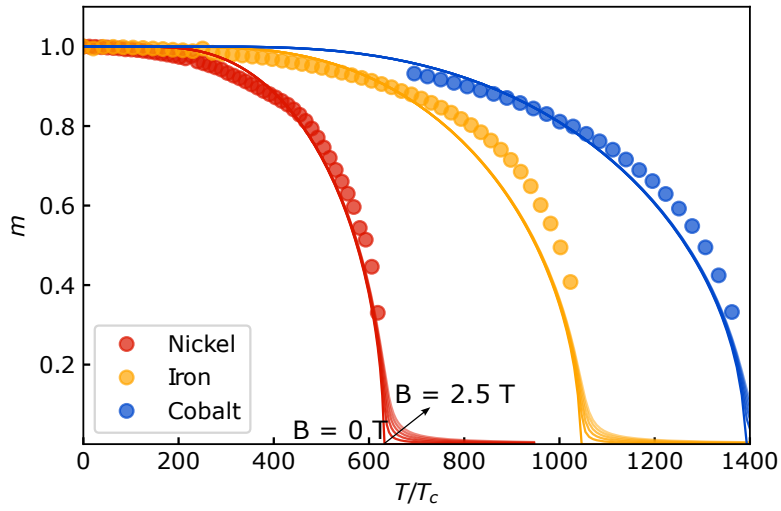


FIGURE 2.6: **Temperature dependence of the magnetization** for the 3d transition metals nickel (red), iron (orange) and cobalt (blue). The solid lines represents the solution of equation 2.31 for different external fields from 0 up to 2.5 T. The data (dots) are taken from [35]

## 2.3 Magnetization dynamics

To describe the magnetization dynamics after laser excitation, two different quantities are of interest. First, how the orientation of the magnetization $\boldsymbol{m}$ changes and second, how the

amplitude of the magnetization $m$ changes. The following section deals with the description of the magnetization precession in the context of the Landau-Lifshitz-Gilbert (LLG) equation and the description of the laser-induced ultrafast demagnetization dynamics. At the end of this chapter, a simple model is presented that combines these two types of dynamics by using non-norm conserving LLG equation.

### 2.3.1 Directional dynamic

The precession dynamics of the magnetization is described with the help of the LLG. This is given as [36]

$$\frac{\partial \mathbf{m}}{\partial t} = -\gamma\mu_0 \mathbf{m} \times \mathbf{H}_{\text{eff}} + \alpha \mathbf{m} \times \frac{\partial \mathbf{m}}{\partial t}. \tag{2.33}$$

In this equation, $H_{\text{eff}}$ is the effective field, which is composed of the external field, plus material-specific other fields (equation 2.16), $\gamma$ is the gyromagnetic ratio, and $\alpha$ is a damping constant. This equation can be rewritten in the same form as the Landau-Lifshitz equation. For small damping they are even identical. For large damping, however, the precession frequency is reduced, similar to a damped harmonic oscillator. The rewritten equation is

$$\frac{\partial \mathbf{m}}{\partial t} = -\frac{\gamma\mu_0}{1+\alpha^2} \mathbf{m} \times \mathbf{H}_{\text{eff}} - \frac{\gamma\alpha\mu_0}{1+\alpha^2} \mathbf{m} \times (\mathbf{m} \times \mathbf{H}_{\text{eff}}) \tag{2.34}$$

The first term of this equation is responsible for the precession of the magnetization, the second term is responsible for the damping of the dynamics until the magnetization has reached the new equilibrium. The equilibrium position of the magnetization can be determined by setting this equation to zero. Two conditions characterize the equilibrium position: either the magnetization is parallel to the effective field or the effective field has to vanish For an effective field as given in the equation 2.16, the magnetization in the initial position generally points in the same direction as the effective field. The special case where the effective field vanishes applies when uniaxial contributions $H_{\text{uni}}$ are neglected and the external field is perpendicular to the sample plane and smaller than the saturation field $H_{\text{sat}}$. Displacing the effective field from equilibrium initiates magnetization dynamics. This displacement can happen for several reasons: If the sample is heated by laser excitation, it generally expands, leading to local strain that alters the effective field via the magneto-elastic coupling. The strain consists of the quasi-static thermal expansion and propagating picosecond strain pulses. Demagnetization can also lead to precession. In this case, the demagnetization reduces the contribution of the saturation field and the effective field is displaced. A detailed discussion of these phenomena is given in section 4.1.

### 2.3.2 Demagnetization

As described in section 2.2, the magnetization depends sensitively on the temperature. Therefore, it is necessary to model the laser-induced temperature change before modeling the demagnetization. The response of the magnetization can be described in the framework of a microscopic two-temperature model introduced by Koopmans et al. [37]. Three different subsystems constitute the material. These are the electron system with temperature $T_{\text{e}}$, which is heated by the laser excitation, the phonon system with temperature $T_p$, to which the electron system transfers heat until they have the same temperature, and the magnetization, which depends on $T_{\text{e}}$ and $T_p$. This model is characterized by the following 3 equations

[37]:

$$\frac{dT_\mathrm{e}}{dt} = -\frac{G_\mathrm{ep}}{C_\mathrm{e}}(T_\mathrm{e} - T_p) + \frac{P(t)}{C_\mathrm{e}}, \tag{2.35}$$

$$\frac{dT_\mathrm{p}}{dt} = -\frac{G_\mathrm{ep}}{C_\mathrm{p}}(T_p - T_\mathrm{e}), \tag{2.36}$$

$$\frac{dm}{dt} = Rm\frac{T_\mathrm{p}}{T_\mathrm{C}}\left(1 - m\coth\frac{mT_\mathrm{C}}{T_\mathrm{e}}\right). \tag{2.37}$$

Here, $R$ is a coupling constant, for Nickel, R is 17.2 $\frac{1}{\mathrm{ps}}$ and for Cobalt 25.3 $\frac{1}{\mathrm{ps}}$ [37]. $G_\mathrm{ep}$ is the electron phonon coupling, which determines the rate at which energy is transferred between the electronic and phononic systems. $C_\mathrm{e}$ and $C_\mathrm{p}$ are the heat capacities of these systems. The equilibrium position in this model can be found by setting equation 2.37 to zero. This condition can be rewritten as follows

$$0 = \left(1 - m\coth\frac{mT_\mathrm{C}}{T_\mathrm{e}}\right) \quad \leftrightarrow \quad 1 = m\ \coth\left(\frac{T_\mathrm{C}\,m}{T}\right) \quad \leftrightarrow \quad m = \tanh\left(\frac{T_\mathrm{C}\,m}{T}\right), \tag{2.38}$$

surprisingly it becomes identical with the temperature dependent magnetization in the mean-field model (equation 2.27).
In the vicinity of the ferromagnetic phase transition, the heat capacity of the material increases dramatically. This increase must be taken into account when describing the temperature dynamics near the ferromagnetic phase transition. This is done, for example, within the scope of the strong electron-spin coupling two temperature model (s-TTM) [38]. Here, the heat capacity of the electrons is extended by a contribution that takes into account the degree of freedom of the spins and thus their contribution to the total heat capacity. It was shown that this extension also corrects the temporal evolution of the phonon temperature, as the electron system now can store more energy, which in turn lowers the temperature of the phonon system [39].

### 2.3.3 Combining precession and demagnetization

The main focus of this work is to describe the precession dynamics in nickel and cobalt. As mentioned above, this is done using the LLG equation. Demagnetization effects are often inevitable in real experiments, especially for nickel which has a comparatively low Curie temperature both phenomena have to be combined for a complete description of the magnetization dynamics. In the literature this is achieved within the framework of the Landau-Lifshitz-Bloch equation [40, 41]. In this work, however, a different, and potentially less complex approach is taken, based on the assumption that the longitudinal and transverse dynamics occur on separate timescales. Rewriting the derivative of the magnetization to separate the longitudinal and transverse dynamics yields:

$$\frac{\partial \boldsymbol{m}}{\partial t} = \frac{\partial(|m|\,\hat{m})}{\partial t} = |m|\frac{\partial \hat{m}}{\partial t} + \hat{m}\frac{\partial |m|}{\partial t}. \tag{2.39}$$

This modified LLG equation was used by Hudl et al. [19] to model THz-induced magnetization dynamics in CoFeB thin films. The first term describes the precession of the magnetization, i.e. how the orientation of the magnetization changes with time. Here $\frac{\partial \mathbf{m}}{\partial t}$ is assumed to be given by given by the LLG equation. Since this term is multiplied by the amplitude of the magnetization, the precession frequency decreases for smaller amplitudes. The second term describes how the amplitude of the magnetization changes with time. The product with the orientation of the magnetization ensures that this only changes the length of the

magnetization vector. This is based on the assumption that the demagnetization dynamics are independent of the orientation of the magnetization. Since the main focus of this work is on the precession dynamics, which takes place on a time scale of about 100 ps, the ultrafast demagnetization dynamics, which takes place on time scales shorter than 100 fs [37], is modelled by solving equation 2.27 for each time step, where $T = T_\mathrm{p}$. Section 4.1 shows that this provides an excellent description of the demagnetization dynamics in the nickel samples. This simplification is possible because the excitation fluence is relatively small so that the phonon temperature in the probed region is far from the Curie temperature. In addition, the thermal coupling constant $G_\mathrm{ep}$ of electrons and phonons is relatively large for nickel, which leads to a fast equilibration ($\approx 5\,\mathrm{ps}$) of the two baths [37]. On the timescales of interest it can then be assumed that the magnetization is in thermal equilibrium. However, deviations are expected for short time scales where $T_\mathrm{e} \neq T_\mathrm{p}$.

# Chapter 3

# Sample structure and experimental setup

The magnetization dynamics are determined by the effective field. Since this is derived from the free energy, an understanding of the precession dynamics requires an understanding of the free energy associated with the magnetization. In particular, the free energy is affected by the magnetocrystalline anisotropy due to the crystal structure of the sample. The samples used in the experiments are polycrystalline. In the case of completely random polycrystalline growth, no magnetocrystalline anisotropy would occur. More often, a preferred direction, also known as a crystallographic texture, is observed. This creates anisotropy along an average preferred direction. In this chapter, the four different samples, two nickel and two cobalt samples, used in this thesis will be introduced. To study the free energy, the samples are characterized using out-of-plane magnetic hysteresis measurements and ferromagnetic resonance (FMR) measurements for the two nickel samples. The crystalline structure of all samples is studied using X-ray diffraction measurements.

## 3.1 Characterization of samples

A schematic representation of the samples used in the experiments is shown in figure 3.1. A total of four different samples were used in the experiment. These were prepared by magnetron sputtering by Dieter Engel at the MBI Berlin. PGO is a glass substrate (400 µm thick)

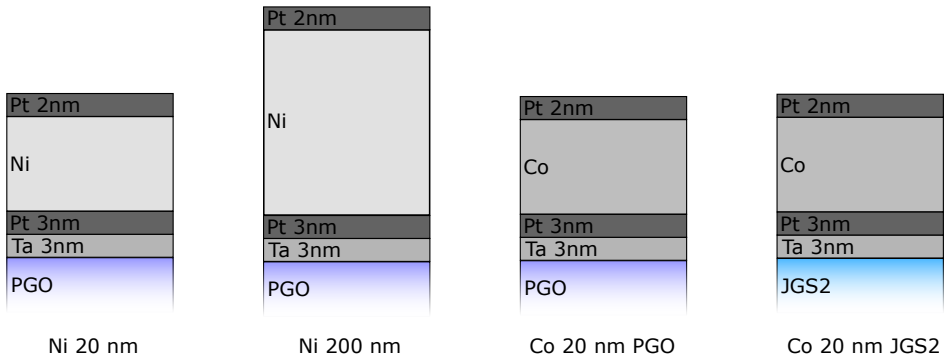


FIGURE 3.1: **Schematic representation of the samples utilized in the experiment**. The two nickel samples have different widths, while the two cobalt samples are grown on a different substrate.

from the company PGO. The material is a selected float glass (mainly soda-lime) with reduced iron content. JGS2 is a pure fused silica substrate with a thickness of 170 µm, suitable for use in the UV-optical range. The general structure of the samples is the same. To achieve polycrystalline growth, the samples are grown on a tantalum layer followed by a platinum seed layer (3 nm each). This is followed by the magnetic layer and a 2 nm thin platinum

layer to protect the ferromagnet against oxidation. The high atomic number of platinum (Pt) increases the magnetic optical Kerr effect (MOKE) contrast at the cobalt-platinum (Co-Pt) interface due to the enhanced spin-orbit coupling.

### 3.1.1 Magnetic properties

To characterize the magnetic properties, the out-of-plane hysteresis loop of the samples was measured using polar MOKE at a wavelength of 400 nm. The results for the different samples are shown in figure 3.2. As mentioned earlier, the equilibrium position of the magnetization can be calculated by minimizing the free energy. This approach is used to simulate the measured hysteresis loop for each sample. The simulated hysteresis loops reproduce the

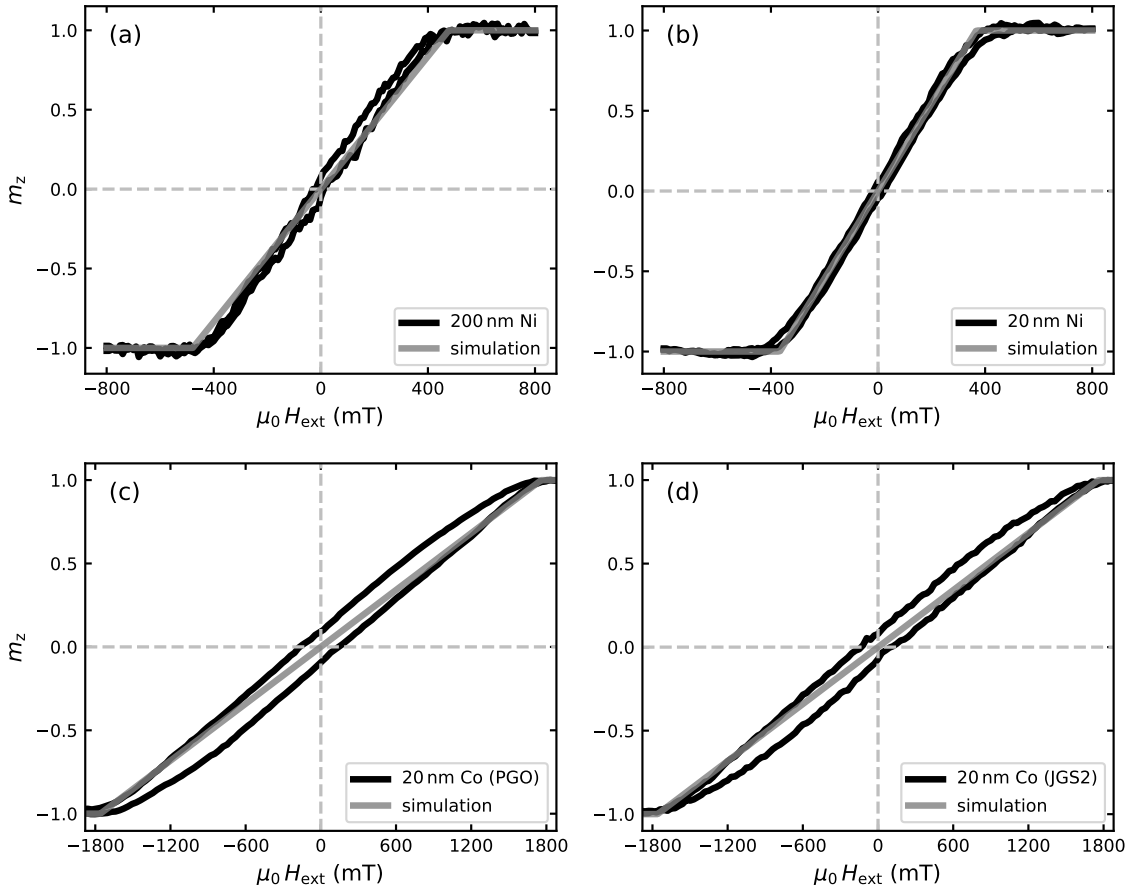


FIGURE 3.2: **Static hysteresis:** (a) for the 200nm Ni sample; (b) for the 20nm Ni sample c) for Cobalt grown on PGO and (d) for Cobalt grown on JGS2; saturation for the nickel samples is reached at B $\geq$ 0.45 T, for the cobalt sample saturation is reached at B $\geq$ 1.8 T. The grey line indicates the fitted hysteresis derived from minimizing the free energy.

overall shape of the measured curves remarkably well. However, the splitting of the measured field up and field down curves cannot be reproduced. The reason for this splitting is the existence of magnetic domains [23], which are not considered in this simple description. FMR measurements of the two nickel samples were performed by J. Carlos Rojas-Sánchez in Nancy. For the cobalt samples we can only estimate the saturation field. For the nickel samples this allows us a cross-check between the out-of-plane hysteresis loop and the FMR

| | Ni 200 | Ni 20 | Co PGO | Co JSG2 |
|---|---|---|---|---|
| $M_s$ (A/m) | $4.2 \cdot 10^5$ | $4 \cdot 10^5$ | $1.44 \cdot 10^6$ | $1.44 \cdot 10^6$ |
| $N_z^{eff}$ | 0.75 | 0.72 | 1 | 1 |
| $H_{\text{sat}}$ (mT) | 396 | 362 | 1810 | 1810 |
| $K_u$ (J/m³) | $-2.64 \cdot 10^3$ | $2.51 \cdot 10^3$ | | |
| $H_{\text{uni}}$ (mT) | -12.6 | 12.5 | | |
| $b_1$ (J/m³) | $8.1 \cdot 10^6$ | $8.1 \cdot 10^6$ | | |
| $H_{\text{me}}$ (mT/‰) | 38.6 | 40.5 | | |

TABLE 3.1: **Magnetic properties of the samples**. The saturation magnetization $M_s$, the effective saturation magnetization $M_s^{eff}$, giving rise to an effective shape anisotropy and the uniaxial in-plane anisotropy $K_u$ are tabulated.

measurements to not only estimate the saturation field, but also possible uniaxial fields. Figure 3.3 shows the in-plane FMR measurements as well as a fitting function for the two nickel samples. By fitting the hysteresis curve and the FMR measurement, the parameters listed in

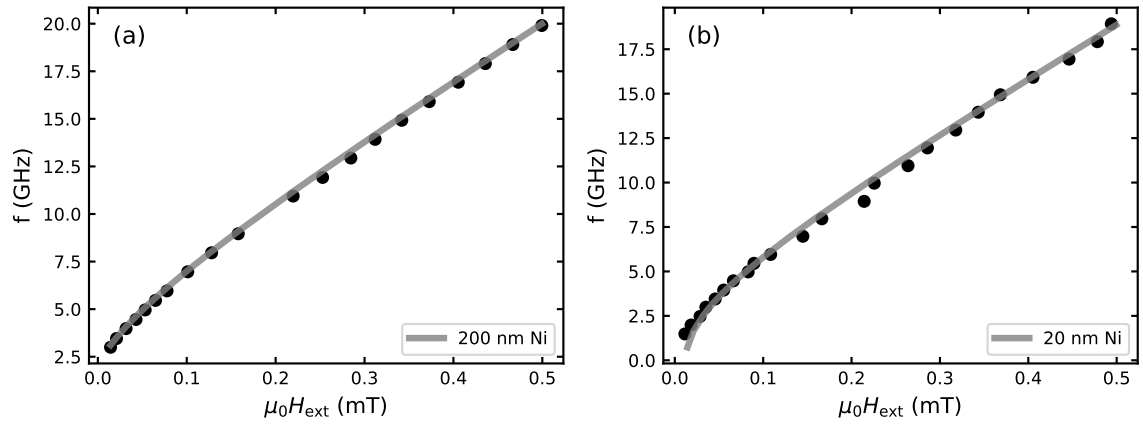


FIGURE 3.3: **FMR measurement:** (a) for the 200nm Ni sample; (b) for the 20nm Ni sample. The data is fitted using the Smit-Beljers formalism [25, 42], which is further discussed in section 4.1.2.

table 3.1 were determined for the samples. Since the hysteresis curve can be described by a wide range of parameters for $N_z^{eff}$ and $K_u$, the FMR measurement is necessary to obtain an accurate picture of the anisotropies. For the sake of completeness, the magneto-elastic coupling constant is also included in this table, although this is only determined by adjusting the simulations in section 4.1.

### 3.1.2 Structural properties

In order to investigate the crystalline structure of the samples, they were analyzed using X-ray diffraction. The measurements of the samples were carried out at a commercial laboratory-based X-ray diffraction setup (NAME) in collaboration with Sema Sarisözen. The sample was placed on a fixed sample table and the X-ray source and detector were moved at a certain angle of incidence/deflection to the sample. The measurement method itself is based on the Bragg condition. If the angle of incidence is chosen such that the Bragg

condition is satisfied, the maximum intensity measured on the X-ray detector is obtained.

$$2d\sin(\theta) = n\lambda \tag{3.1}$$

Figure 3.4 depicts the measured X-ray intensity as a function of the incident angle. Copper was used as the cathode material, so the wavelength of the X-rays corresponds to the copper K-alpha line, i.e. 1.54 Å. All samples show a strong maximum at an angle of approx-

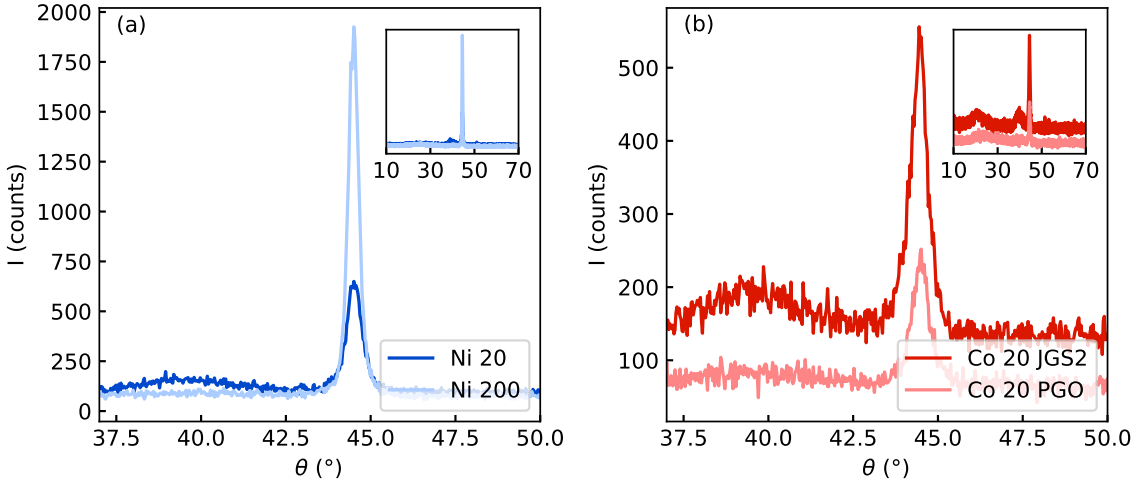


FIGURE 3.4: **X-ray diffraction measurement ($\vartheta$-2$\vartheta$):** (a) for the nickel samples (b) for the cobalt samples. The inset in the upper right-hand corner shows the diffraction signal for a wide range of angles, the main figure shows the signal in the vicinity of the strongest peak. The wavelength of the X-Ray source is 1.54 Å.

imately 45°. This maximum corresponds to the [0002] direction for the cobalt samples and ⟨111⟩ directions for the nickel samples. The different amplitude of the two nickel samples is due to the different thickness of the two samples. The difference for the two cobalt samples indicates a different crystallographic texture. From the higher peak intensity for the same film thickness, it can be concluded that the sample grown on JGS2 shows a higher degree of crystallinity than the sample grown on PGO. Different magnetic anisotropies are therefore conceivable for the two samples. Characterization using FMR would provide more information on this.

## 3.2 Experimental setup

The magnetization of a sample can be measured in several ways. One common method is the vibrating sample magnetometry (VSM) method. The sample oscillates in a homogeneous magnetic field and the absolute magnetization is determined by measuring the induced voltage in pick-up coils. In contrast, magneto-optical measurements provide only a relative change in magnetization. This is achieved by probing the field-dependent polarization rotation or ellipticity change of light in an all-optical setup. This allows for the measurement of ultrafast phenomena such as precession and demagnetization on picosecond and subpicosecond time scales in a pump-probe scheme.

### 3.2.1 Magneto-optical Kerr effect (MOKE)

In 1845, Michael Faraday observed that the polarization of linearly polarized light rotates during transmission through a glass rod when an external magnetic field is oriented parallel to the propagation direction [43]. He noted that the rotation of the polarization is linearly proportional to the external field and that no effect is seen when the magnetic field is perpendicular. Some years later, in 1877, John Kerr published his results on the same observation, but for reflected light [44]. These two related phenomena, now called the Faraday and Kerr effects, are commonly used to measure magnetic behavior [45, 46].
Depending on the orientation of the magnetization in the sample and the angle of incidence of the linearly polarized light on the sample, three types of MOKE effects are distinguished: polar, longitudinal and transverse magneto-optical Kerr effects. These three cases are shown in the figure 3.5. As shown later in figure 3.8, the time-resolved MOKE setup of the UDKM

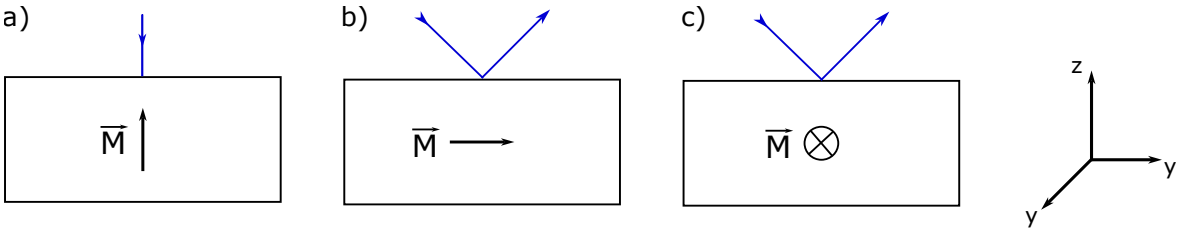


FIGURE 3.5: **Three different MOKE geometries:**. a) polar MOKE b) longitudinal MOKE c) transverse MOKE; the blue line represents the incident and reflected linearly polarised light.

group but can be used for polar Moke measurements. Therefore, this section is limited to this technique. For a more detailed discussion on this topic, specialized literature is recommended [47, 48].
To describe the polar MOKE, it is convenient to think of linearly polarized light as a superposition of left circularly polarized (lcp) and right circularly polarized (rcp) light. A circularly polarized wave propagating along the z-direction is written as

$$\mathbf{E}_{\pm}(\mathbf{r},t) = \frac{1}{\sqrt{2}} E_0 \ (\hat{x} \pm i\hat{y}) \exp\left(ik_z z - i\omega t\right). \tag{3.2}$$

For an observer to whom the wave is moving, a positive helicity means that the electric field rotates counterclockwise. This is called left circularly polarized light. The behavior of an electromagnetic wave in a medium is described by the dielectric tensor $\underline{\epsilon}(\vec{k},\omega)$ or the resulting refractive index $n(\mathbf{k},\omega)$ according to the Fresnel formulas. Due to the low momentum of light quanta in the visible spectrum, the k dependence can be reasonably neglected. For the general case, $\underline{\epsilon}(\omega)$ is rather complicated, since the crystal symmetry and the direction of the magnetic field must be taken into account. For special cases, such as the polar MOKE geometry, the dielectric tensor simplifies [47]. Here the magnetic field pointing in the z-direction introduces off-diagonal terms and $\underline{\epsilon}$ takes the following form

$$\underline{\epsilon} = \begin{bmatrix} \epsilon_{xx} & \epsilon_{xy} & 0 \\ -\epsilon_{xy} & \epsilon_{xx} & 0 \\ 0 & 0 & \epsilon_{zz} \end{bmatrix} \tag{3.3}$$

For the polar MOKE geometry the refractive index for the corresponding circularly polarized wave is written as

$$n_{\pm}^2 = \epsilon_{xx} \pm i\epsilon_{xy}. \tag{3.4}$$

From the definition of the index of refraction

$$\mathbf{n} = c_0/c_{\text{phase}}\,\hat{k} = \frac{c\,\mathbf{k}}{\omega}, \tag{3.5}$$

together with equation 3.2, the reason for the MO Kerr effect becomes obvious, lcp and rcp light have a different index of refraction

$$\mathbf{E}_{\pm}(\mathbf{r},t) = \frac{1}{\sqrt{2}}E_0\ (\hat{x} \pm i\hat{y})\exp\left(i\frac{\omega}{c_0}\,\mathbf{n}_{\pm}\cdot\mathbf{z} - i\omega t\right). \tag{3.6}$$

If the magnetization is non-zero, so is $\epsilon_{xy}$. As a consequence the amplitude and phases of the two reflected modes become unequal. In figure 3.6 the change of amplitude and phase are depicted. At the microscopic level, the origin of the different dielectric functions is highly

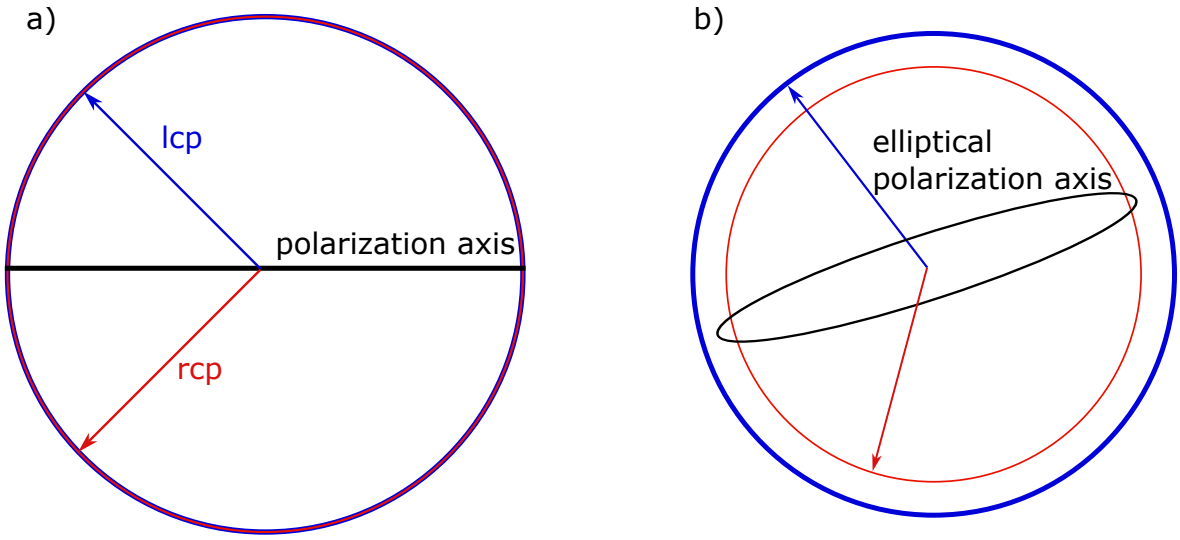


FIGURE 3.6: **Principle of MO Kerr effect:**. a) situation before reflection b) wave after being reflected; in this depiction the change of amplitude and phase of the rcp wave is stronger than for the lcp wave. The phase shift leads to a rotation of the polarization axis and the different amplitudes to Kerr ellipticity.

complex. For an accurate description, the spin and magnetic field dependent shift of the electronic band structure must be considered in the framework of spin density functional theory (SDFT). [49, 50] However, the different dielectric functions for left and right circularly polarized light can also be understood in the context of a simple consideration, as shown in a) Figure 3.7. Suppose there is a transition from a $d$ to a $p$ orbital and the energy levels are split by a magnetic field. The figure shows that transitions with $\Delta m_l = -1$, the transitions excited by lcp, have a smaller energy gap than transitions with $\Delta m_l = 1$. In the plot of the frequency dependent dielectric function, b) figure 3.7, the different transition energies cause the dielectric functions for lcp and rcp to be shifted relative to each other. Consequently, the refractive indices for these two modes are also different.

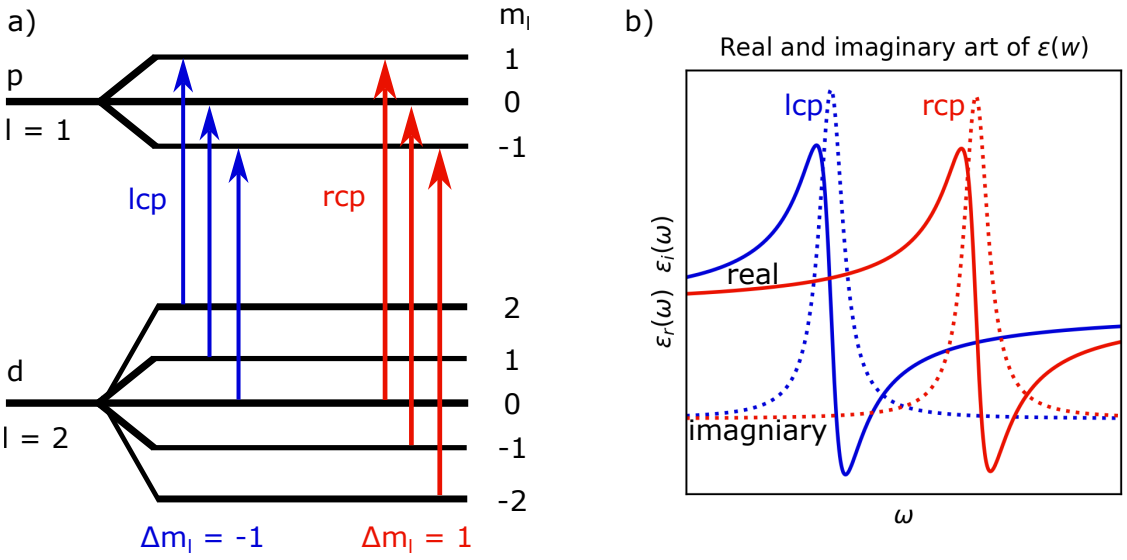


FIGURE 3.7: **Schematic microscopic explanation of MO Kerr effect:**. a) Due to the interaction with the magnetic field, the energy levels split. As a consequence the transition frequency for lcp and rcp become different. b) The real (solid line) and imagniary (dotted line) part of the dielectric function for lcp and rcp light with different transition frequencies.

### 3.2.2 Time-resolved MOKE setup

Ultrafast magnetic phenomena occur on such short time scales that traditional measurement methods, analogous to video recording, are impossible. For this reason, the stroboscopic pump-probe method is used to measure the magnetic response. This method uses a short laser pulse. It is split into a pump, the part that initiates the dynamics, and a probe, the part that measures the response of the sample. By adjusting the time delay between the pump and the probe, it is possible to measure dynamics down to the pulse duration, which can be in the attosecond range [51]. Pump-probe experiments require that the system returns to its initial state between each pump excitation. Time-resolved magneto-optical Kerr effect (trMOKE) experiments based on the pump-probe method are among the most widely used techniques to study magnetization dynamics [23]. The experimental setup used in the UDKM group is shown in the figure 3.8. [18]. It is based on a Ti:Sa laser system that generates laser pulses of about 150 fs with a central wavelength of 800 nm and a repetition rate of 1 kHz. A beam splitter splits the beam into a pump and a probe part. A chopper is used to adjust the repetition rate of the pump to 500 Hz. This ensures that each signal recorded after pumping can be compared to an unpumped signal, which reduces the noise level. Several mirrors direct the pump through the delay stage, controlling the delay between the pump and the probe. A $\lambda/2$ waveplate can be used to adjust the pump power that is transmitted through a Glan-Taylor polarizer. The diameter (0.4 - 1 mm) of the laser spot on the sample can be adjusted by the position and focal length of a focussing lens. To keep the pump spot position constant, part of the pump is directed to a CCD camera. The CCD signal is used to detect and counteract any displacement using a motorized mirror.
A telescope is used to reduce the diameter of the probe. A BBO crystal is then used to double the frequency. This is done to spectrally separate any pump reflected light that may disturb the measured polarization change. Additionally, the Kerr rotation is larger for 400 nm than for 800 nm [52]. The power of the probe beam can also be adjusted using a $\lambda/2$ waveplate. The spot size of the pump ($\approx$ 100 µm in diameter), is much smaller than for the pump ($\approx$

500 µm in diameter). The probe beam is directed perpendicular to the sample surface and reflected from it. The reflected light is passed through a $\lambda/2$ waveplate and a Wollaston prism onto a balanced photodiode. The light is spatially split into p- and s-polarized components in the Wollaston prism and their proportions are measured by a balanced photodiode. The $\lambda/2$ waveplate in front of the Wollaston prism is used to adjust the proportions of p- and s-polarized light before measurement so that the signal from the balanced photodiode is not saturated. A small change in the polarization axis will then result in a measurable voltage difference. Since the Kerr rotation is proportional to the projection of the magnetization direction onto the wave vector of the probe, the magnetization perpendicular to the sample, called $m_z$, is measured in this configuration. The magnetic field in our experiment can be provided in 2 ways, either by an electromagnet, as shown in the figure 3.8, or by a rotatable permanent magnet placed above the sample.

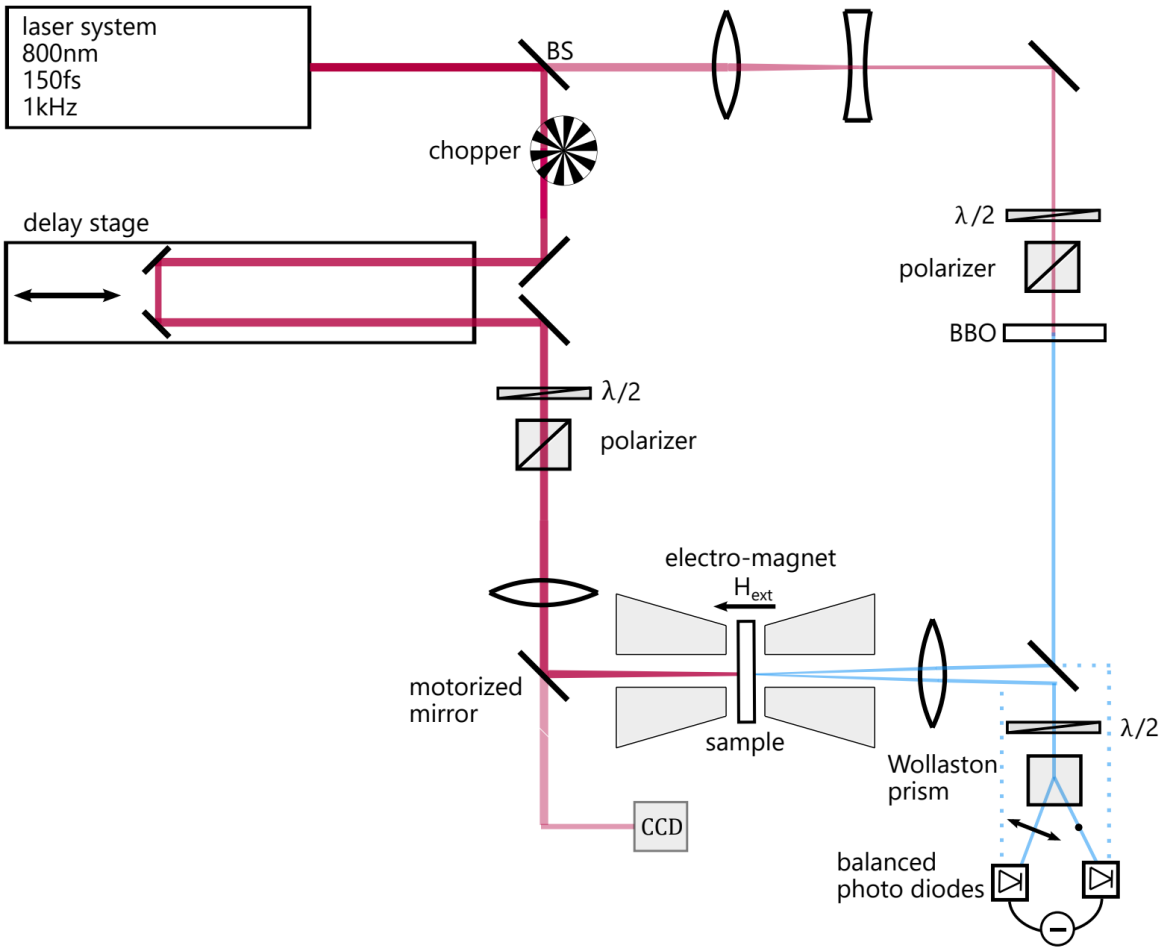


FIGURE 3.8: **Time-resolved polar MOKE setup:** Laser pulses with a cental frequncy of 800 nm are provided by the laser system. The beam is then split into a pump and a probe. Via a chopper the reptition rate of the pump is set to 500 Hz, and it is then directed over a delay stage. The fluence can be set using a $\lambda/2$-waveplate together with a polarizer and a converging lense. The probe is frequency doubled using a BBO crystal to distinguish it from the pump. Its power is adjusted via a $\lambda/2$-waveplate and directed perpendicularly onto the sample's surface. The reflected light is analyzed for polarization changes using a Wollaston prism and a balanced photodiode.

One of the major advantages of all optical setups is their flexibility. For example, the

temporal evolution of the reflectivity can be measured with the same setup by simply flipping a mirror. The reflectivity measurement path is shown by the dotted lines in figure 3.8. The probe pulse must be split into a reference signal going to one diode and a measurement signal reflected from the sample to the other diode. The reflectivity signal is then obtained from the difference between the diode signals. For a more detailed description of the setup, the reader is referred to [53].

# Chapter 4

# Magnetization precession in nickel and cobalt

The dynamics of laser-excited magnetization represents a fascinating and rapidly evolving field of research. Since the first measurements of ultrafast demagnetization dynamics [1, 2], a large number of other phenomena have been observed. These include spintronics [54], all-optical switching [55] and precession [56]. Significant progress has been made in the field of magnetization precession alone. In addition to precession dynamics in ferromagnets [3], high frequency dynamics have also been observed in materials with more exotic ordering phenomena. These include antiferromagnets [57–60] and ferrimagnets [61, 62]. Excitation and detection of higher-order standing spin waves [63, 64], coherent multi-pulse control [57, 65, 66], and inertial effects such as nutation dynamics [9, 10] are only a selection of interesting advances in this field.
After laser excitation, a multitude of effects concurrently influence the effective field and, consequently, the magnetization dynamics. It is challenging to ascertain the relative importance of each effect. Examples of these effects include ultrafast demagnetization, changes in magnetocrystalline anisotropy, magnetoelastic coupling, and during laser excitation, inverse Faraday and Cotton-Mouton effects. However, these effects are strongly influenced by the laser excitation parameters, the sample geometry, and the direction and strength of the external field. In the following we experimentally separate them by an appropriate choice of measurement conditions. In section 4.1 the measurements of the nickel samples described in chapter 3 are compared with simulations performed with the UDKM1DSIM toolbox [17] in combination with a newly developed LLG solver. The possibility to enhance or diminish each effect in the simulations allows for the isolation of the most significant contributions to the magnetization dynamics in the time or frequency domain. This approach provides a comprehensive understanding of the dominant effects that drive the magnetization dynamics. Section 4.2 discusses the magnetization response of the two 20 nm thin cobalt films grown on different substrates. Here the magnetization is not modeled in the same way as in the previous section. The section focuses on describing the influences of various parameters such as the strength or direction of the external field, the fluence, and the substrate on which the samples were grown which influences the anisotropy. The last section 4.3 demonstrates a coherent control scheme where the precession is enhanced or attenuated by a second pump pulse. In this section, the knowledge gained from the previous two sections on the different precession driving mechanisms is employed to control the magnetization by adjusting the pump-pump delay. Here, the nonlinear influence of the demagnetization and the linear strain response is considered, unlike in typical coherent control experiments, where the mechanisms that drive the precession are the same for both pump pulses.

## 4.1 Magnetization response in Nickel films for various excitation conditions

The magnetization dynamics following laser excitation were measured for two distinct samples: a 20 nm thin nickel sample and a 200 nm thick sample. The 200 nm thick sample was measured under two distinct measurement geometries: frontside excitation, where the pump and probe pulses are on the same side of the sample, and backside excitation, where the pulses are on the opposite sides. In this experiment, the influence of direct and indirect laser excitation of the magnetization is investigated. For the 20-nm-thin sample, only measurements for backside excitation are shown. A rotating permanent magnet was used to vary the direction of the external field. The measured results and a sketch of the measurement geometry are shown in figure 4.1. The measurements on the 20 nm thin film in figure

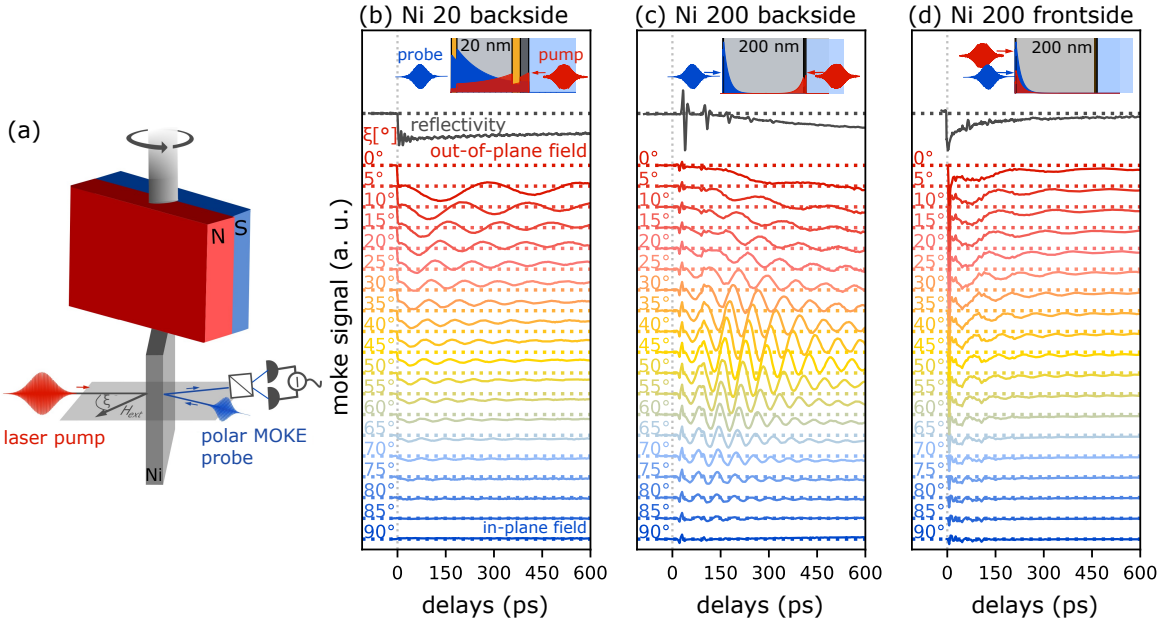


FIGURE 4.1: **Sketch of the setup and measurement results of the rotation series:** (a) Sketch of the trMOKE setup in the backside pump, frontside probe geometry. The permanent magnet provides a magnetic field of about 400 mT at the probe position. (b) Measurement of the 20 nm sample, the upper right sketch shows the measurement geometry, the gray line shows the time resolved change of the reflectivity and the colored lines show the measured magnetization dynamics for the external field angles from 0-90°, (c) Same as (b), but here the dynamics of the 200 nm thick film for the backside pump are shown. (d) Shows the results of the 200 nm thick film in the front side configuration The measurements were made at 3mJ/cm², 23mJ/cm² and 12mJ/cm² respectively.

4.1 (b) show an initial fast demagnetization. The magnetization then processes with an amplitude and frequency that depend on the field angle. While the amplitude of the signal decreases as the angle increases, the frequency of the precession increases. The reflectivity signal shows a step-like change, followed by very fast, strongly damped oscillations, and a persistent periodic signal. The strongly damped oscillations in the first 50 ps indicate sound waves generated by the rapid expansion of the nickel layer. These sound waves propagate through the nickel layer. The persistent periodic signal can be identified as a Brioullin oscillation. Since a certain portion of the probe pulse penetrates the substrate, as shown in the optical penetration profile in figure 4.1 (c) above, the interaction of the light with the sound waves in the substrate leads to alternating constructive and destructive interference. The

frequency of these oscillations is given by [67]

$$f_B = \frac{2\,n\,v}{\lambda}, \tag{4.1}$$

where $n$ is the index of refraction, $v$ is the speed of sound in the substrate, and $\lambda$ is the wavelength of the probe pulse. Plugging the substrate parameters from the 4.1 table into this equation yields a frequency of 42.8 GHz. This is in reasonable agreement with an FFT analysis of the reflectivity, which gives a frequency of 44.5 GHz.
The trMOKE measurement of the 200 nm thick film in the backside excitation geometry, figure 4.1 (c), shows a slow demagnetization on the scale of hundreds of ps. The precession frequency increases with increasing external field angle, as in the case of the 20 nm thick film, while here the precession amplitude increases until it starts to decrease after an angle of about 45°. It is interesting to note that the precession amplitude increases within two periods at these optimal angles. Like the demagnetization, the change in the reflection shows slow dynamics on a time scale of a few hundred ps. In addition, the propagation of sound waves through the sample is clearly visible. Their repetition time is 69 ps. For a 200 nm thick nickel layer, this gives a sound velocity of 5.8 nm/ps, which is used in the simulations.
The 200 nm thick nickel film behaves in a very similar way to the 20 nm thick film in the first picoseconds, the magnetization decreases rapidly on a very short time scale. This is followed by remagnetization on a time scale of about 100 ps and magnetization precession. Again, as with the 20 nm sample, the amplitude decreases at higher angles. As with all samples and measurement geometries, the frequency simultaneously increases. The reflectivity signal shows a steep drop followed by a recovery similar to the trMOKE signal. In addition, as with the other geometries, sound waves can be seen, but they are less pronounced than in the case of excitation from the backside.
A convenient way to visualize this dataset is to calculate an FFT of the angle-resolved data and fit it to obtain the amplitude and frequency of the magnetization precession for the different angles. Figure 4.2 shows the amplitude and precession frequency as they change with the direction of the external field. Figure 4.2 (a) shows the change in amplitude as a function

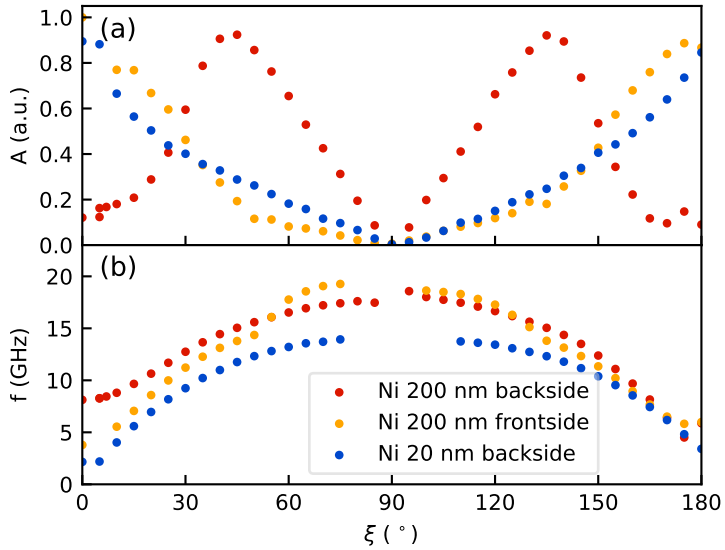


FIGURE 4.2: **Angle-resolved amplitude and precession frequency:** (a) normalized amplitude (b) precession frequency; is shown for the different samples and geometries.

of the external field angle. The 20 nm and 200 nm samples, the latter one excited from the front have their maximum at an external angle of 0°. In contrast, the 200 nm sample excited from the back has its maximum precession amplitude at about 45°. The plot of the precession frequency versus angle (b) shows a similar trend for all samples. For higher angles, the frequency increases up to about 17 GHz. However, it can be seen that the frequencies for the 20 nm film are slightly lower than those for the 200 nm film. The differences between the measurements for the 200 nm sample can be attributed to small differences in the distance and orientation of the permanent magnet.
The data raises three questions that will be answered in the following sections using simulations of the dynamics of temperature, strain, and magnetization.

1. How can the reflection measurements be understood? This is done by simulating the temperature and strain response of the samples using the UDKM1DSIM toolbox. The change in reflectivity is then linearly approximated by the change in temperature and strain in the probed region.

2. What is the reason for the increase in precession frequency as a function of angle, can it be calculated analytically? The Smit-Beljers formalism is the method of choice. It expresses the precession frequency analytically as a derivative of the free energy. The frequency for different external field angles is recovered using the parameters found in section 3.1.1.

3. Why do the 20 nm and 200 nm samples show a maximum precession amplitude at 0° for the front side excitation and the 200 nm sample shows a maximum at 45° for the back side excitation? In particular, why is the precession amplitude of the 200 nm back-excited sample highest at 45°, but not for the 200 nm front-excited sample? This is done by modelling the response of the magnetization via the non-norm conserving LLG equation as described in section 2.3.3. The simulation of strain and temperature and the magnetic parameters from section 3.1.1 are used to obtain a model of the measured magnetization dynamics for the different orientations of the external field. The simulations show that for the 20 nm and 200 nm samples in front-side excitation, quasi-statice strain is the driving mechanism for precession. For the 200 nm sample in backside excitation, strain pulses lead to a resonant enhancement of the precession.

In the following subsections, I will address these questions and explain the basic mechanisms driving precession based on the measured data and simulations.

### 4.1.1 Temperature and strain dynamic

The time dependent change of the reflectivity $\Delta R(t)$ is modeled by linearizing it with the change of the electron, the phonon temperature and the strain in the nickel layer [**https://doi.org/10.1002/pss** 68]:

$$\Delta R(t) = \frac{\partial R}{\partial T_\mathrm{e}} \Delta T_\mathrm{e}(t) + \frac{\partial R}{\partial T} \Delta T_\mathrm{p}(t) + \frac{\partial R}{\partial \eta} \Delta \eta_\mathrm{acc}(t), \tag{4.2}$$

where $\Delta T_\mathrm{e}(t)$ and $\Delta T_\mathrm{p}(t)$ are the electron and phonon temperature changes, and $\Delta \eta_\mathrm{acc}(t)$ is the acoustic strain including quasi-static strain and the strain pulses. To calculate the change in reflectivity, the temperature and strain response must first be calculated for the specific sample and excitation geometry. This is done using the UDKM1DSIM toolbox. For the simulation of the samples the parameters specified in the table 4.1 were used. The results of the simulations for temperature and strain are shown in the figures 4.4, 4.5 and 4.6. All these figures follow the same format. On the left side the spatio-temporal temperatures

| Element | Nickel | Platinum | Tantalum | PGO |
|---|---|---|---|---|
| heat capacity lattice (J/kg K) | 442 | 133 | 139 | 708 |
| Sommerfeld constant (J/kg K²) | 0.12 | 0.034 | 0.023 | none |
| thermal conductivity electrons phonons (W/m K) | 81.4<br>9.6 | 66<br>5 | 52<br>5 | 0<br>2 |
| electron-lattice coupling ( W/m³ K) | $1 \cdot 10^{17}$ [39] | $3.75 \cdot 10^{17}$ [70] | $3.75 \cdot 10^{17}$ | none |
| linear thermal expansion coefficent lattice (1/K) | $20.2 \cdot 10^{-6}$ [71] | $8.9 \cdot 10^{-6}$ | $12.4 \cdot 10^{-6}$ [72, 73] | $8.7 \cdot 10^{-6}$ |
| linear thermal expansion coefficent electrons (1/K) | $3.88 \cdot 10^{-9}$ [74] | $20.2 \cdot 10^{-6}$ [71] | $2.11 \cdot 10^{-9}$ | none |
| sound velocity (nm/ps) | 5.8 | 4.24 | 4.24 [73] | 5.7 |
| refractive index for 800 nm & 400 nm | 2.3223+8.8820i<br>1.7163+2.5925i<br>[75, 76] | 0.57617+8.067i<br>1.0433+3.0855i<br>[75] | 0.99181+7.293i<br>1.3259+3.5442i<br>[75] | 1.5 |
| density (g/cm³) | 8.91 | 21.45 | 16.68 | 2.49 |

TABLE 4.1: **List of the simulation parameters:** All other not referenced parameters are taken from Pudell 2020 [77]

for the electron and phonon system and the resulting strain are shown for the case where only quasi-static strain ($\eta_{\mathrm{qs}}$) and quasi-static strain together with strain pulses ($\eta_{acc}$) are considered. The right side shows the temperature and strain response in the probed region. This is calculated by weighting these variables with an exponential function with the same profile as the optical penetration depth of the probe. This weighted temperature and strain response is used to model the laser-excited reflectivity response and magnetization dynamics.

The simulations in figure 4.4 show the dynamics for the 20 nm thin nickel film in backside excitation. The electronic system shown in (a) and (e) heats up first and then transfers its heat to the phonon system (b) and (f) within a few picoseconds. The temperature of the phonon is in equilibrium with the temperature of the electrons within 8 ps. The strain induced by the heat alone largely follows the shape of the phonon temperature. On longer time scales (g) the strain becomes smaller due to heat diffusion into the substrate. The propagation of sound waves is shown in the acoustic strain map (d). The platinum layer immediately adjacent to the nickel layer are the main source of these waves, as this small layer absorbs a lot of energy.

The simulations in figure 4.5 show the dynamic response of temperature and strain for the 200 nm thick nickel layer in the backside excited case. Again, the electrons first heat up and

then transfer their heat to the phonon system (b) within a few picoseconds. (e,f,g) shows that heat is transported through the sample on longer time scales. The acoustic strain map (d) shows the propagation of sound waves reflected at the interfaces.
The simulations in figure 4.6 show the dynamics for the 200 nm thick nickel film for frontside excitation. Again, the electrons first heat up and then transfer their heat to the phonon system (b). Again, heat is dissipated on longer time scales, but now away from the probed region rather than into it, as shown in (e,f,g). (d) shows the propagation of sound waves reflected at the interfaces, as in the simulation for the backside excited sample.
The reflectivity changes for the different samples and excitation geometries can now be computed from the simulations and the extracted temperature and strain response in the probed region using the equation 4.2. The best agreement with the normalized reflectivity signal for all these samples and excitation conditions was found for $\frac{\partial R}{\partial T_e} = -0.090$, $\frac{\partial R}{\partial T_p} = -0.019$ and $\frac{\partial R}{\partial \eta} = -1.0$. The simulated reflectivity dynamics along with the measured data are shown in figure 4.3. Within this simple model, the simulated reflectivity change agrees well with

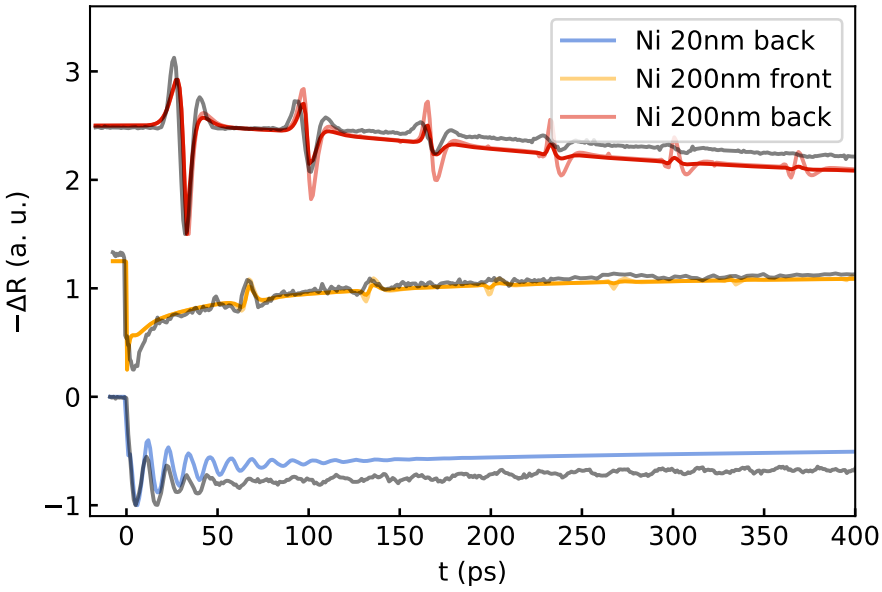


FIGURE 4.3: **Simulated and measured reflectivity response:** for the nickel samples under different excitation conditions. The darker colored lines for the 200 nm sample, indicate the response where the strain pulses are manually damped.

the measured reflectivity response. Because this model is relatively simple, there are several reasons for the differences between the simulations and measurements. On the one hand, the measured dynamics of the total reflectivity results from the change in reflectivity of the platinum and nickel layers. However, the strain in the platinum layer is not treated differently from the strain in the Nickel layer since this would double the fit parameters. There are several plausible reasons why the simulation shows longer and sharper strain pulses than the corresponding measurement, as shown by the dark and light red and yellow curves in figure 4.3. The actual impedance matching between the tantalum and platinum layers is unknown. In addition, the dispersion of the sound waves, which could broaden them, and the roughness of the interfaces, which attenuates the sound waves, are not included in the UDKM1DSIM toolbox. The dark red and yellow lines in figure 4.3 are obtained by damping each strain pulse with an exponential decay. This corrected strain is used for further simulations of the magnetization dynamics.

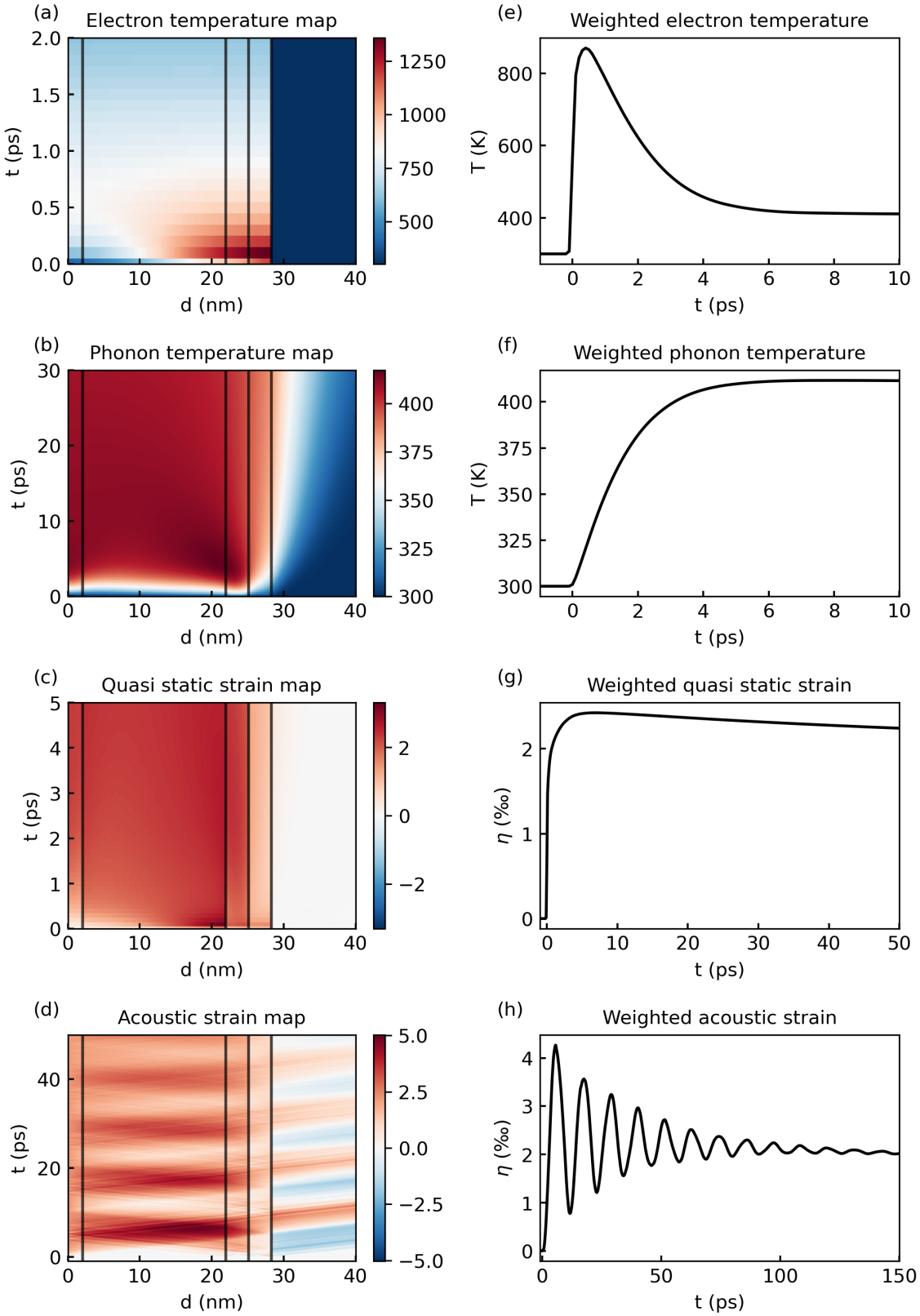


FIGURE 4.4: **Simulated strain and heat dynamic for Ni 20 nm (backside excitation):** (a) electron temperature map (b) weighed phonon temperature (c) calculated strain considering only heat (d) calculated strain with hypersound (e) weighed electron temperature (f) weighed phonon temperature (g) weighed strain (only heat) (h) weighed strain (with hypersound); the black lines in the colormaps indicate the interfaces between different materials. By applying an exponential profile onto the Ni data at the probe position (left side), the weighted temperature and strain dynamic is calculated.

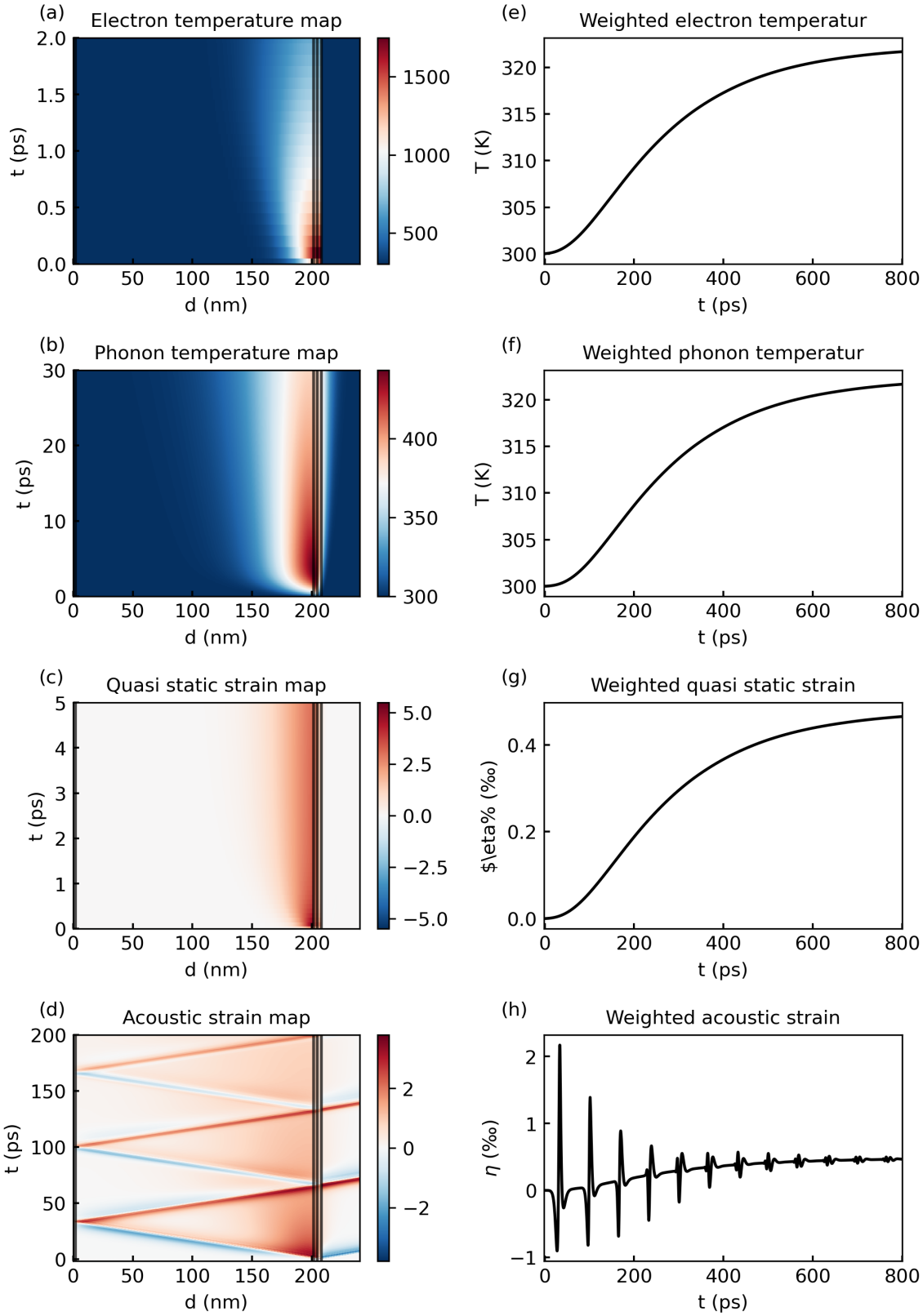


FIGURE 4.5: **Simulated strain and heat dynamic for Ni 200 nm (backside excitation):** (a) electron temperature map (b) weighed phonon temperature (c) calculated strain considering only heat (d) calculated strain with hypersound (e) weighed electron temperature (f) weighed phonon temperature (g) weighed strain (only heat) (h) weighed strain (with hypersound); the black lines in the colormaps indicate the interfaces between different materials. By applying an exponential profile onto the Ni data at the probe position (left side), the weighted temperature and strain dynamic is calculated.

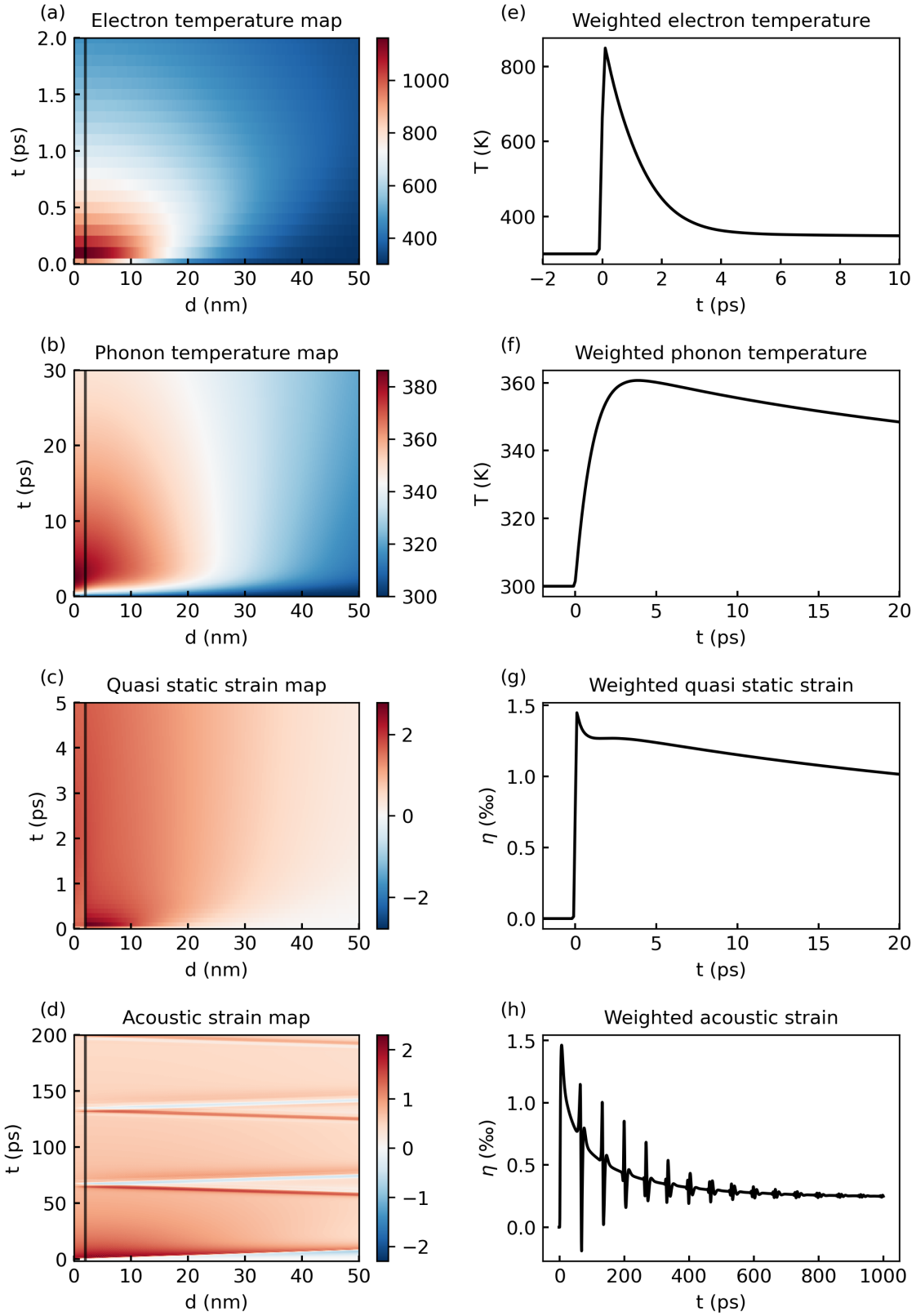


FIGURE 4.6: **Simulated strain and heat dynamic for Ni 200 nm (frontside excitation):** (a) electron temperature map (b) weighed phonon temperature (c) calculated strain considering only heat (d) calculated strain with hypersound (e) weighed electron temperature (f) weighed phonon temperature (g) weighed strain (only heat) (h) weighed strain (with hypersound); the black lines in the colormaps indicate the interfaces between different materials. By applying an exponential profile onto the Ni data at the probe position (left side), the weighted temperature and strain dynamic is calculated.

### 4.1.2 Calculation of precession frequency

In the literature, measurements of the FMR frequency as a function of the external field strength are often fitted with the Kittel formula [78]. In this context, two different measurement techniques are distinguished: either the external field is parallel or perpendicular to the sample plane. A more general description of the FMR as a function of the external field is provided by the Smit-Beljers formalism [42]. This formalism has the advantage that for any configuration of the external field where $m_z \neq 1$, the FMR frequency can be calculated. A convenient notation, which avoids the unphysical behavior near $m_z = 1$, is given by [25]:

$$\left(\frac{\omega}{\gamma}\right)^2 = \frac{1}{M_s^2}\left[F_{\theta\theta}\left(\frac{F_{\phi\phi}}{\sin^2\theta} + \frac{\cos\theta}{\sin\theta}F_\theta\right) - \left(\frac{F_{\theta\phi}}{\sin\theta} + \frac{\cos\theta}{\sin^2\theta}F_\phi\right)^2\right]. \tag{4.3}$$

Here $\omega$ is the precession frequency, $\gamma$ is the gyromagnetic ratio, $M_s$ is the saturation magnetization, and the lower indices indicate the derivative of the free energy in spherical coordinates. For the 20 and 200 nm nickel film the free energy for the case $\eta = 0$ is the sum of the Zeeman energy $F_{\text{Zee}}$ and the effective anisotropy $F_{\text{eff}}$. The magnetic parameters from table 3.1 were used to compute the precession frequency. First the initial position of the magnetization has to be calculated. This is done numerically by minimizing the free energy, since it is not possible to calculate the initial position of the magnetization for any orientation of the external field analytically. Then the free energy and the corresponding derivatives are calculated and inserted into equation 4.3. In figure 4.7 this method is compared with measurements of the precession frequency for different angles of the external field. Given the experimental conditions, especially since the field is quite inhomogeneous for a permanent magnet, the data is well described by the chosen set of parameters. It should be emphasized that the chosen parameters not only describe the precession frequency well, but also the hysteresis curves shown in the figure 3.2.

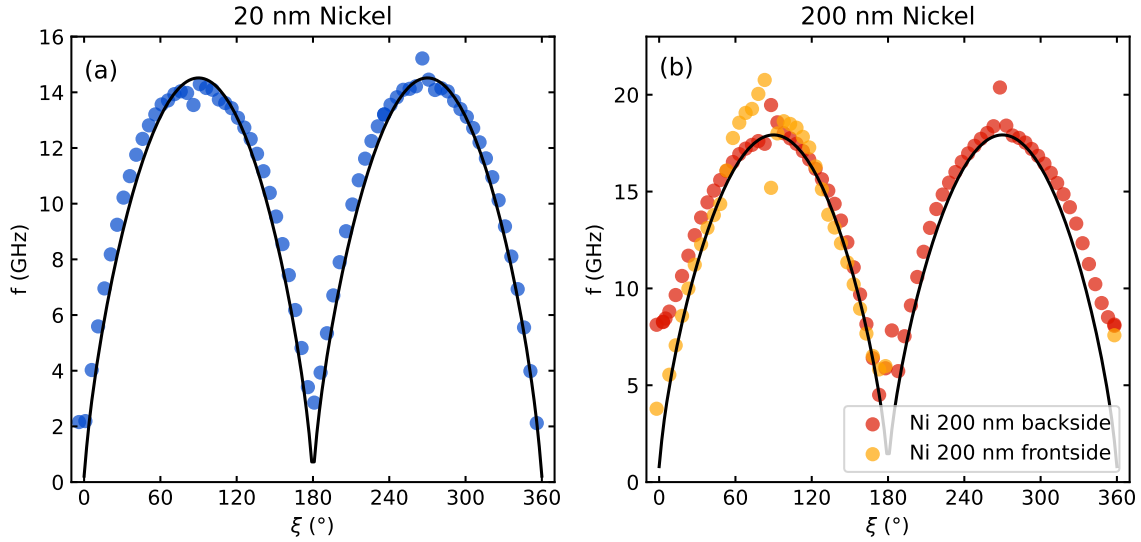


FIGURE 4.7: **Simulated precession frequency:** Angle-dependent precession for the 200 nm (a) and that for the 20 nm thin sample (b). The same parameters were used as in table 3.1, the Landé factor was set to g = 2.1. For the simulation in (a) left, an external field of 360 mT was assumed, for the simulation shown in (b) the external field is set to 430 mT.

### 4.1.3 Modelling the amplitude of precession

To model the angle ($\xi$) dependent amplitude of precession, we simulate the dynamics of the magnetization. The effects of strain and heat on the magnetization must be explicitly calculated numerically since because the LLG equation is nonlinear. In this way, the complex interaction between heat, strain and magnetization can be studied. For this purpose the modified LLG equation (2.39) is used, which combines demagnetization and precession.

$$\begin{aligned}\frac{\partial \boldsymbol{m}}{\partial t} &= m\frac{\partial \mathbf{m}}{\partial t} + \mathbf{m}\frac{\partial m}{\partial t} \\ &= -m\left[\frac{\gamma\mu_0}{1+\alpha^2}\mathbf{m}\times\mathbf{H}_{\text{eff}} + \frac{\gamma\alpha\mu_0}{1+\alpha^2}\mathbf{m}\times(\mathbf{m}\times\mathbf{H}_{\text{eff}})\right] + \mathbf{m}\frac{\partial m}{\partial t}\end{aligned} \tag{4.4}$$

The effective field, which captures the influence of strain and demagnetization on precession, is given by the equation 2.16

$$\mathbf{H}_{\text{eff}} = \mathbf{H}_{\text{ext}} - H_{\text{sat}}m_{\text{z}}\mathbf{e}_{\text{z}} + H_{\text{uni}}m_{\text{x}}\mathbf{e}_{\text{x}} + H_{\text{me}}m_{\text{z}}\mathbf{e}_{\text{z}} \tag{4.5}$$

The interplay of these two equations governs the magnetization dynamics. In other words, the magnetization determines where the effective field points, and the effective field determines how the magnetization moves.
A widely used approach to solving the differential equations numerically is the RK4 method. The RK4 method works by calculating the rate of change of the magnetization at four different points within each time step. These four derivatives are then combined into a weighted sum to produce a refined estimate of the rate of change of the system over the entire time step. The weights assigned to each derivative are tailored to counteract the lower-order error terms. This improves the overall accuracy of the method. The RK4-LLG solver is written in C++, but it can be imported as a library and used in Python.
For the simulation of the dynamics of the magnetization, the simulated response of heat and strain calculated in section 4.1.1 is used. To account for demagnetization, the magnetization is assumed to be in thermal equilibrium with the phonon system. This means that the amplitude of the magnetization is approximated by setting the temperature in the equation 2.27 to the phonon temperature and solving this equation for each time step and the corresponding phonon temperature. This approximation is suitable for describing these experiments because the fluence is relatively small. Thus, the phonon temperature is far from the ferromagnetic phase transition. In addition, the goal of this chapter is the description of the precession ($\approx$ 50 - 100 ps)., not the description of the ultrafast demagnetization ($\approx$ 100 fs). Since these two phenomena occur on rather different timescales, and the electrons and phonons thermalize rapidly ($\approx$ 5 ps as described in section 4.1.1), the temperature dependent magnetization is assumed to be determined by the phonon temperature. The simulations show remarkably good agreement with the measurements. This is even more impressive since the system is described by a single macrospin. It is therefore not surprising that larger deviations occur in thicker, inhomogeneously excited layers. In addition, deviations in the backside excitation can be attributed to the fact that the overlap between pump and probe pulse was not optimally adjusted. A possible improvement of the overlap due to instabilities during a measurement could explain why the measured precession amplitude increases more than in the simulations. The deviations in the first picoseconds for the frontside excitation can be explained by the fact that this model does not include ultrafast demagnetization. Another reason is that the exact temperature change of the sample is not known. In order to better describe the dynamics on femto- to picosecond time scales, further measurements are needed, e.g. to calibrate the strain and also the temperature using UXRD measurements.

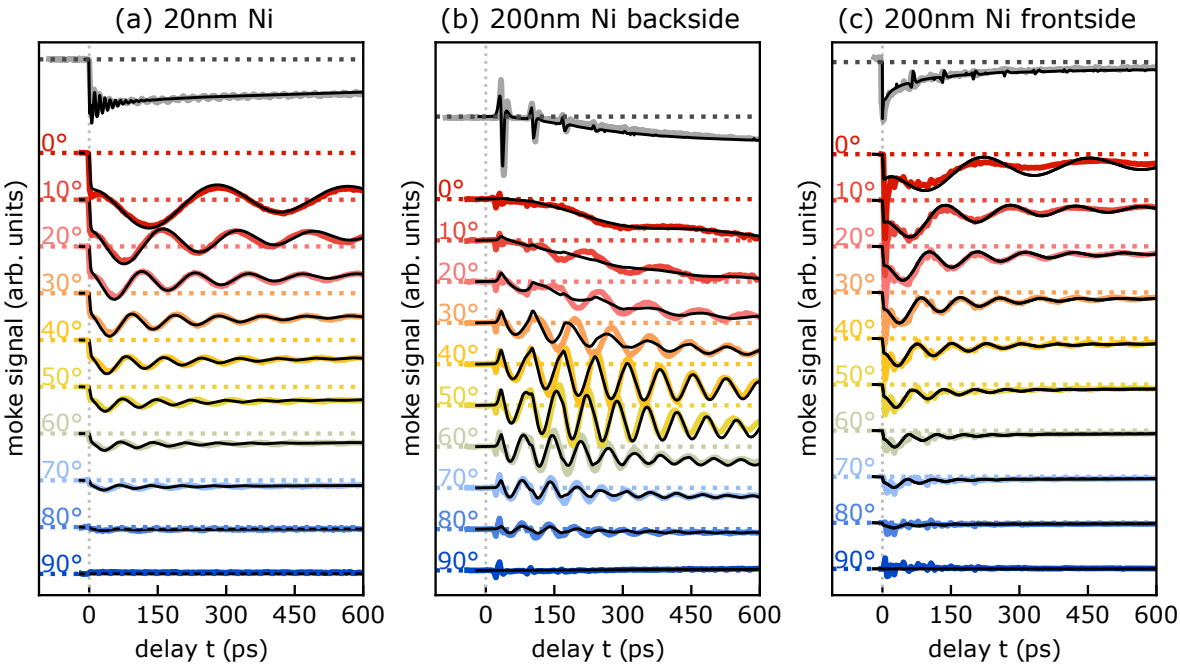


FIGURE 4.8: **Simulated magnetization dynamic in Ni:** The angle-dependent precession for the (a) 20 nm sample (b,c) 200 nm sample in backside and frontside excitation are shown together with their corresponding simulated dynamic (black line). In the top of the figures the reflectivity is shown with the simulated reflectivity discussed in section 4.1.1. The simulations in (b) needed to be scaled by a separate factor for each measurement in order to achieve the best possible fit. For (a) and (c), a single scaling factor was used for each set of measurements.

Simulations of temperature and strain dynamics with the UDKM1DSIM toolbox help to reveal the different influences on the precession dynamics. By switching different contributions on and off, it is possible to investigate which contribution has the strongest influence on the magnetization dynamics when inserting the timeresolved average strain and temperature in to the LLG equation. For this purpose, 5 different simulations for the different samples and excitation geometries are compared in figure 4.9. In the first simulation only the quasi-static strain (only qs) is considered as the driving mechanism. The laser-generated strain pulses and the quasi-static strain are included in the second model called s. In a third scenario, only demagnetization is used as the driving mechanism. The last two models combine demagnetization with quasi-static strain and demagnetization with quasi-static strain plus strain pulses. Figure 4.9 shows the simulated precession dynamics for the 20 nm sample for these 5 different models. In the lower half of the figure, the resulting precession amplitude and frequency are plotted for the different angles of the external field. The upper part of Figure 4.9 clearly shows that it has no significant effect on the precession whether the quasi-static strain with or without strain pulses is included in the model. This is true for both the case where demagnetization is ignored and the case where demagnetization is included. This is reasonable since the acoustic pulses generated in the 20 nm thin sample have such a short travel range that their repetition rate $f = 149\,\mathrm{GHz}$ is significantly higher than the precession frequency. Comparing the simulations with and without demagnetization, two differences stand out. The first is obviously the nearly instantaneous reduction of $m_z$ in the first picosecond. The second is that the precession amplitude for the simulations with demagnetization is significantly smaller than for the simulation without demagnetization. This is particularly evident in Figure 4.9 (b). At small angles, the amplitude of the

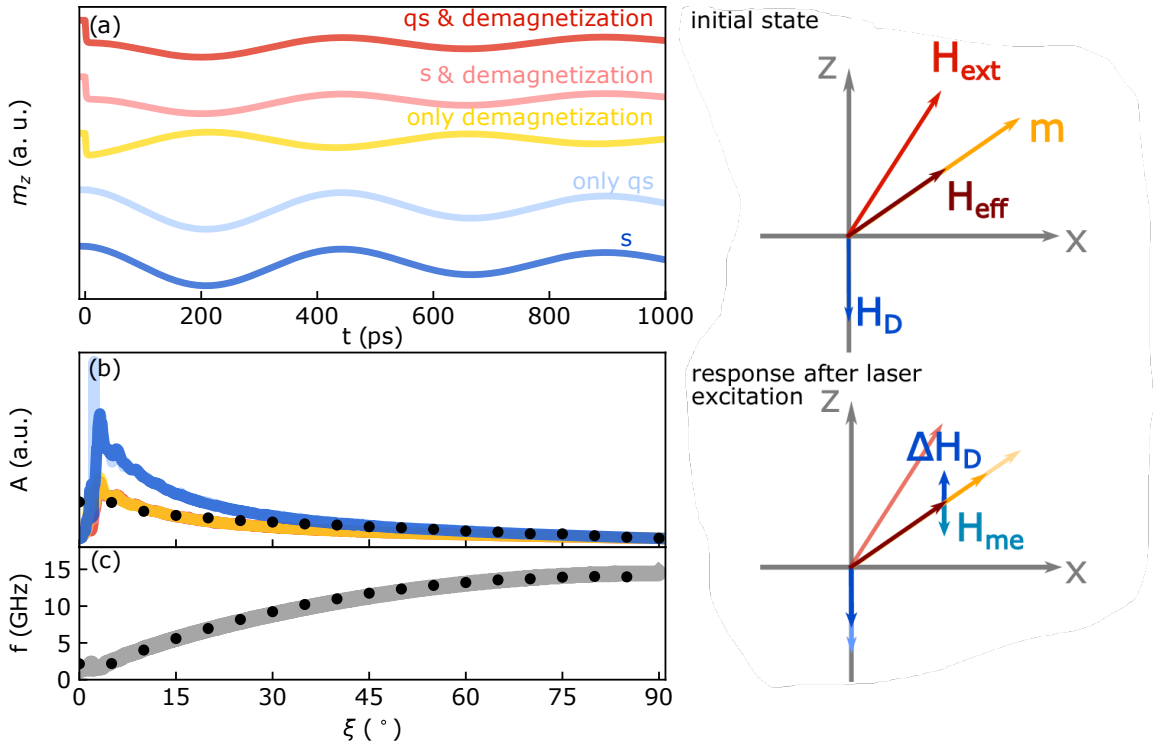


FIGURE 4.9: **Comparison of different excitation mechanisms for Ni 20 at $\xi = 5$:** The simulated precession dynamics for the 5 different models are shown in (a). (b) shows the precession amplitude for the different orientations of the external field. Here the yellow and red curves overlap over a large range of angles. (c) illustrates the angle-dependent precession frequency. These curves overlap for all models. On the right side, the mechanisms responsible for precession are illustrated. Before laser excitation, the effective field points in the same direction as the magnetization. After laser excitation, 2 simultaneous processes take place. First, demagnetization causes the demagnetization field to be reduced. As a result, the effective field is rotated out of the sample plane. Second, thermal expansion and the associated strain cause a magneto-elastic field that pushes the effective field into the sample plane.

simulations without demagnetization is almost four times larger than that of the simulations with demagnetization. The reason for this can be seen in the simulation in which only the demagnetization has been included in the model. Compared to the other simulations with demagnetization, this simulation shows the same degree of demagnetization in the first picoseconds, but the phase of the precession is shifted by 180 degrees. While here the precession starts with an increase in $m_z$, the simulations with demagnetization and strain show that the precession starts with a decrease of the $m_z$ component. This shows that the precession dynamics caused by demagnetization are opposite to those caused by strain, due to the positive magnetoelastic coupling parameter in nickel. The influence of demagnetization and quasi-static strain on the effective field is shown in on the right in Figure 4.9. For simplicity, the influence of the uniaxial field in the x-direction is neglected. The change in the effective field after laser excitation is determined by both the demagnetization and the quasi-static strain. The demagnetization influences the demagnetization field and the strain influences the magnetoelastic coupling field. The change of these contributions to the

effective field is given by

$$\Delta \mathbf{H}_D = -M_{sat}^{eff} \Delta m_z \mathbf{e}_z, \tag{4.6}$$

$$\Delta \mathbf{H}_{me} = -\frac{b_1 \eta}{\mu_0} m_z \mathbf{e}_z. \tag{4.7}$$

Demagnetization implies a negative $\Delta m_z$, which causes the effective field to be directed out of the sample plane. Since the magnetoelastic coupling is positive for nickel, a positive strain will direct the effective field into the sample plane. A comparison of the simulations and measurements for the 20 nm sample (Figure 4.8) reveals that the quasi-static strain must be the dominant factor, as the dynamics always start with a decrease of the $m_z$ component
The simulations for the 200 nm thick sample in front-side excitation are shown in Figure

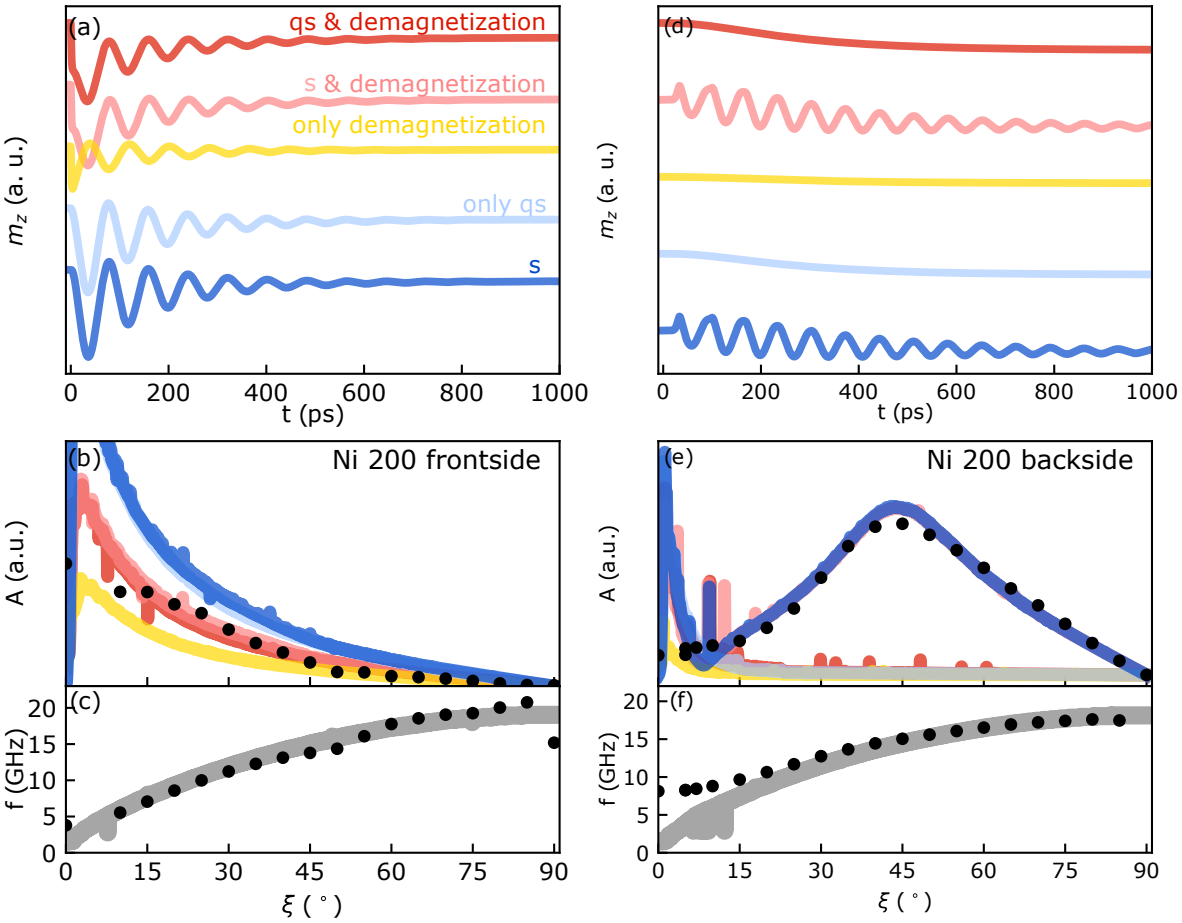


FIGURE 4.10: **Comparison of different excitation mechanisms for Ni 200 in frontside (a-c) and backside (d-f) excitation at $\xi = 45$:** The simulated precession dynamics for the 5 different models are shown at in (a,c). (b,e) shows the precession amplitude for the different orientations of the external field. Here the yellow and red curves overlap over a large range of angles. (c,f) illustrates the angle-dependent precession frequency.

4.10 (a-c). The simulations for the different mechanisms show a similar behavior as for the 20 nm thick sample. (a) shows the dynamics at an angle of 45°. There are no differences when comparing the quasi-static strain simulations with and without strain pulses. This is also true for the simulations with and without demagnetization. The simulation with only demagnetization as a driving factor also shows the same differences to the simulations with both demagnetization and strain as it does for the thin sample. The demagnetization

causes the precession to start with an increase of the $m_z$ component, while the quasi-static strain causes the precession to start in the opposite direction. (b) shows the amplitude of the precession for the different field configurations. Again, it can be seen that it makes little difference whether the quasi-static or the acoustic strain simulation is used. The angle dependent precession frequency shown in (c) agrees well with the measured data. It can therefore be concluded that the quasi-static strain is also the driving factor for the precession here. The amplitude of the precession is also reduced by the demagnetization.
The simulation results for the 200 nm thick nickel layer in backside excitation are shown in figure 4.10. Panel (d-e) shows the dynamics for the different models at an external field of 45°. The situation is clearly different from the 20 nm thin film. It can be seen that the demagnetization has almost no effect on the magnetization dynamics. The reason for this is that with indirect excitation, the temperature change in the probed region is small because the heat is dissipated throughout the sample. Additionally, diffusion through 200 nm takes a long time as shown in the temperature and strain simulations (figure 4.5). Although the quasi-static strain clearly affects the magnetization, it does not cause precession. To induce magnetization precession, a rapid change in the effective field is required. In this case, this rapid change is achieved only by the strain pulses. Thus, the strain pulses are the driving factor of the precession dynamics. Figure 4.10 (e) Shows the angle dependent amplitude of the precession for the different excitation mechanisms. Again, demagnetization and quasi-static strain have no effect on the precession. The reason why the precession amplitude is highest at an angle of 45° is that at this angle the precession frequency is equal to the strain pulse repetition rate with $f = 14.5\,\mathrm{GHz}$. This results in resonant amplification of the precession.
To explain why the strain pulses have such a small effect on the precession dynamics, simulations where only the quasi-static strain was used are compared with simulations where only the strain pulses were used to drive the precession. The following figure shows the driving strain and the resulting precession for these two cases. Figure 4.11 clearly demon-

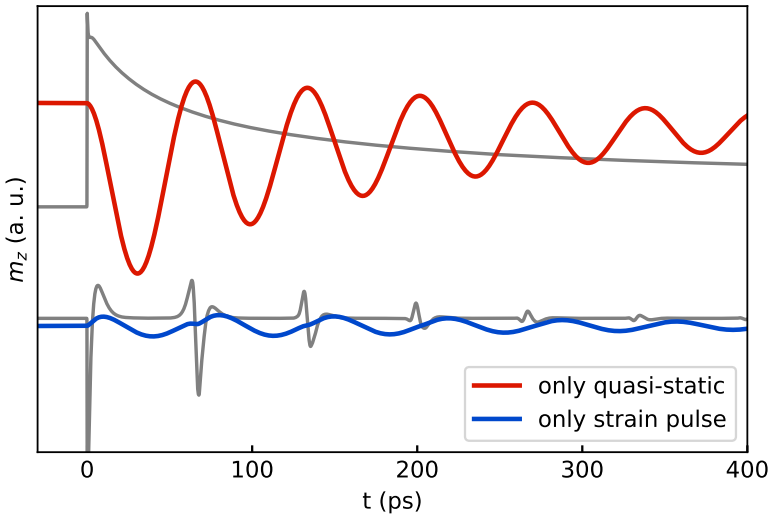


FIGURE 4.11: **LLG simulations using quasi-static strain and strain waves for frontside excitation:** The precession resulting from the strain pulses is smaller and has a different phase

strates that for frontside excitation, where both mechanisms are active the, precession dynamics triggered by the strain pulses have a significantly smaller amplitude. In addition there is a phase shift compared to the dynamics triggered by quasi-static strain. This phase

shift ensures that the strain pulses do not amplify the precession triggered by the quasi-static strain in frontside excitation, making their influence negligble.

## 4.2 Laser induced precession in Cobalt

Cobalt is very similar to nickel. In both materials, the atomic 3d orbitals are responsible for the ferromagnetic behaviour. In contrast to nickel, cobalt has a much higher Curie temperature of 1423 K, a higher saturation magnetization, a different crystalline arrangement (hcp) at room temperature, and a much stronger magnetocrystalline anisotropy[79]. The free energy for these samples is expressed as a combination of a Zeeman contribution, effective anisotropy, magnetocrystalline anisotropy for a hexagonal system, and magnetoelastic coupling.

$$\begin{aligned} F &= F_{Zee} + F_{\text{shape}}^{\text{eff}} + F_{\text{mc}}^{\text{hex}} + F_{\text{me}} \\ &= -\mu_0 M_s \, \boldsymbol{m} \cdot \mathbf{H}_{\text{ext}} + \frac{\mu_0}{2} M_s^2 \left( N_x^{\text{eff}} m_x^2 + N_z^{\text{eff}} m_z^2 \right) + K_1 m_z^2 + K_2 m_z^4 + b_1 \eta m_z^2 \end{aligned} \tag{4.8}$$

Neglecting the higher order magnetocrystalline anisotropy $K_2$, the effective field is given by equation 2.16

$$\mathbf{H}_{\text{eff}} = \mathbf{H}_{\text{ext}} - H_{\text{sat}} m_z \mathbf{e}_z + H_{\text{uni}} m_x \mathbf{e}_x + H_{\text{me}} m_z \mathbf{e}_z \tag{4.9}$$

The saturation field $H_{\text{sat}}$ consists of the effective anisotropy in z-direction and the first order term ( $K_1$) of the magnetocrystalline anisotropy.

In the following, the magnetization dynamics of two cobalt samples grown on different substrates are compared. Since the values of the different contributions to the free energy are essential for a numerical description of the precession, but the samples have not been studied by FMR, the main focus of this section is on the phenemenological description of the dynamics. The dynamics of the magnetization are not modeled, but the different measured trends of the measurement series and possible differences between the measured samples are explained. This is mostly done by describing how the effective fields react after laser excitation, as this drives the precession. Three different series of measurements are compared and described. First, the behavior of the magnetization with perpendicular field orientation and different field strengths is studied. Then the influence of the incident pump fluence is examined for the perpendicular field orientation. Finally, the dynamics for different orientations of the external field are discussed.

### 4.2.1 Field series

The measurements and simulations of the 20 nm thin nickel layer showed that the precession is driven by the quasi-static strain and demagnetization. This is also the case for the Cobalt samples, as indicated by the fact that the precession dynamics starts with a decrease of the $m_z$ component. The change in reflectivity, shown in figure 4.12 (a) and (b), provides information about the temperature and strain response after laser excitation. The electrons are heated by the optical excitation and couple to the phonons. The deposition of energy in these systems creates a stress that causes strain. The heat is dissipated into the substrate over long time scales, as indicated by the slow recovery of reflectivity. Because only slow phononic conduction occurs in the glass substrate, this time scale is quite slow. Notably in these two measurements, especially in the JGS2 sample, another fast oscillation is seen in addition to the precession. This oscillation is independent of the external field strength

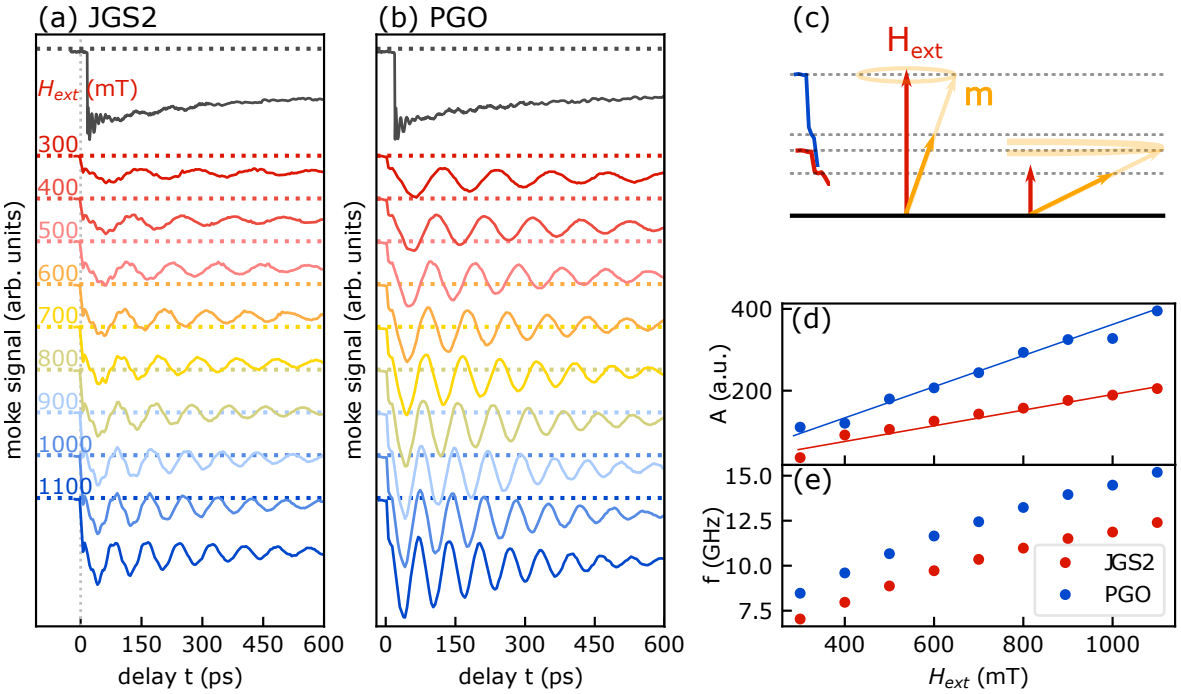


FIGURE 4.12: **Field series of 20 nm Co on JGS2 and PGO in backside excitation:** For different field strengths, the precession dynamics of cobalt grown on (a) JGS2, (b) PGO at an excitation fluence of 6.3mJ/cm² are shown. (c) illustrates the measured dynamic for the first picoseconds after laser excitation and increase of $\Delta m_z$ via demagnetization for increasing external fields, (d) shows the linear growth of the amplitude with increasing external field. In (e) the field dependence of the precession frequency is plotted.

and has a frequency of 50 GHz. Since the dynamics of the magnetization is expected to be strongly dependent on the external field strength, the cause of these field-independent oscillations is not attributed to the dynamics of the magnetization. Instead, we attribute them to the Brioullin oscillations described in section 4.1. In the reflectivity, this oscillation at 50 GHz can be seen, as well. This corresponds to a strain pulse propagating in the substrate with a sound velocity of about 6.6 nm/ps (equation 4.1). The measured dynamics are very similar for both substrates. For higher fields, the amplitude of the ultrafast demagnetization and the precession frequency increase. In (c) the mechanism responsible for the increase in $\Delta m_z$ via demagnetization is shown. For a perpendicular external field, the initial magnetization is on a cone of minimum free energy. For the same change of $|m|$, the observed change in the $m_z$ component is maximized when the magnetization points out of the plane. As higher fields tilt the magnetization more and more out of plane, the observed demagnetization increases. The linear increase in precession amplitude with higher magnetic fields can be understood by comparing the initial magnetization with the equilibrium position after laser excitation. Figure 4.13 illustrates the initial and final states of magnetization.

Neglecting possible small anisotropies that do not depend on $m_z$, the initial position of the magnetization in the case of an external field smaller than saturation, perpendicular to the surface, is obtained by setting $H_{\text{eff}}$=0. For simplicity, we consider only linear dependence of $m_z$, then the initial position of the magnetization can be found by setting

$$\boldsymbol{H}_{\text{ext}} + \boldsymbol{H}_{\text{D}} = H_{\text{ext}} - M_s^{\text{eff}}\, m_z^{\text{in}} = 0. \tag{4.10}$$

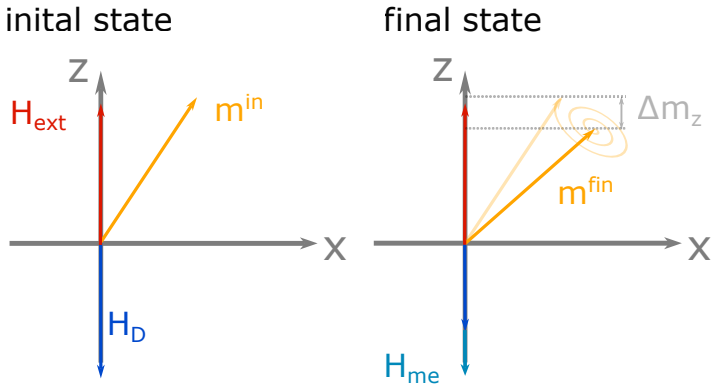


FIGURE 4.13: **Comparison of initial and final state:** Negecting small anisotropies, the initial magentization is determined by the external field and the saturation field. The orientation of the magnetization after laser excitation is also determined by the magnetoelastic coupling field. It can be seen that the measured precession amplitude is approximately determined by $\Delta m_z$.

Quasi-static strain is the dominating mechanism for precession in Cobalt [14]. Neglecting all other effects the effective field after laser excitation is given by

$$\boldsymbol{H}_{\text{ext}} + \boldsymbol{H}_{\text{D}} + \boldsymbol{H}_{\text{me}} = H_{\text{ext}} - M_{\text{s}}^{\text{eff}}\, m_{\text{z}}^{\text{fin}} + \frac{2\, b_1\, \eta}{\mu_0\, M_{\text{s}}}\, m_{\text{z}}^{\text{fin}} = 0 \tag{4.11}$$

By substituting the difference of the $m_z$ component $\Delta m_z = m_z^{\text{in}} - m_z^{\text{fin}}$ into 4.11, solving this system of equations for $\Delta m_z$ and assuming that $M_s^{\text{eff}} \gg \left|\frac{2\, b_1\, \eta}{\mu_0\, M_s}\right|$ one finds that

$$\Delta m_z \approx \frac{2\, b_1\, \eta}{\mu_0\, M_s\, M_s^{eff}}\, m_z^{in} \tag{4.12}$$

In this simplified model, according to equation 4.10, the initial position of the magnetization in the z-direction depends linearly on the strength of the external field. This agrees well with the almost linear increase in precession amplitude in figure 4.12 (d). This equation only holds if $H_{\text{ext}} < H_{\text{sat}}$. Above this limit, the inital effective field is larger than zero. If the laser induced magneto-elastic field is smaller than the initial effective field, no precession is expected since the equilibrium position of the magnetization does not change.

The two samples show differences in their dynamics. In particular, the amplitude of the precession dynamics for the sample grown on PGO sample is much more pronounced than for the JGS2 sample. There are several possible reasons for this.

1. The magnetoelastic coupling may be stronger for the PGO sample due to different crystallographic textures. According to equation 4.12, a higher magneto-elastic coupling increases the strain-induced displacement of the magnetization and causes the precession amplitude to be significantly larger.

2. The magnetocrystalline anisotropy is very high in cobalt. In contrast to nickel, dynamical effects such as the temperature dependent change of the anisotropy (section 2.1.5) should therefore play a more important role in driving the precession [80]. Different anisotropies in the two samples could also explain the different field dependent frequency in figure 4.12 (e).

3. The external field may be slightly different in the two measurements. Since the amplitude of the precession depends sensitively on the initial magnetization, different

orientations of the magnetization would lead to different amplitudes. This would also explain why the precession frequencies are so different, since the precession frequency at small field angles is also strongly influenced by the orientation of the external field.

### 4.2.2 Fluence series

The field series was performed at medium fluences of 6.3mJ/cm², where quasi-static strain controls the magnetization dynamics. In order to create a change to precession controlled by demagnetization, a series of measurements was taken at increasing incident fluence. The results are shown in figure 4.14 The measurement series for (a) JGS2 and (b) PGO clearly

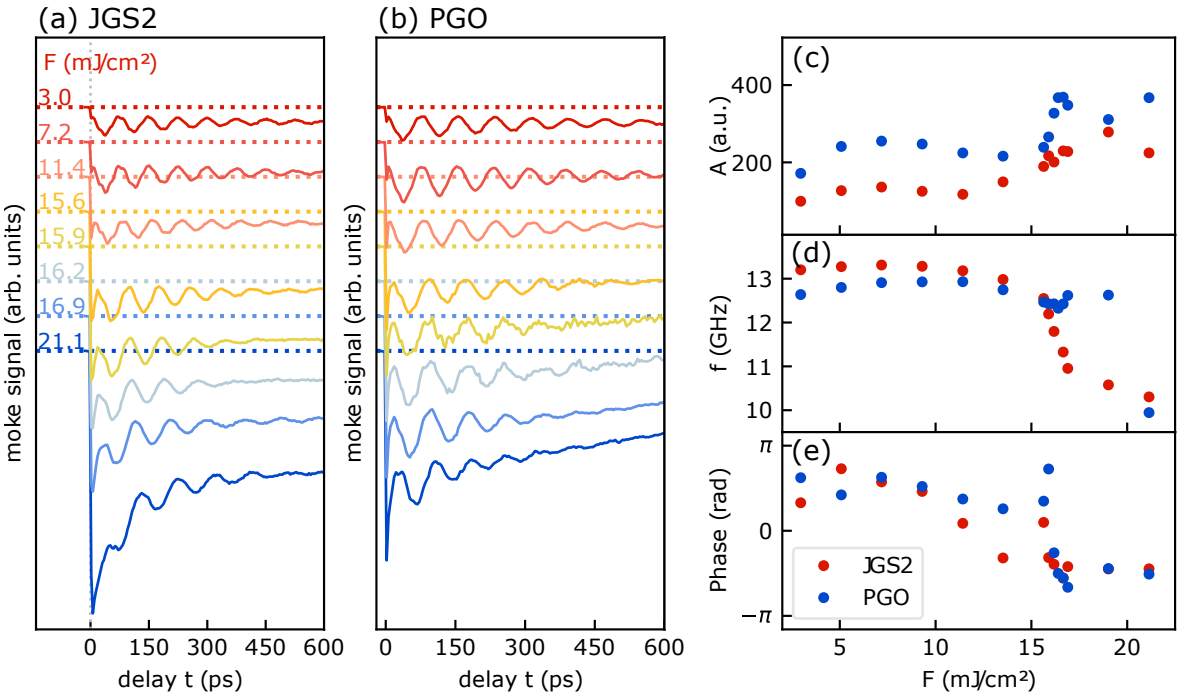


FIGURE 4.14: **Fluence series of Co on JGS2 and PGO in backside excitation:** For different excitation fluences the precession dynamics of (a) 20 nm Cobalt on JGS2, (b) cobalt on PGO at an external field of 1.1T are shown. (c) Fluence dependence of the precession amplitude, (d) precession frequency and (e) the phase of the frequency.

show that the demagnetization increases with increasing fluence. In addition, there is a noticeable difference in the amplitude of the demagnetization, especially when comparing the two samples at maximum excitation. The JGS2 sample, measured under the same conditions, shows a much larger amplitude of demagnetization. The reason for this could be that there are also differences in the initial position of the magnetization. If the initial magnetization for the JGS2 sample is stronger along the z-axis, then the change in the $m_z$ component measured in the polar MOKE should also be stronger.
It is particularly characteristic of this series of measurements that an alternation between precession driven by quasi-static strain and precession driven by demagnetization is visible for both samples. While at low fluences the precession starts with a decrease in $m_z$, at high fluences the precession starts in the opposite direction´after the ultrafast demagnetization. This change between the excitation mechanisms is also shown in figure 4.14 (e). The phase of the precession frequency calculated from the FFT is plotted. It is clear to see how the phase reverses with increasing fluence. Similar results that indicate this change of the driving mechanism were found by Shin et al. for NiFe [13]

The measured precession frequency of the two samples shown in (d) are closer together in this measurement than in the field series shown in figure 4.12 (d). This is a clear indication that the two measurements do not have exactly the same field configuration. If the sample is tilted by a small angle, the precession frequency should also change significantly. This becomes apparent from measurements with rotatable magnet near $\xi = 0$ . In figure 4.14 (d), we see that the precession frequency initially increases with increasing fluence, but then decreases sharply. This sharp decrease is due to the increase in demagnetization, which does not scale linearly with fluence. In the context of the LLG equation, a lower amplitude of magnetization results in a lower frequency.

### 4.2.3 Rotation series

The precession dynamics of the cobalt samples were investigated using a rotating permanent magnet. The results of this series of measurements are shown in figure 4.15. The rotation series clearly shows that the precession frequency increases as the angle of the external field to the surface normal increases. At the same time, as shown in (c), the amplitude of the precession also decreases. This decrease can be understood in the context of equation 4.12. For larger angles of the external field to the surface normal, the initial $m_z$ component becomes smaller and so does the displacement between the initial and final states of the magnetization.

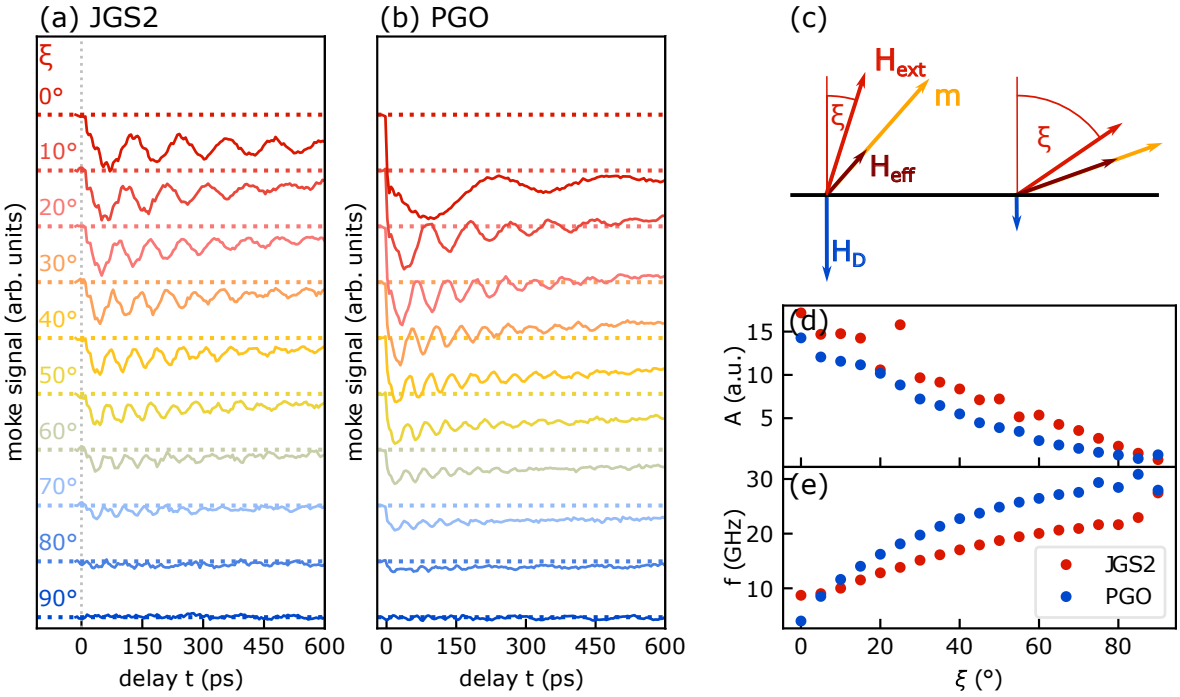


FIGURE 4.15: **Rotation series of Co on JGS2 and PGO in backside excitation:** For different external field orientations, the precession dynamics are (a) of 20 nm cobalt on JGS2, (b) cobalt on PGO at an excitation fluence of 6.3 mJ/cm². (c) illustrates the increase of the effective field for higher angles of the external field. (d) shows the angular dependence of the precession amplitude and (e) the precession frequency.

It is interesting to note that high frequencies of up to 30 GHz can be achieved with the rotating magnet, although the permanent magnet used can only generate fields of about 400 mT. The reason for the high precession frequency is the orientation of the external field and the resulting strength of the effective field. Figure 4.15 (c) shows the effective field for 2 different

angles of the external field. If the small contributions to the effective field, that are proportional to $m_x$ are neglected, the external field in the x-direction cannot be compensated. As a result, the effective field and thus the precession frequency increases with increasing angle. The behavior of the frequency in this series of measurements is strongly influenced by the anisotropy fields present. The significant difference between the angle-dependent precession frequencies of the two samples demonstrates that they have different anisotropies. This is in accordance with the X-ray diffraction measurements shown in section 3.1.2. These measurements show that the cobalt sample grown on JGS2 has a stronger diffraction signal for the c-axis of hexagonal cobalt than the sample grown on PGO. The different crystalline structures can strongly affect the anisotropy of the sample.

## 4.3 Coherent control using double pulse excitation

Understanding the mechanisms that drive the precession allows for controlling the magnetization dynamics. This is achieved in coherent control experiments where the magnetization precession is excited by two pulses and the dynamics is controlled by adjusting the pump-pump delay [81–84]. Usually, the mechanism driving the precession is the same for both pump pulses and constructive interference is observed when the two pulses are seperated by multiples of the period $T$ of the dynamics. As can be seen from previous experiments in chapter 4.2.2, it is possible to switch between two different excitation mechanisms if the magneto-elastic coupling is negative. The excitation mechanisms are the quasi-static strain, which scales linearly with the fluence, and the non-linear change in the demagnetizing field caused by demagnetization. In the following, the coherent control by means of double pulse excitation is combined with a control of two different mechanisms responsible for the precession by adjusting the fluence. The experiments were performed using the 20 nm thin nickel film and published together with M. Mattern [85].
Figure 4.16 (a) shows the fluence-dependent magnetization dynamics after single laser excitation. With increasing fluence, the demagnetization and the amplitude of the precession continue to increase. For fluences above 2.9mJ/cm², the precession amplitude then decreases so that the amplitudes at 5 and 0.7 mJ/cm² become comparable.

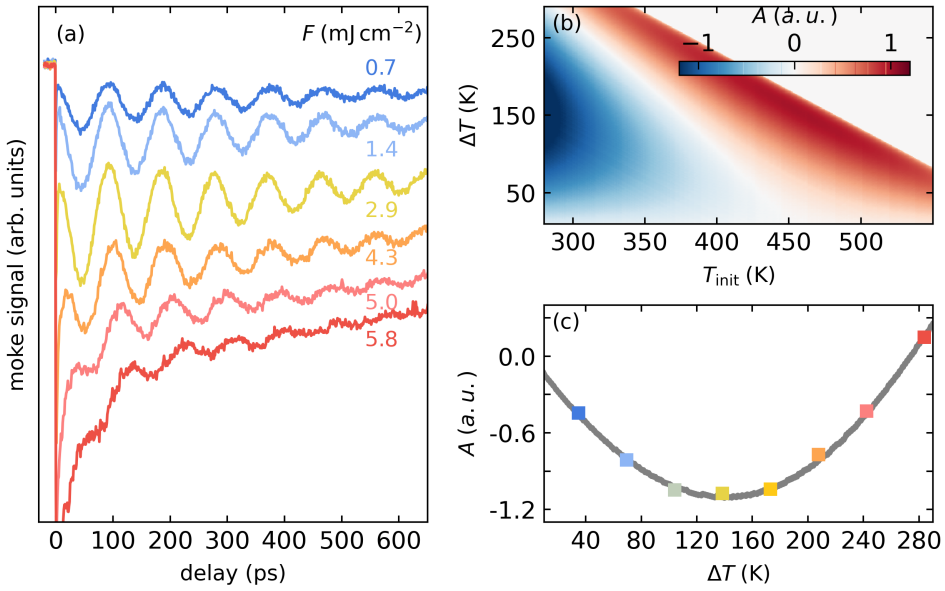


FIGURE 4.16: **Measurement and simulation of fluence-dependent precession amplitude :** (a) Fluence-dependent magnetization precession upon a single excitation for an external field of 350 mT at 35° with respect to the sample surface normal. (b) Amplitude of the precession A as function of the laser-induced temperature rise in the phonons $\Delta T$ and the sample temperature before excitation $T_{init}$ The arrows visualize the measurement series in (a) and figure 4.17 . (c) The modelled precession amplitude as function of $\Delta T$ at $T_{init}$ = 300 K (solid line) corresponds to the left arrow in (b) and captures the measured amplitude of the fluence series in (a) (coloured symbols)

Figure (b) illustrates how the precession amplitude is determined by the "initial" temperature caused by the first laser pulse and by the change in temperature $\Delta T$ caused by the second pulse. A red color means that the precession is predominantly driven by demagnetization, and the blue color means that quasi-static strain prevails as driving mechanism. The precession amplitude is determined by the torque acting on the magnetization $\mathbf{A} = \Delta\mathbf{H}_{eff} \times \mathbf{M}$. The change of the effective field results from the contributions of the demagnetizing field and the magnetoelastic coupling. The change in magnetization, and the resulting change of the demagnetizing field is described using the formula for temperature-dependent magnetization in the context of mean-field theory. The change of the magneto elastic field is determined by the quasi-static strain which is calculated using $\eta = \alpha\Delta T$. The parameters used are the same as those already employed in section 4.1 for the simulation of the 20 nm thin nickel sample. The gray line in Figure 4.16 (c) shows the modeled precession amplitude curve for different temperature changes $\Delta T$ where the initial temperature is $T_{\text{init}} = 300\,\text{K}$. This curve can be compared with the fluence series show in figure 4.16 (a). Assuming that a change in phonon temperature of 34.5K is driven by an excitation fluence of 0.7 mJ/cm², the model shows good agreement with the fluence-dependent amplitude (colored symbols) extracted from a fit of the transient magnetization by an exponential decaying background and a damped oscillation. With increasing fluence, the precession amplitude increases up to a temperature change of $\Delta T = 140\,\text{K}$. After that, the amplitude decreases again due to the non-linear increase in demagnetization. For changes above 270 K, demagnetization becomes the dominant mechanism for precession dynamics.
Figure 4.17 compares in the left column the dynamics when the sample is excited with one (dashed lines) and both laser pulses (solid lines). The right column shows the difference

between these two measurements. The oscillation amplitude of the difference signal represents the change caused by the second pulse. In Figure 4.17 (a) and (b) the fluence of the first pulse $F_1$ is varied while the fluence of the second pulse $F_2 = 1.8\,\mathrm{mJ/cm^2}$ is kept constant. This corresponds to a variation of $T_{init}$ with a constant change in temperature of $\Delta T = 85\,\mathrm{K}$. In (b), the sign of the precession amplitude is clearly changed, due to the change of the precession-driving mechanism. The effect of the second pulse changes from a strengthening of the precession for small $F_1$ to an attenuation for $F_1 = 4.3\,\mathrm{mJ/cm^2}$.
The change between the mechanisms dominant for the precession can also be realized by varying the pump-pump delay. In this case, the second pump-pump delay is selected so that it always coincides with the maximum of precession triggered by the first pulse. The measurements are shown in figures 4.17 (c) and (d). The fluences of the two pulses are $F_1 = 2.8\,\mathrm{mJ/cm^2}$ and $F_2 = 1.8\,\mathrm{mJ/cm^2}$. A transition from demagnetization to quasi-static strain as a driver of the precession triggered by the second pulse is visible between $\Delta t = 94$ and 188 ps. This is in good agreement with the model, where $T_{init}$ decreases with increasing delay. While for small delays, the precession of the first pulse is attenuated, as demagnetization driven precession has an opposite phase, the precession is in turn enhanced for larger delays. This effect would be even stronger if the substrate had a higher thermal conductivity. If the nickel layer had been grown on MgO, for example, an even stronger change between attenuation and amplification would be visible.
In Figure 4.17 (e) and (f) a different method for changing the dominant mechanism for a fixed fluence of the first pulse $F_1 = 1.1\,\mathrm{mJ/cm^2}$ is shown. For increasing fluence of the second pulse, the precession triggered by the second pulse initially increases, but then decreases again from a fluence of $F_2 = 2.2\,\mathrm{mJ/cm^2}$. At the highest fluence of $4.7\,\mathrm{mJ/cm^2}$, the effect of demagnetization is strong enough to switch off the precession. The effect, depends strongly on the fluence of the first pulse. In Figure 4.17 (g) and (h) the situation is illustrated for a first excitation fluence of $F_1 = 4.3\,\mathrm{mJ/cm^2}$. The excitation fluence is now so large that for any fluence of the second pulse $F_2$ the dominant mechanism is demagnetization. This leads to the observation that if the second pulse occurs at the maximum of the precession, the precession is attenuated for each fluence $F_2$.

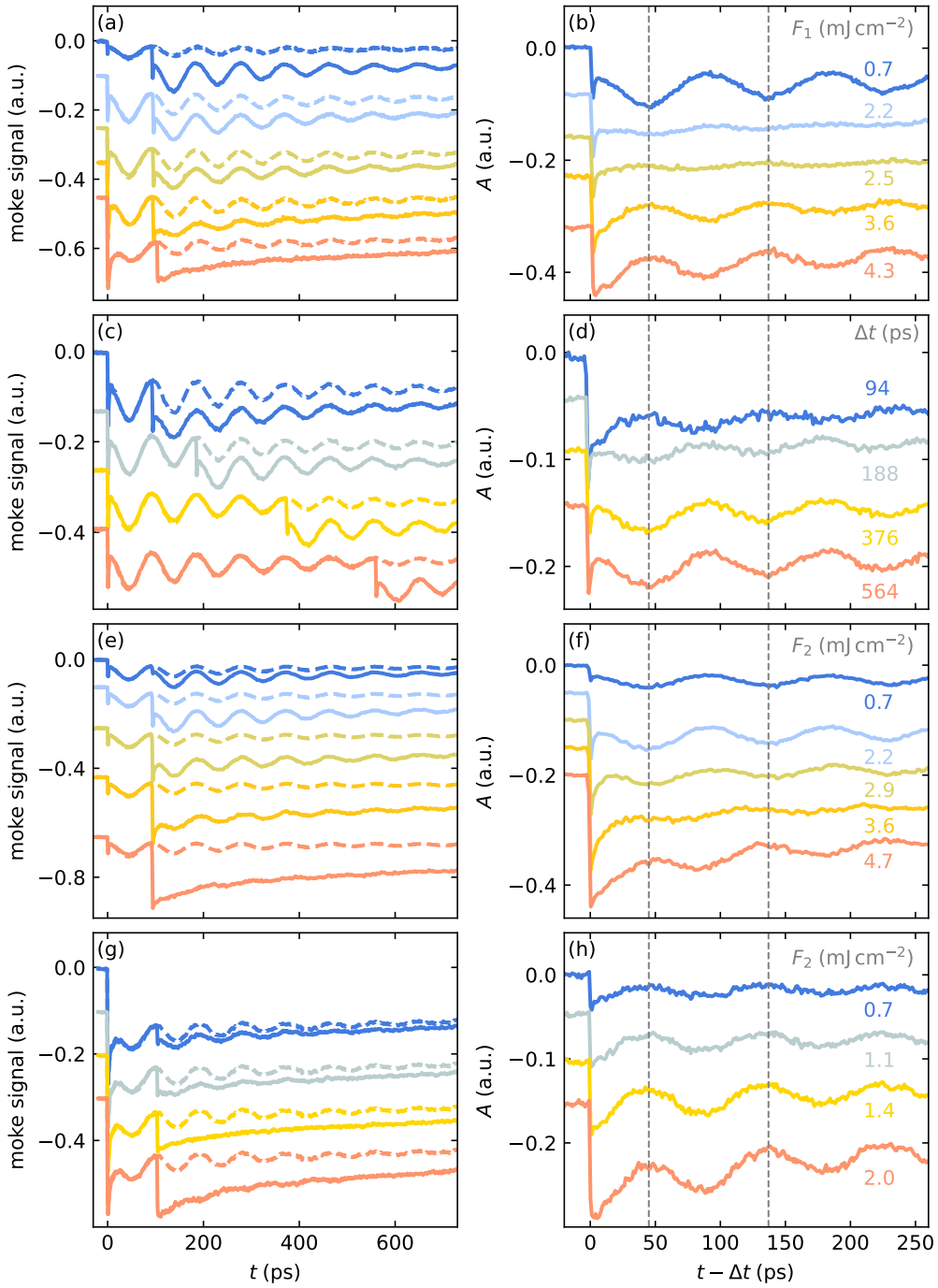


FIGURE 4.17: **Control of the magnetization precession via double-pulse excitation by tuning the effect of the second pulse:** (b,d,f,h) Difference in the magnetization upon both excitations (solid lines) and only the first excitation (dashed lines) in panels (a,c,e,f), respectively. (a,b) Variation of fluence of the first pulse for constant $F_2$ = 1.8 mJ/cm² . (c,d) Variation of the pump-pump delay for constant $F_1$ = 2.8mJ/cm² and $F_2$ = 1.8 mJ/cm² . Note that the second pulse is chosen to pump at the same precession phase at all chosen $\Delta t$ and nonetheless has an effect on the phase for varying $\Delta t$. (e,f) Variation of the fluence $F_2$ for constant $F_1$ = 1.1 mJ/cm² . (g,h) Variation of the fluence $F_2$ for constant $F_1$= 4.3 mJ/cm² . The difference in panels (b,d,f,h) demonstrate a tuning of the dominant driving mechanism for the second excitation, which we utilize to selective control the magnetization precession upon double-pulse excitation in panels (a,c,e,f)

# Chapter 5

# Conclusion and Outlook

## 5.1 Conclusion

The magnetization precession in nickel and cobalt was measured as an integral part of this work. The aim was to model and understand the precession dynamics and to identify the mechanisms that drive them. To describe precession and demagnetization, the magnetization vector, $\boldsymbol{m}$, is partioned into two components: direction, $\hat{m}$, and length, $|m|$. By measuring the magnetic hysteresis the saturation field was estimated as a preliminary approximation. Further FMR measurements, which were conducted exclusively on nickel samples, the various contributions to the free energy could be quantified. The fourth chapter addresses the issue of precession measurements for the different samples. The first section focuses on the realistic modeling of the magnetization dynamics in the nickel samples. Given the availability of FMR measurements and the associated precise knowledge of the effective field, the nickel samples are particularly suitable for investigating the magnetization dynamics within the framework of numerical models. This requires knowledge of the thermal response of the sample system and the strain, as these control the magnetization dynamics. To this end, the UDKM1DSIM toolbox was employed to virtually reconstruct the samples and describe the heat propagation and the induced strain subsequent to laser excitation via a one-dimensional model. Upon weighting the change in temperatures of the electron and phonon systems and the strain with the penetration depth of the probe beam, the change in reflectivity over time can be adequately described linearizing it in terms of electron-, phonon temperature and strain. The resulting change in phonon temperature is used to describe the demagnetization in the context of the modified LLG. This approximation is only valid for small temperature changes in the measured range and on the time scales >10 ps relevant for the precession. In the model, demagnetization and the strain have an influence on the precession. Demagnetization leads to a reduction in the saturation field, while the magnetoelastic coupling field is increased by the strain. For nickel, the magnetoelastic coupling constant $b_1 > 0$ is positive, so that the two mechanisms act in opposite directions after laser excitation. The simulated magnetization dynamics accurately describe the measured dynamics in the nickel samples within the scope of the approximations. By switching the various mechanisms that trigger the precession dynamics on and off, it is possible to investigate the driving forces behind the magnetization precession. The quasi-static strain, which is caused by the thermal expansion, is responsible for the precession dynamics of the 20 nm thin nickel sample as well as the 200 nm thick nickel sample in frontside excitation. However, the effect of demagnetization should not be overlooked, as this significantly reduces the amplitude of the precession. For the 200 nm thick nickel sample, strain pulses are responsible for the precession dynamics, provided that the repetition rate of these pulses matches the precession frequency. The course of the precession frequency, which depends on the angle of the external field, was also investigated using the Smit-Beljers formalism, which further confirms the magnetic anisotropy parameters. No FMR measurements were available for the cobalt samples, which is why these were only investigated qualitatively in various measurement

configurations. For one, the magnetization precession was investigated using an electromagnet for different field strengths perpendicular to the sample surface. Here, an increase in the precession frequency and a linear increase in the precession amplitude were observed. The linear increase in the precession amplitude can be explained by the increase in the initial $m_z$ component. In this model, the amplitude is expected to decrease over a field range given by the magneto-elastic coupling when the external field is equal to the saturation field. However, measurements at such field strengths are not yet possible with the measurement setup used, as the maximum external fields achieved are approximately 1.3 T. In a further series of measurements, the magnetization dynamics were investigated for different excitation fluences. It was found that it is possible to switch between the different excitation mechanisms, i.e. strain and demagnetization, by selecting the excitation fluence. For low fluences, the precession is driven by the strain, whereby the $m_z$ component decreases after the. In contrast, for high fluences, the change in the saturation field decreases nonlinearly, resulting in the precession dynamics starting with increasing $m_z$ component. Finally, the magnetization dynamics were investigated for different orientations of the external field, using a similar procedure as for the nickel samples. The different behaviour of the angle-dependent precession frequency can be attributed to possible different anisotropies. The discrepancy in the results may be attributed to the differing crystallinities of the two samples. Further measurements on identically grown samples could be conducted to verify a systematic trend. In the third section, a coherent control double-pulse excitation scheme was presented, which represents a significant advancement over previous methods for controlling magnetization dynamics. Instead of exciting the precession dynamics twice using the same mechanism, the alternation between strain and demagnetization is used as a driving factor. This allows for the targeted amplification or attenuation of the precession dynamics.

## 5.2 Outlook I

In the following parts of this work, I will present a speculative outlook that addresses two key areas: spatially resolved magnetization dynamics and a formalism for the description of demagnetization dynamics in the context of free energy.
The simulation of the magnetization dynamics discussed in section 4.1 contain the approximation that the sample has a homogeneous temperature and average strain. The dynamics of temperature and strain were calculated using the UDKM1DSIM toolbox, and then the temperature and strain were weighted with the sample profile. The weighted temperature and strain values were then used as input variables to calculate the magnetization dynamics. A more advanced model would consider the dynamics at each individual lattice point and include the exchange interaction between the magnetic moments. The program used in this work to calculate the magnetization dynamics can be rewritten relatively easily so that the magnetization dynamics can be calculated individually for each location in the sample if the exchange interaction is ignored. The results of this simulation for the 20 nm thin nickel sample are shown in figure 5.1. The excitation of the precession in the 20 nm thin layer is homogeneous. The amplitude of the precession is approximately the same at each location of the sample. Figure 5.1 (b) shows the dynamics of the $m_z$ component of the magnetization within the sample. Here, too, it can be seen that the sample is excited homogeneously. Figure 5.1, c) shows the magnetization dynamics at different locations of the sample. The dark red curve shows the dynamics at the surface of the sample, the yellow curve the dynamics in the center and the blue curve at the surface where the pump is incident. In these simulations, the measured response of the magnetization can be compared to the weighted $m_z$ component in the region being probed. The light red curve confirms this and is in very good

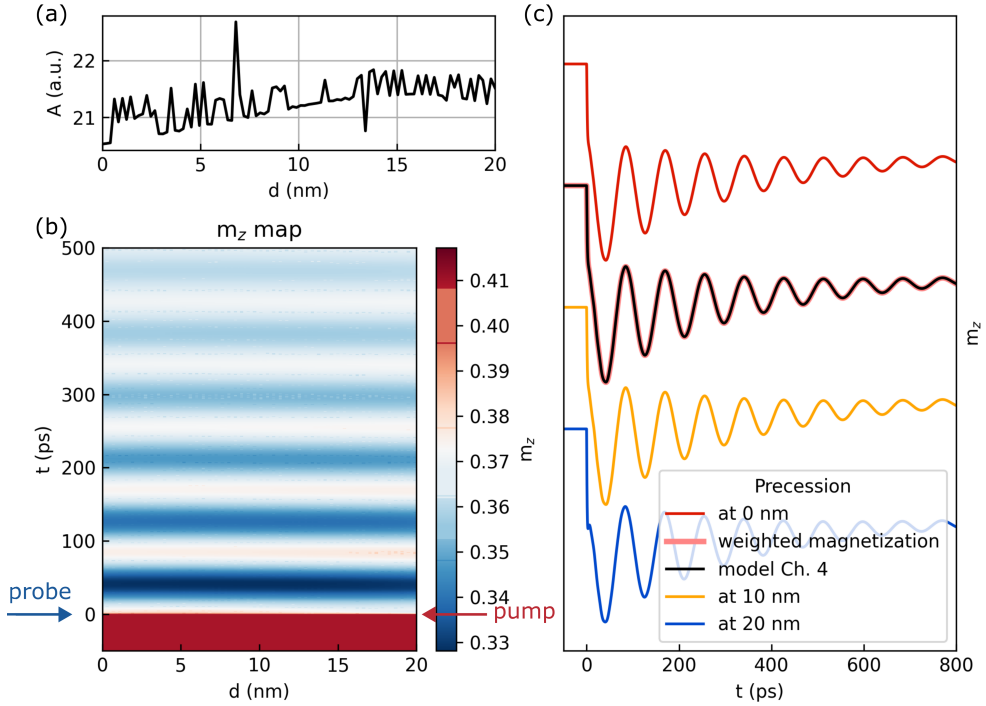


FIGURE 5.1: **Simulated magnetization response for 20 nm nickel (1D):** (a) plots the amplitude of precession throughout the sample. (b) shows the evolution of the $m_z$ component. In (c) the magnetization response at different positions in the sample is compared with the magnetization response calculated from the weighting of $m_z$ with the probe profile and with the simulation from section 4.1. For the simulations, the external field was set to 360 mT and the angle of the field with respect to the surface normal $\xi$ was set to 10°.

agreement with the black curve, which shows the dynamics of the magnetization from section 4.1. All these curves are very comparable, which supports the claim that the excitation of the precession is homogeneous.
Figure 5.2 depicts the same simulation for the 200 nm sample in back- and frontside excitation. Here, the excitation of the sample is significantly more inhomogeneous than in Figure 5.1 (a). It is also notable that the amplitude profile after front- and backside excitation is comparable, but not identical. This discrepancy can be attributed to the fact that the excitation fluence is twice as high for the backside simulation. In the latter case, the amplitude decreases as one approaches the excitation point, whereas for fronstide excitation depicted in figure 5.2 (d), it increases in the excited region. This is due to the interplay of demagnetization- and strain-driven precession. While the strain is dominant in the pumped region for frontside excitation, the demagnetization-driven excitation is significantly stronger for the backside geometry. Since both effects act in opposition to one another, the amplitude in Figure 5.2 (a) decreases at 200 nm. The precession is most effectively excited in the center of the sample for both measurement geometries. This is due to the ideal resonant amplification of the precession by strain pulses. In the center of the sample, the sound pulses do not arrive every 70 ps, but every 35 ps. Additionally, due to reflection at the surface, the sign of the strain pulse is reversed, which ensures phase matching with the precession. Figure 5.2 (b,e), which shows the $m_z$ component, clearly demonstrates that the precession is most strongly excited in the center of the sample. The inhomogeneous excitation of the sample can also be clearly seen in Figure 5.2 (c,f). Here, the dynamics change

significantly depending on the location in the sample. Nevertheless, the magnetization dynamics weighted by the probe penetration profile (light red) agree well with the dynamics simulated in section 4.1 (black curves).
The simulations show that the approximate description of the magnetization dynamics of uncoupled spins by a weighted temperature and strain is a good approximation. For coupled spins, however, the situation could be significantly different in the case of inhomogeneously excited samples. For example, it is plausible that the amplitude of the precession in the investigated regions, especially for the backside-excited 200-nm-thick sample, could be significantly larger for simulations with exchange interaction. The spins, which are optimally excited in the center of the sample, ensure that the amplitude at the boundaries of the sample is also larger due to the coupling. The effect should be particularly pronounced with cobalt, as the exchange stiffness is particularly high here [86]. Currently the UDKM1DSIM toolbox is being expanded to simulate the dynamics of magnetization with exchange interaction. In the future, it should be possible to use it to calculate not only the dynamics of temperature and strain, but also the precession dynamics driven by them. More work is needed, to ensure an accurate implementation. In addition, the integration of different models for precession dynamics into the toolbox is of great interest, as this allows a comparison of the extended LLG equation used in this work with models based on the LLB equation.

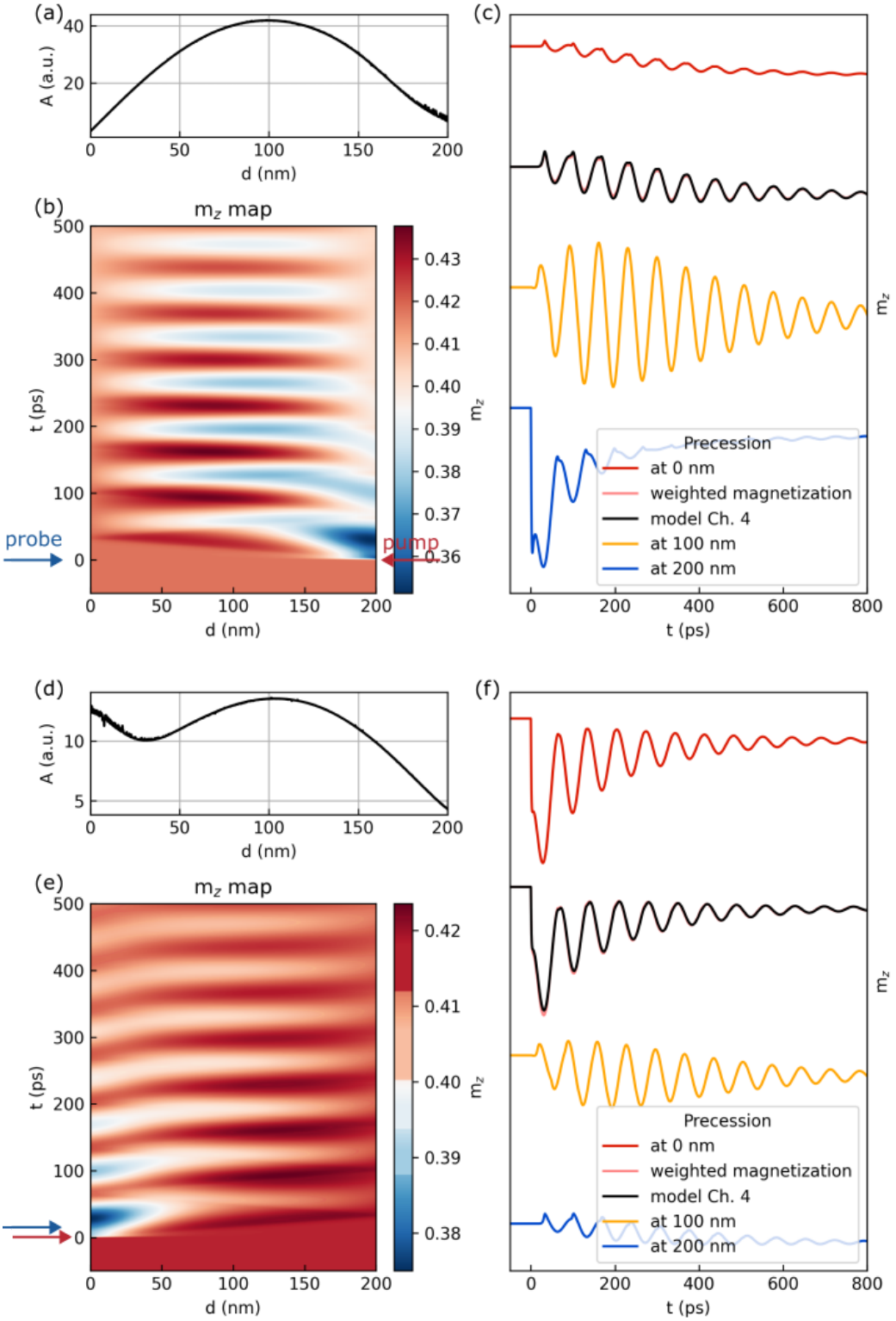


FIGURE 5.2: **Simulated magnetization response for 200 nm nickel (1D):** The top half shows the simulation for backside excitation, the bottom half shows the simulation for frontside excitation. (a,d) plots the amplitude of precession throughout the sample. (b,e) shows the evolution of the $m_z$ component. In (c,f) the magnetization response at different positions in the sample is compared with the magnetization response calculated from the weighting of $m_z$ with the probe profile and with the simulation from section 4.1. For the simulations, the external field was set to 440 mT and the angle of the field with respect to the surface normal $\xi$ was set to 45°.

## 5.3 Outlook II

The modified LLG equation 2.39 is easy to motivate, but it lacks a deeper theoretical consideration that justifies this equation. It should also be noted that the description of demagnetization in this work is only meaningful for the limiting case of small temperature differences in the measured region. This is due to the assumption that the magnetization is always in thermodynamic equilibrium with the phonons. As soon as the temperature of the system is in the range of the Curie temperature, a clearly different behavior is expected. For instance, a high fluence results in the remagnetization taking much longer than would be expected from the electron and phonon temperatures. This behavior can be understood (not completely) [87], in the context of the microscopic 2-temperature model (section 2.3.2). It would be interesting to investigate whether the external field has an influence on the dynamics. If so, it is conceivable that the magnetization dynamics in equation 2.37 might be better expressed by

$$\frac{dm}{dt} = Rm\frac{T_p}{T_C}\left[(1 - m\coth\left(\frac{mT_C}{T_e} + \frac{\mu_B B}{k_B T_C}\right)\right]. \tag{5.1}$$

This equation would reproduce the same temperature-dependent curve for the stationary magnetization when an external field is applied as for the Ising and mean field model. However, a completely different approach is also conceivable, which originates from thermodynamics. In this case, the equation of motion for a non-conserved scalar order parameter, like the magnetization amplitude $m$, is **[doi:10.1080/00018730110117433 ]**

$$\frac{dm}{dt} = -\Gamma\frac{\delta F}{\delta m}, \tag{5.2}$$

where $\Gamma$ is a kinetic coefficent that defines the timescale of the magnetization dynamics. As this kinetic coefficient describes the demagnetization process, it is plausible that it depends on temperature or magnetization. For example, the scattering rate $\tau^{-1}$ in the Elliot-Yafet mechanism is linearly proportional to the temperature [89]. In the following, however, this value is kept constant. $F$ is the free energy, in the framework of the Ising- or the mean field model this equation becomes,

$$\frac{dm}{dt} = -\Gamma\left(-\mu_B B - k_B T_c m + k_B T \operatorname{arctanh}(m)\right). \tag{5.3}$$

This approach is particularly interesting because a description using the free energy automatically includes critical phenomena in the vicinity of the phase transition. In addition, this approach also includes a description of the heat capacity in the vicinity of the phase transition [90]. The heat capacity can be calculated from the free energy as follows

$$C = -T\frac{\partial^2 F}{\partial T^2}. \tag{5.4}$$

Figure 5.3 compares the two different models (equation 5.1 and 5.3) for demagnetization dynamics. In order to obtain a model of the magnetization dynamics at high excitation fluences that comes as close as possible to reality, a modified model with strong electron-spin coupling (s-TTM) was chosen. In this model, the heat capacity of the spin and the electron system are considered together, with an increase in the heat capacity near the phase transition taken into account [38, 39]. In order to account for the cooling of the layer to the substrate, a bath is introduced in addition to the electron and phonon system, which is comparatively weakly coupled to the phonon bath. The temperature dynamics are described

by

$$\frac{dT_e}{dt} = -\frac{G_{ep}}{C_e}(T_e - T_p) + \frac{P(t)}{C_e}, \tag{5.5}$$

$$\frac{dT_p}{dt} = -\frac{G_{ep}}{C_p}(T_p - T_e) - \frac{G_{bp}}{C_p}(T_p - T_b), \tag{5.6}$$

$$\frac{dT_b}{dt} = -\frac{G_{bp}}{C_b}(T_b - T_p),. \tag{5.7}$$

The modified temperature-dependent heat capacity of the electrons, $C_e$, and that of the phonons, $C_p$, were taken from the literature [39]. The heat capacity of the bath was set to ten times the value of the phonons. The electron-phonon coupling was set to the value of $G_{ep} = 1.5 \cdot 10^{18}$ and the coupling with the bath to the value of $G_{bp} = 1.5 \cdot 10^{16}$. The scattering rate in the equations for the magnetization dynamics is $R = 17.2\ \mathrm{ps}^{-1}$ and $\Gamma = 27\ \mathrm{ns}^{-1}$.
The general shape of the magnetization dynamics shown in Figure 5.3 is strikingly similar in both models. This is not unexpected for the dynamics at later times, given that the magnetization is in thermal equilibrium at this time, and this equilibrium is identical for both models. The shape of the magnetization dynamics in the first picoseconds is strongly influenced by the kinetic coefficient $\Gamma$ for the free energy model. The external field also exerts a clear influence on the magnetization dynamics in both cases. In Figure 5.3 (a) and (f), where no external field is present, the light red curves demonstrate complete demagnetization at times above 10 ps. In contrast, in Figure 5.3 (e) and (j), where the external field was set to 2 T, the magnetization at 10 ps exhibits a higher magnetization. Additionally the extremly fast remagnetization at zero field, cannot be seen in scenarios with magnetic fields. The reason for this is, that due to the external magnetic field, the Free Energy Landscape near $m \approx 0$ changes, such that metastable magnetization states are avoided.
Based on this approach, it may even be possible to establish a general equation of motion for magnetization dynamics that includes demagnetization and precession. This requires a formalism that links the free energy of the magnetization orientation to the free energy of the magnetization amplitude and an equation of motion for a non-conserved vectorial order parameter with angular momentum. Further work is required to verify the validity of this approach.

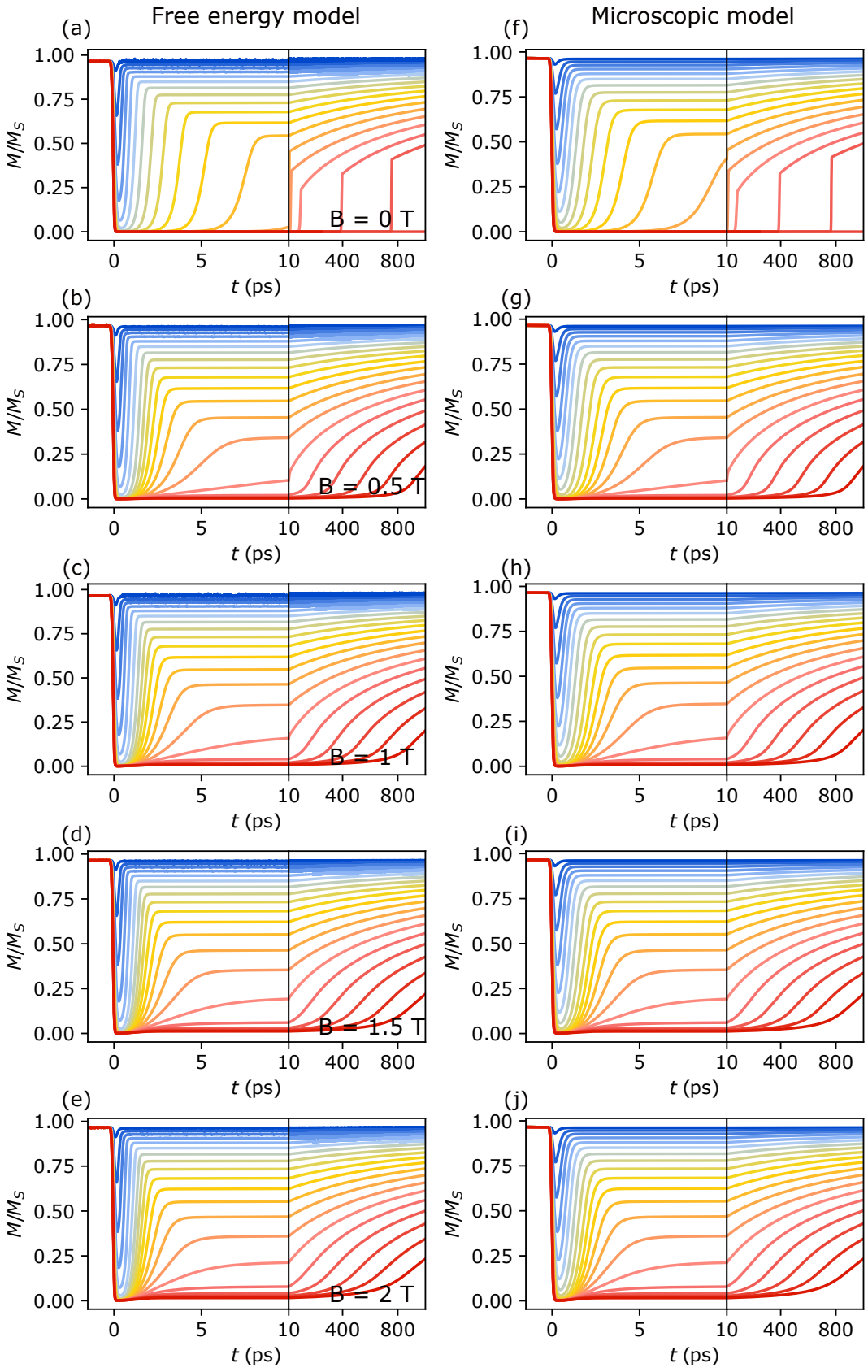


FIGURE 5.3: **Comparison of different demagnetization models:** (a, b, c, d, e) illustrates the resulting magnetization dynamics for equation 5.3 under varying external magnetic field strengths. Figure (f, g, h, i, j) depicts the magnetization dynamics for the same temperature evolution of the phonon and electron systems, as described by equation 5.1, under varying external magnetic field strengths. The magnetization dynamics are quite similar across both models.

# Bibliography


[1] E. Beaurepaire, J.-C. Merle, A. Daunois, and J.-Y. Bigot, "Ultrafast Spin Dynamics in Ferromagnetic Nickel", Phys. Rev. Lett. **76**, 4250–4253 (1996).

[2] J. Hohlfeld, E. Matthias, R. Knorren, and K. H. Bennemann, "Nonequilibrium Magnetization Dynamics of Nickel", Phys. Rev. Lett. **78**, 4861–4864 (1997).

[3] M. Vomir, L. H. F. Andrade, L. Guidoni, E. Beaurepaire, and J.-Y. Bigot, "Real space trajectory of the ultrafast magnetization dynamics in ferromagnetic metals", Physical review letters **94**, 237601 (2005).

[4] A. V. Scherbakov, A. S. Salasyuk, A. V. Akimov, X. Liu, M. Bombeck, C. Brüggemann, D. R. Yakovlev, V. F. Sapega, J. K. Furdyna, and M. Bayer, "Coherent magnetization precession in ferromagnetic (Ga,Mn)As induced by picosecond acoustic pulses", Physical review letters **105**, 117204 (2010).

[5] M. Deb, P. Molho, B. Barbara, and J.-Y. Bigot, "Temperature and magnetic field dependence of rare−earth↔iron exchange resonance mode in a magnetic oxide studied with femtosecond magneto-optical Kerr effect", Physical Review B **94**, 153 (2016).

[6] M. Deb, E. Popova, M. Hehn, N. Keller, S. Mangin, and G. Malinowski, "Picosecond acoustic-excitation-driven ultrafast magnetization dynamics in dielectric Bi-substituted yttrium iron garnet", Physical Review B **98**, 444 (2018).

[7] S. Alebrand, M. Gottwald, M. Hehn, D. Steil, M. Cinchetti, D. Lacour, E. E. Fullerton, M. Aeschlimann, and S. Mangin, "Light-induced magnetization reversal of high-anisotropy TbCo alloy films", Applied Physics Letters **101**, 162408 (2012).

[8] C. D. Stanciu, F. Hansteen, A. V. Kimel, A. Kirilyuk, A. Tsukamoto, A. Itoh, and T. Rasing, "All-Optical Magnetic Recording with Circularly Polarized Light", Phys. Rev. Lett. **99**, 047601 (2007).

[9] K. Neeraj, N. Awari, S. Kovalev, D. Polley, N. Zhou Hagström, S. S. P. K. Arekapudi, A. Semisalova, K. Lenz, B. Green, J.-C. Deinert, I. Ilyakov, M. Chen, M. Bawatna, V. Scalera, M. d'Aquino, C. Serpico, O. Hellwig, J.-E. Wegrowe, M. Gensch, and S. Bonetti, "Inertial spin dynamics in ferromagnets", Nature Physics **17**, 245–250 (2021).

[10] V. Unikandanunni, R. Medapalli, M. Asa, E. Albisetti, D. Petti, R. Bertacco, E. E. Fullerton, and S. Bonetti, "Inertial Spin Dynamics in Epitaxial Cobalt Films", Physical review letters **129**, 237201 (2022).

[11] L. Thevenard, I. S. Camara, S. Majrab, M. Bernard, P. Rovillain, A. Lemaıtre, C. Gourdon, and J.-Y. Duquesne, "Precessional magnetization switching by a surface acoustic wave", Phys. Rev. B **93**, 134430 (2016).

[12] A. D. Kent, B. Özyilmaz, and E. del Barco, "Spin-transfer-induced precessional magnetization reversal", Applied Physics Letters **84**, 3897–3899 (2004).

[13] Y. Shin, S. Yoon, J.-I. Hong, and J.-W. Kim, "Magnetoelasticity-driven phase inversion of ultrafast spin precession in NixFe100-x thin films", Journal of Science: Advanced Materials and Devices **8**, 100568 (2023).

[14] Y. Shin, M. Vomir, D.-H. Kim, P. C. Van, J.-R. Jeong, and J.-W. Kim, "Quasi-static strain governing ultrafast spin dynamics", Communications Physics **5**, 56 (2022).

[15] V. S. Vlasov, A. V. Golov, L. N. Kotov, V. I. Shcheglov, A. M. Lomonosov, and V. V. Temnov, "The Modern Problems of Ultrafast Magnetoacoustics (Review)", Acoustical Physics **68**, 18–47 (2022).

[16] U. Vernik, A. M. Lomonosov, V. S. Vlasov, L. N. Kotov, D. A. Kuzmin, I. V. Bychkov, P. Vavassori, and V. V. Temnov, "Resonant phonon-magnon interactions in freestanding metal-ferromagnet multilayer structures", Phys. Rev. B **106**, 144420 (2022).

[17] D. Schick, "udkm1Dsim – a Python toolbox for simulating 1D ultrafast dynamics in condensed matter", Computer Physics Communications **266**, 108031 (2021).

[18] J. Jarecki, "Magnetization Dynamics in Metallic Heterostructures studied by a combination of tr-MOKE and UXRD", Master thesis (University of Potsdam, Institute for Physics and Astronomy, 2023).

[19] M. Hudl, M. d'Aquino, M. Pancaldi, S.-H. Yang, M. G. Samant, S. S. P. Parkin, H. A. Dürr, C. Serpico, M. C. Hoffmann, and S. Bonetti, "Nonlinear Magnetization Dynamics Driven by Strong Terahertz Fields", Phys. Rev. Lett. **123**, 197204 (2019).

[20] M. Mattern, A. von Reppert, S. P. Zeuschner, M. Herzog, J.-E. Pudell, and M. Bargheer, "Concepts and use cases for picosecond ultrasonics with x-rays", Photoacoustics **31**, 100503 (2023).

[21] A. von Reppert, "Magnetic strain contributions in laser-excited metals studied by time-resolved X-ray diffraction", PhD dissertation (University of Potsdam, Institute for Physics and Astronomy, 2021).

[22] J.-E. Puddel, "Lattice Dynamics observed with x-ray diffraction", PhD dissertation (University of Potsdam, Institute for Physics and Astronomy, 2020).

[23] J. Stöhr and H. C. Siegmann, *Magnetism From Fundamentals to Nanoscale Dynamics* (Springer Berlin, Heidelberg, 2006).

[24] R. Gross and A. Marx, *Festkörperphysik* (München: De Gruyter Oldenbourg, 2014).

[25] L. Baselgia, M. Warden, F. Waldner, S. L. Hutton, J. E. Drumheller, Y. Q. He, P. E. Wigen, and M. Mary ško, "Derivation of the resonance frequency from the free energy of ferromagnets", Phys. Rev. B **38**, 2237–2242 (1988).

[26] B. D. Cullity and C. D. Graham, *Introduction to Magnetic Materials* (John Wiley Sons, Ltd, 2008).

[27] K. D. Greve, *Magnetostriction and Magneto-Elastic Coupling: from Electric Hum to Sonar*, Lecture notes, `http://large.stanford.edu/courses/2007/ph210/degreve2`.

[28] C. Kittel, "Physical Theory of Ferromagnetic Domains", Rev. Mod. Phys. **21**, 541–583 (1949).

[29] S. Mankovsky, S. Polesya, H. Lange, M. Weißenhofer, U. Nowak, and H. Ebert, "Angular Momentum Transfer via Relativistic Spin-Lattice Coupling from First Principles", Phys. Rev. Lett. **129**, 067202 (2022).

[30] R. R. Birss, G. J. Keeler, and C. H. Shepherd, "Temperature dependence of the magnetocrystalline anisotropy energy of nickel in the (100) plane", **7**, 1683 (1977).

[31] W. J. Carr, "Temperature Dependence of Ferromagnetic Anisotropy", Phys. Rev. **109**, 1971–1976 (1958).

[32] A. Aharoni, *Introduction to the Theory of Ferromagnetism, Second Edition (International Series of Monographs on Physics)*, 2nd, International Series of Monographs on Physics volume 109 (Oxford University Press, USA, 2001).

[33] J. Chang, *Landau Theory*, Lecture notes, https://stanford.edu/~jeffjar/statmech/week4e.html#deriving.

[34] P. Young, *Magnetic Phase Transitions, and Free Energies in a Magnetic Field*, Lecture notes, https://young.physics.ucsc.edu/112/magnetic.pdf.

[35] J. Crangle and G. M. Goodman, "The Magnetization of Pure Iron and Nickel", Proceedings of the Royal Society of London Series A **321**, 477–491 (1971).

[36] J. Jarecki, M. Mattern, F.-C. Weber, J.-E. Pudell, X.-G. Wang, J.-C. Rojas Sánchez, M. Hehn, A. von Reppert, and M. Bargheer, "Controlling effective field contributions to laser-induced magnetization precession by heterostructure design", Communications Physics **7**, 112 (2024).

[37] B. Koopmans, G. Malinowski, F. Dalla Longa, D. Steiauf, M. Fähnle, T. Roth, M. Cinchetti, and M. Aeschlimann, "Explaining the paradoxical diversity of ultrafast laser-induced demagnetization", Nature Materials **9**, 259–265 (2010).

[38] D. Zahn, F. Jakobs, H. Seiler, T. A. Butcher, D. Engel, J. Vorberger, U. Atxitia, Y. W. Windsor, and R. Ernstorfer, "Intrinsic energy flow in laser-excited 3*d* ferromagnets", Phys. Rev. Res. **4**, 013104 (2022).

[39] D. Zahn, F. Jakobs, Y. W. Windsor, H. Seiler, T. Vasileiadis, T. A. Butcher, Y. Qi, D. Engel, U. Atxitia, J. Vorberger, and R. Ernstorfer, "Lattice dynamics and ultrafast energy flow between electrons, spins, and phonons in a 3d ferromagnet", Phys. Rev. Res. **3**, 023032 (2021).

[40] U. Atxitia, D. Hinzke, and U. Nowak, "Fundamentals and applications of the Landau–Lifshitz–Bloch equation", Journal of Physics D: Applied Physics **50**, 033003 (2016).

[41] U. Atxitia, P. Nieves, and O. Chubykalo-Fesenko, "Landau-Lifshitz-Bloch equation for ferrimagnetic materials", Phys. Rev. B **86**, 104414 (2012).

[42] J. Smit and H. G. Beljers, "Ferromagnetic resonance absorption in $BaFe_{12}O_{19}$, a highly anisotropic crystal", Philips Research Reports **10**, 113–140 (1955).

[43] M. Faraday, "On the magnetization of light and the illumination of magnetic lines of force", Philosophical Magazine and Journal of Science **3** (1846).

[44] J. Kerr, "On rotation of the plane of polarization by reflection from the pole of a magnet", Philosophical Magazine and Journal of Science **5** (1877).

[45] F. Liu, T. Makino, T. Yamasaki, K. Ueno, A. Tsukazaki, T. Fukumura, Y. Kong, and M. Kawasaki, "Ultrafast Time-Resolved Faraday Rotation in EuO Thin Films", Phys. Rev. Lett. **108**, 257401 (2012).

[46] I. Razdolski, A. Alekhin, U. Martens, D. Bürstel, D. Diesing, M. Münzenberg, U. Bovensiepen, and A. Melnikov, "Analysis of the time-resolved magneto-optical Kerr effect for ultrafast magnetization dynamics in ferromagnetic thin films", Journal of Physics: Condensed Matter **29**, 174002 (2017).

[47] P. M. Oppeneer, "Theory of the Magneto-Optical Kerr Effect in Ferromagnetic Compounds", Habilitation (TU Dresden, Institute for theoretical Physics, 1999).

[48] P. Fumagalli and J. Schoenes, *Magneto-optics an introduction* (De Gruyter, Berlin/Boston, 2022).

[49] J. Kuneš, "Magnetism and Magneto-Optics in DFT", Physica Scripta **2004**, 116 (2004).

[50] H. Ebert, "Magneto-optical effects in transition metal systems", Reports on Progress in Physics **59**, 1665 (1996).

[51] S. X. Hu and L. A. Collins, "Attosecond Pump Probe: Exploring Ultrafast Electron Motion inside an Atom", Phys. Rev. Lett. **96**, 073004 (2006).

[52] Š. Višňovský, V. Pařízek, M. Nývlt, P. Kielar, V. Prosser, and R. Krishnan, "Magneto-optical Kerr spectra of nickel", Journal of Magnetism and Magnetic Materials **127**, 135–139 (1993).

[53] L. Willig, "Ultrafast Magneto-Optical Studies of Remagnetisation Dynamics in Transition Metals", PhD dissertation (University of Potsdam, Institute for Physics and Astronomy, 2019).

[54] I. Žuti ć, J. Fabian, and S. Das Sarma, "Spintronics: Fundamentals and applications", Rev. Mod. Phys. **76**, 323–410 (2004).

[55] Z. Chai, X. Hu, F. Wang, X. Niu, J. Xie, and Q. Gong, "Ultrafast All-Optical Switching", Advanced Optical Materials **5**, 1600665 (2017).

[56] M. van Kampen, C. Jozsa, J. T. Kohlhepp, P. LeClair, L. Lagae, W. J. M. de Jonge, and B. Koopmans, "All-optical probe of coherent spin waves", Physical review letters **88**, 227201 (2002).

[57] T. Kampfrath, A. Sell, G. Klatt, A. Pashkin, S. Mährlein, T. Dekorsy, M. Wolf, M. Fiebig, A. Leitenstorfer, and R. Huber, "Coherent terahertz control of antiferromagnetic spin waves", Nature Photonics **5**, 31–34 (2011).

[58] C. Tzschaschel, K. Otani, R. Iida, T. Shimura, H. Ueda, S. Günther, M. Fiebig, and T. Satoh, "Ultrafast optical excitation of coherent magnons in antiferromagnetic NiO", Physical Review B **95**, 1–11 (2017).

[59] P. Němec, M. Fiebig, T. Kampfrath, and A. V. Kimel, "Antiferromagnetic opto-spintronics", Nature Physics **14**, 229–241 (2018).

[60] C. Tzschaschel, T. Satoh, and M. Fiebig, "Tracking the ultrafast motion of an antiferromagnetic order parameter", Nature Communications **10**, 3995 (2019).

[61] G. Bonfiglio, K. Rode, K. Siewerska, J. Besbas, G. Y. P. Atcheson, P. Stamenov, J. M. D. Coey, A. V. Kimel, T. Rasing, and A. Kirilyuk, "Magnetization dynamics of the compensated ferrimagnet $Mn_2Ru_xGa$", Phys. Rev. B **100**, 104438 (2019).

[62] W. Li, J. Yan, M. Tang, S. Lou, Z. Zhang, X. L. Zhang, and Q. Y. Jin, "Composition and temperature-dependent magnetization dynamics in ferrimagnetic TbFeCo", Phys. Rev. B **97**, 184432 (2018).

[63] I. Razdolski, A. Alekhin, N. Ilin, J. P. Meyburg, V. Roddatis, D. Diesing, U. Bovensiepen, and A. Melnikov, "Nanoscale interface confinement of ultrafast spin transfer torque driving non-uniform spin dynamics", Nature communications **8**, 15007 (2017).

[64] M. Deb, E. Popova, M. Hehn, N. Keller, S. Petit-Watelot, M. Bargheer, S. Mangin, and G. Malinowski, "Femtosecond Laser-Excitation-Driven High Frequency Standing Spin Waves in Nanoscale Dielectric Thin Films of Iron Garnets", Physical review letters **123**, 027202 (2019).

[65] J.-W. Kim, M. Vomir, and J.-Y. Bigot, "Controlling the spins angular momentum in ferromagnets with sequences of picosecond acoustic pulses", Scientific reports **5**, 8511 (2015).

[66] M. Deb, E. Popova, H.-Y. Jaffrès, N. Keller, and M. Bargheer, "Controlling High-Frequency Spin-Wave Dynamics Using Double-Pulse Laser Excitation", Physical Review Applied **18**, 10.1103/PhysRevApplied.18.044001 (2022).

[67] M. Tomoda, A. Toda, O. Matsuda, V. E. Gusev, and O. B. Wright, "Sound velocity mapping from GHz Brillouin oscillations in transparent materials by optical incidence from the side of the sample", Photoacoustics **30**, 100459 (2023).

[68] C. Thomsen, H. T. Grahn, H. J. Maris, and J. Tauc, "Surface generation and detection of phonons by picosecond light pulses", Phys. Rev. B **34**, 4129–4138 (1986).

[69] M. Djordjevic, M. Lüttich, P. Moschkau, P. Guderian, T. Kampfrath, R. G. Ulbrich, M. Münzenberg, W. Felsch, and J. S. Moodera, "Comprehensive view on ultrafast dynamics of ferromagnetic films", physica status solidi c **3**, 1347–1358 (2006).

[70] D. Zahn, H. Seiler, Y. W. Windsor, and R. Ernstorfer, "Ultrafast lattice dynamics and electron–phonon coupling in platinum extracted with a global fitting approach for time-resolved polycrystalline diffraction data", Structural Dynamics **8**, 064301 (2021).

[71] J. R. Neighbours, F. W. Bratten, and C. S. Smith, "The Elastic Constants of Nickel", Journal of Applied Physics **23**, 389–393 (1952).

[72] R. S. Krishnan, R. Srinivasan, and S. Devanarayanan, *Thermal Expansion of Crystals* (Pergamon Press, 1979).

[73] F. H. Featherston and J. R. Neighbours, "Elastic Constants of Tantalum, Tungsten, and Molybdenum", Phys. Rev. **130**, 1324–1333 (1963).

[74] X. Wang, S. Nie, J. Li, R. Clinite, M. Wartenbe, M. Martin, W. Liang, and J. Cao, "Electronic Grüneisen parameter and thermal expansion in ferromagnetic transition metal", Applied Physics Letters **92**, 121918 (2008).

[75] W. S. M. Werner, K. Glantschnig, and C. Ambrosch-Draxl, "Optical Constants and Inelastic Electron-Scattering Data for 17 Elemental Metals", Journal of Physical and Chemical Reference Data **38**, 1013–1092 (2009).

[76] P. B. Johnson and R. W. Christy, "Optical constants of transition metals: Ti, V, Cr, Mn, Fe, Co, Ni, and Pd", Phys. Rev. B **9**, 5056–5070 (1974).

[77] J.-E. Pudell, M. Mattern, M. Hehn, G. Malinowski, M. Herzog, and M. Bargheer, "Heat Transport without Heating?—An Ultrafast X-Ray Perspective into a Metal Heterostructure", Advanced Functional Materials **30**, 2004555.

[78] Z. Zhang and Y. Wei, "Optimization of experiment settings in ferromagnetic resonance measurements", Results in Physics **7**, 2614–2618 (2017).

[79] J. M. D. Coey, *Magnetism and Magnetic Materials* (Cambridge University Press, 2010).

[80] J. Kisielewski, A. Kirilyuk, A. Stupakiewicz, A. Maziewski, A. Kimel, T. Rasing, L. T. Baczewski, and A. Wawro, "Laser-induced manipulation of magnetic anisotropy and magnetization precession in an ultrathin cobalt wedge", Phys. Rev. B **85**, 184429 (2012).

[81] Q. Zhang, A. V. Nurmikko, A. Anguelouch, G. Xiao, and A. Gupta, "Coherent Magnetization Rotation and Phase Control by Ultrashort Optical Pulses in $CrO_2$ Thin Films", Phys. Rev. Lett. **89**, 177402 (2002).

[82] M. Deb, E. Popova, H.-Y. Jaffrès, N. Keller, and M. Bargheer, "Controlling High-Frequency Spin-Wave Dynamics Using Double-Pulse Laser Excitation", Phys. Rev. Appl. **18**, 044001 (2022).

[83] T. Kampfrath, A. Sell, and G. e. a. Klatt, "Coherent terahertz control of antiferromagnetic spin waves", Nature Photonics **5**, 31–34 (2011).

[84] J. Kim, M. Vomir, and J. Bigot, "Controlling the Spins Angular Momentum in Ferromagnets with Sequences of Picosecond Acoustic Pulses", Scientific Reports **5**, 10.1038/srep08511 (2014).

[85] M. Mattern, F.-C. Weber, D. Engel, C. von Korff Schmising, and M. Bargheer, "Coherent control of magnetization precession by double-pulse activation of effective fields from magnetoacoustics and demagnetization", Applied Physics Letters **124**, 102402 (2024).

[86] M. D. Kuz'min, K. P. Skokov, L. V. B. Diop, I. A. Radulov, and O. Gutfleisch, "Exchange stiffness of ferromagnets", The European Physical Journal Plus **135**, 301 (2020).

[87] M. Mattern, "Insights into laser-induced magnetization dynamics using picosecond ultrasonics with x-ray diffraction", PhD dissertation (University of Potsdam, Institute for Physics and Astronomy, 2024).

[88] A. J. Bray, "Theory of phase-ordering kinetics", Advances in Physics **51**, 481–587 (2002).

[89] A. Rustagi, *Spin Relaxation Mechanisms*, Lecture notes, https://www.phys.ufl.edu/~avinash/Notes/Spin_Relaxation/Spin_Relaxation.pdf.

[90] J. F. Rodríguez and J. A. Blanco, "Temperature Dependence of the Molar Heat Capacity for Ferromagnets Within the Mean Field Theory", Physica Scripta **71**, CC19 (2005).

# Declaration of Authorship

I, Fried-Conrad WEBER, declare that this thesis titled, "Magnetization precession in 3D metals: the role of heat and strain" and the work presented in it are my own. I confirm that:

- This work was done wholly or mainly while in candidature for a research degree at this University.
- Where any part of this thesis has previously been submitted for a degree or any other qualification at this University or any other institution, this has been clearly stated.
- Where I have consulted the published work of others, this is always clearly attributed.
- Where I have quoted from the work of others, the source is always given. With the exception of such quotations, this thesis is entirely my own work.
- I have acknowledged all main sources of help.
- Where the thesis is based on work done by myself jointly with others, I have made clear exactly what was done by others and what I have contributed myself.

Signed: _____

Date: _____